

---

Electronic Thesis and Dissertation Repository

---

8-4-2017 12:00 AM

# Using Computed Tomography Perfusion to Evaluate the Blood-Brain-Barrier and Blood-Tumor-Barrier Response following Focused Ultrasound Sonication with Microbubble Administration

Hassaan Ahmed, *The University of Western Ontario*

Supervisor: Dr. Ting Lee, *The University of Western Ontario*

A thesis submitted in partial fulfillment of the requirements for the Doctor of Philosophy degree in Medical Biophysics

© Hassaan Ahmed 2017

Follow this and additional works at: <https://ir.lib.uwo.ca/etd>



Part of the [Medical Biophysics Commons](#)

---

## Recommended Citation

Ahmed, Hassaan, "Using Computed Tomography Perfusion to Evaluate the Blood-Brain-Barrier and Blood-Tumor-Barrier Response following Focused Ultrasound Sonication with Microbubble Administration" (2017). *Electronic Thesis and Dissertation Repository*. 4904.  
<https://ir.lib.uwo.ca/etd/4904>

This Dissertation/Thesis is brought to you for free and open access by Scholarship@Western. It has been accepted for inclusion in Electronic Thesis and Dissertation Repository by an authorized administrator of Scholarship@Western. For more information, please contact [wlsadmin@uwo.ca](mailto:wlsadmin@uwo.ca).

## Abstract

The blood-brain-barrier (BBB) is the single most limiting factor in the delivery of neurotherapeutics into the brain. Focused ultrasound sonication combined with intravenous microbubble administration (FUSwMB) is a novel technique that can transiently disrupt the BBB, with minimal vascular or tissue damage, allowing for localized drug delivery over the targeted region. The goals of this thesis are to: 1) use computed tomography (CT) perfusion to measure the permeability surface area product (PS) following FUSwMB in normal rabbits with an intact BBB, and 2) to evaluate the blood-tumor-barrier (BTB) PS response following FUSwMB in a C6 rat glioma model.

Chapter 2 evaluated CT perfusion as a tool for monitoring and measuring the increased PS following FUSwMB induced BBB disruption. A range of exposure parameters, power and sonication time, were evaluated to induce transient BBB disruption with minimal injury, in a rabbit model. The PS vs. time profile showed a distinct window for increased drug delivery following FUSwMB, and can be used to predict delivery over the targeted region.

Chapter 3 evaluated CT perfusion derived BTB PS response acutely over 4 hours, and sub-acutely over 3 days, using both small (760 Da) and large molecular (65 kDa) weight CT contrast agents, following FUSwMB in a C6 rat glioma model. The BTB PS measured with standard small contrast agent, which was abnormally elevated at baseline because of the breakdown of the BBB in tumor vasculature, demonstrated a gradual decrease up to 4 hours following sonication, and remained decreased at 24 hours post. The BTB PS measured with the larger contrast agent showed an increasing trend at 24 hours post FUSwMB, when the Isovue PS was at its lowest.

Chapter 4 investigated the CT Perfusion derived extravascular distribution volume ( $V_e$ ), as a surrogate of vasogenic edema, following FUSwMB in the rat C6 glioma model as in Chapter 3. The decrease in Isovue PS at 24 hours post FUSwMB was accompanied by a decrease in  $V_e$ , implying a decrease in vasogenic edema and also the abnormally elevated interstitial fluid pressure (IFP). The results of Chapter 4 suggested a mechanism for the observed decrease in Isovue BTB PS following FUSwMB in Chapter 3 and its implications on drug delivery in

brain tumors. It is hypothesized that the destruction of newly formed vessels from angiogenesis or the stimulation of reactive glial cells following FUSwMB were responsible for normalizing the BTB PS, thereby lowering IFP and improving perfusion and transvascular drug delivery throughout the tumor.

Chapter 5 summarized the findings indicating CT Perfusion can be used to monitor the change in BBB/BTB PS following FUSwMB. In the disrupted BBB, when PS is 5 times less than blood flow (F), PS can be used to approximate drug delivery, however, when PS is significantly elevated, as with brain tumors, the volume transfer constant (FE) is the correct functional parameter and should be used instead. Future studies investigating the improvement in delivery and clinical outcomes for larger chemotherapeutic drugs, such as bevacizumab, following FUSwMB are also presented.

## Keywords

Focused ultrasound, microbubbles, sonication, blood-brain-barrier, blood-tumor-barrier, CT perfusion, permeability surface area product, volume transfer constant, drug delivery.

## Co-Authorship Statement

Chapter 2, “Focused Ultrasound Sonication with Microbubble Administration Induced Blood-Brain-Barrier Disruption: Quantifying the Increased Endothelial Permeability Surface Area Using Dynamic Contrast Enhanced Computed Tomography in Rabbits”, was submitted as a manuscript to the journal *Ultrasound in Medicine and Biology*. I wrote the manuscript and co-authors include A. Waspe, R. Chopra, K Hynynen, D Jackson, and TY Lee. I was responsible for the design of the study, analysis, interpretation, and writing of the manuscript. Dr. Lee helped design the study, analyze and interpret the results, and with editing of the manuscript. Dr. Chopra helped analyze and interpret the results, and with editing of the manuscript. Drs. Waspe, Chopra, and Hynynen provided focused ultrasound expertise and assistance. Dr. Jackson helped analyze and interpret the histology results.

Chapter 3, “Comparison of Small (760 Da) and Large (65 kDa) Contrast Agent Dynamic Contrast Enhanced Computed Tomography to Measure Blood-Tumor-Barrier Permeability Surface Response Following Focused Ultrasound Sonication with Microbubble Administration in a C6 Rat Glioma Model”, was submitted to the journal *Public Library of Science (PLOS) One*. I wrote the manuscript and co-authors include R Chopra, K Hynynen, and TY Lee. I was responsible for the design of the study, analysis, interpretation, and writing of the manuscript. Dr. Lee helped design the study, analyze and interpret the results, and with editing of the manuscript. Dr. Chopra helped analyze and interpret the results, and with editing of the manuscript. Drs. Chopra, and Hynynen provided focused ultrasound expertise and assistance.

Chapter 4, “Investigating the Decrease in Edema Following Focused Ultrasound with Microbubble Administration using Magnetic Resonance Imaging, and Dynamic Contrast Enhanced Computed Tomography Derived Vascular Distribution Volume in a C6 Rat Glioma Model”, was submitted to the journal *Public Library of Science (PLOS) One*. I wrote the manuscript and co-authors include R Chopra, K Hynynen, and TY Lee. I was responsible for the design of the study, analysis, interpretation, and writing of the manuscript. Dr. Lee helped design the study, analyze and interpret the results, and with editing of the manuscript.

Dr. Chopra helped analyze and interpret the results, and with editing of the manuscript. Drs. Chopra, and Hynynen provided focused ultrasound expertise and assistance.

## Acknowledgments

This Ph.D. thesis would not have been possible without all the support from my supervisor, fellow students, lab members, research assistants, the medical biophysics program, the support staff, as well as my family and friends.

First and foremost, I would like to extend a heart-felt thank-you to my Ph.D. supervisor, Dr. **Ting-Yim Lee**. I am incredibly privileged and grateful to have had an opportunity to work on such an exciting project in your lab, and for your belief in seeing this thesis through to completion. I have the utmost respect for you as a scientist, a researcher, and as a mentor. Whenever we appeared to hit a roadblock, your insightful and thought-provoking discussions always gave the extra push needed to move forward. I am so proud to have been your student and I am certain that the problem solving and other important translational skills you have conferred onto me will help advance my life and future career, no matter what path it takes. I also want to thank my advisors, **Dr. Dwayne Jackson** and **Dr. Rob Bartha**, for helping shape my project, particularly in the early stages.

I would also like to express my gratitude to the rest of the Lee lab students, members, and staff who were instrumental in my research over the last 6 years. None of our animal experiments would have happened without our wonderful technicians. **Lise Desjardins** - I will never forget all the late nights working with the FUS system (especially in the early days), the countless experiments lugging the system around the hospital, all the laughs when things weren't going so well, and for always believing in me when not everyone else did. **Jennifer Hadway** - you always did an amazing job of juggling the schedules, and were always willing to help out, even when you had 10 other things to do. **Laura Morrison** - thank you very much for stepping in and helping out when Laura and Jenn were not available, and always making sure things were running smoothly. **Dr. Errol Stewart** - thank you for your advice and helpful discussions to guide me through my time as a student. **Dr. Lisa Hoffman** - thank you for preparing and providing us with C6 glioma cells and helping out with in vitro experiments. **Baraa Al-Khazraji** - thank you for teaching me how to prepare, stain, and analyze my histology results for Chapter 2. **Cathie Crukley** - thank you for helping out with the tumor immunohistochemistry staining and analysis for Chapter 4.

**Anne Leaist, Wendy Hough, and Dr. Grace Parraga** – thank you for making sure the administrative side of things were always up-to-date.

In addition, I want to thank all the people at FUS Instruments Inc., and our collaborators from Sunnybrook, particularly **Dr. Adam Waspe, Dr. Rajiv Chopra, and Dr. Kullervo Hynynen**, for all their expertise and assistance, without which the focused ultrasound experiments would not have been possible.

Finally, I would like to thank my family for always keeping me level, through all the ups and downs, and always believing in me. The work in this thesis is dedicated to my mother, **Nishat**, my father, **Naseer**, my siblings – **Jowairiyya, Ferouk, Haajarah, and Numan**, and my beautiful fiancé **Sara**. I also can't forget my nephew **Aydin!** Your support, prayers, and love are the reason I am here today.

# Table of Contents

Abstract .....	i
Co-Authorship Statement .....	iii
Acknowledgments .....	v
Table of Contents .....	vii
List of Tables .....	xii
List of Figures .....	xiii
Abstract .....	xviii
Chapter 1 .....	1
1 Introduction .....	1
1.1 Overview .....	1
1.2 Blood-Brain-Barrier (BBB).....	2
1.3 Drug Delivery across the BBB.....	3
1.4 Malignant Gliomas .....	5
1.4.1 Blood-Tumor-Barrier .....	5
1.4.2 Drug Delivery in Brain Tumors .....	7
1.5 FUS and MB induced BBB Disruption.....	11
1.6 The effect of FUS parameters on BBB Disruption .....	12
1.6.1 Transducer Frequency .....	12
1.6.2 Applied Pressure Amplitude or Power.....	14
1.6.3 FUS Pulse Sequence.....	15
1.6.4 Exposure Time .....	17
1.7 The effect of MB on FUS.....	17
1.8 Pre-clinical drug delivery studies using FUS sonication with MB administration	19
1.8.1 Delivery across the Disrupted BBB .....	19

1.8.2	Delivery across the BTB in Glioma Models .....	20
1.9	Computed Tomography (CT) Perfusion .....	22
1.9.1	Imaging the Delivery of Blood Borne Solutes across the BBB .....	22
1.9.2	General Closed Two-Compartmental Model .....	23
1.9.3	Johnson and Wilson Model .....	26
1.9.4	Adiabatic approximation leading to the Johnson-Wilson-Lee Model .....	29
1.9.5	In-vivo Diffusion and Flow Limited Solute Exchange .....	31
1.10	Research Goals and Objectives .....	33
1.11	Thesis Outline .....	33
1.11.1	FUS sonication with MB administration Induced BBB Disruption: Quantifying the Increased Endothelial Permeability using CT Perfusion (Chapter 2).....	33
1.11.2	Using small (750 Da), and large (65 kDa) contrast agent in CT Perfusion to quantify BTB PS response following FUS sonication with MB administration in a C6 rat glioma model (Chapter 3).....	33
1.11.3	Investigating the decrease in edema following FUS sonication with MB administration using MRI and vascular distribution volume, measured from DCE-CT (Chapter 4). .....	34
1.11.4	Conclusion and Future Work (Chapter 5).....	34
1.12	References .....	34
Chapter 2	.....	51
2	Focused Ultrasound Sonication with Microbubble Administration Induced Blood- Brain-Barrier Disruption: Quantifying the Increased Endothelial Permeability Surface Area using Dynamic Contrast Enhanced-Computed Tomography in Rabbits.....	51
2.1	Introduction .....	51
2.2	Methods and Materials .....	53
2.2.1	Animals .....	53
2.2.2	Focused Ultrasound Sonication with Microbubble Administration.....	54
2.2.3	Magnetic Resonance Imaging .....	55
2.2.4	CT Perfusion Protocol.....	56

2.2.5	Tracer Kinetic Analysis.....	56
2.2.6	CT Perfusion Map Analysis.....	58
2.2.7	Histology.....	58
2.2.8	Statistical Analysis.....	59
2.3	Results.....	60
2.4	Discussion.....	66
2.5	Conclusions.....	73
2.6	References.....	73
Chapter 3	.....	78
3	Comparison of Small (760 Da), and Large (65 kDa) Contrast Agent Dynamic Contrast-Enhanced Computed Tomography to measure Blood-Tumor-Barrier Permeability Surface Response Following Focused Ultrasound Sonication with Microbubble Administration in a C6 Rat Glioma Model.....	78
3.1	Introduction.....	78
3.2	Methods and Materials.....	80
3.2.1	Study Protocol and Experimental Groups.....	80
3.2.2	Focused Ultrasound Sonication with Microbubble Administration.....	81
3.2.3	Dynamic Contrast Enhanced Computed Tomography Perfusion.....	82
3.2.4	Tracer Kinetic Modeling.....	83
3.2.5	CT Perfusion Map Analysis.....	85
3.2.6	Statistical Analysis.....	86
3.3	Results.....	86
3.4	Discussion.....	91
3.5	Conclusion.....	100
3.6	References.....	101
Chapter 4	.....	109

4	Investigating the Decrease in Edema following Focused Ultrasound Sonication with Microbubble Administration using Magnetic Resonance Imaging and CT Perfusion Derived Extravascular Distribution Volume in a C6 Rat Glioma Model .....	109
4.1	Introduction .....	109
4.2	Methods and Materials .....	111
4.2.1	Animal Groups .....	111
4.2.2	Focused Ultrasound Sonication and Microbubble Administration .....	112
4.2.3	CT Perfusion Study Protocol.....	112
4.2.4	Tracer Kinetic Modeling .....	113
4.2.5	Magnetic Resonance Imaging .....	114
4.2.6	Imaging Analysis of CT Perfusion and MRI Study .....	115
4.2.7	Calculation of Extravascular Distribution Volume.....	115
4.2.8	Immunohistochemistry .....	116
4.2.9	Statistical Analysis .....	116
4.3	Results .....	117
4.4	Discussion .....	120
4.5	Conclusion.....	124
4.6	References .....	125
Chapter 5	.....	130
5	Conclusion and Future Work.....	130
5.1	Summary of Findings .....	130
5.1.1	CT Perfusion to quantify PS changes following FUSwMB.....	130
5.1.2	BTB PS response following FUSwMB.....	131
5.2	Future Work .....	132
5.2.1	Evaluating the increase in PET-labeled Bevacizumab delivery following FUSwMB in a C6 Rat Tumor Model .....	132
5.2.2	Improvement in clinical outcomes following FUSwMB in combination with Bevacizumab administration in a C6 Rat Glioma Model .....	133

5.3 References .....	134
Curriculum Vitae .....	138

## List of Tables

Table 1-1: The effect of a range of applied acoustic powers on blood-brain-barrier (BBB) disruption, while other parameters were held constant. All sonications had a duration of 20 s, and were performed using 50 ul/kg Optison microbubbles. ....	15
Table 1-2: Comparison of three types of microbubbles (MB) that are commonly used for blood-brain-barrier (BBB) disruption; Definity, Optison, and SonoVue.....	18
Table 1-3: Pre-clinical studies on delivery of different molecules and cells across disrupted blood-brain-barrier (BBB) following focused ultrasound with microbubble administration (FUSwMB).....	19
Table 1-4: Summary of studies on delivery of imaging or therapeutic agents across the blood-tumor-barrier (BTB) following focused ultrasound with microbubble administration (FUSwMB) (100,104–109,116,117). ....	21
Table 2-1: Summary of Focused Ultrasound (FUS) exposure parameters including applied power, sonication time, and total sonication energy ( $E_{\text{applied}}$ ), as well as permeability surface area product (PS) and gross histology results. ....	61
Table 3-1: Summary of pre-clinical studies that investigated tumor PS following focused ultrasound with microbubble administration (FUSwMB) (31,32,33).....	93

## List of Figures

Figure 1-1: Schematic cross-sectional representation of a cerebral capillary, highlighting a single endothelial cell (EC), the tight junctions (TJ), pericytes (PC), basal lamina (BL), and astrocytes (AC). Adapted from Hawkins et al 2005 (8).....	3
Figure 1-2: Photomicrograph of (a) normal mice brain vasculature, and (b) a glioma xenograft in an immunodeficient mouse brain. The normal vasculature is optimally organized, appropriately connected and shaped to provide nutrients to all parenchymal cells, whereas the cancer vasculature is disorganized, poorly connected, and tortuous. Adapted from Jain et al. 2007 (50). .....	6
Figure 1-3: Mechanisms of vascular, transvascular, and interstitial transport in a tumor tissue unit consisting of blood vessels and the surrounding tissue. Adapted from Chauhan et al. 2011 (65). .....	8
Figure 1-4: Interstitial fluid pressure profile in the subcutaneous rat tumor, indicating a sharp increase at the periphery and reaching a plateau within the core of the tumor. Adapted from Chauhan et al. 2011 (59). .....	10
Figure 1-5: Proposed mechanisms which result in ultrasound induced blood brain barrier disruption in the presence of microbubbles: A) radiation forces, B) bubble oscillation, and C) acoustic streaming. Adapted from (76). .....	11
Figure 1-6: Focal contrast enhancement from dynamic contrast enhanced magnetic resonance imaging (DCE-MRI) after focused ultrasound with MB administration (FUSwMB) induced blood-brain-barrier (BBB) disruption in a rat at four frequencies: A) 0.26 MHz, B) 0.69 MHz, C) 1.63 MHz, and D) 2.07 MHz. Adapted from Hynynen et al. 2006 (92).....	14
Figure 1-7: A commonly used pulse sequence for focused ultrasound with microbubble administration (FUSwMB) induced blood-brain-barrier (BBB) disruption with a burst length (BL) of 10 ms, a pulse repetition frequency (PRF) of 1 Hz, for a 1% duty cycle. ....	16

Figure 1-8: A schematic of the general closed two-compartment model that distributes contrast between the intravascular space and the interstitial space, as two separate ‘well-mixed’ compartments. Adapted from Lee et al. 2003 (127). .....	24
Figure 1-9: A schematic of the Johnson and Wilson distributed parameter model. Adapted from Lee et al. 2003 (127). .....	27
Figure 1-10: The blood flow scaled impulse residue function according to the Johnson and Wilson model. The symbols are defined in the text. Adapted from Lee et al 2003 (127) ....	30
Figure 2-1: Schematic of the setup of a focused ultrasound with microbubble administration (FUSwMB) experiment, showing the rabbit head placed supine on the surface of the water tank of the FUS instrument, with the focal zone of the focused ultrasound transducer targeted in the brain. ....	54
Figure 2-2: Coronal head CT images of a representative rabbit, acquired with Isovue contrast injection, following focused ultrasound with microbubble administration (FUSwMB). The 2x2 voxel arterial input region of interest (ROI) and corresponding arterial time density curve, $Ca(t)$ , along with sonicated and control ROIs in the striata, and their corresponding time density curves $Q(t)$ are presented. ....	57
Figure 2-3: Gadolinium (Gd) enhanced T1-weighted magnetic resonance imaging (MRI) in multiple planes and blood-brain-barrier (BBB) permeability surface area product (PS) maps for two rabbits that demonstrated BBB disruption. In MR images, the regions of increased BBB permeability are indicated with blue arrows. ....	62
Figure 2-4: Total applied sonication energy ( $E_{\text{applied}}$ ) plotted against peak permeability surface area product (PS) for all sonications with 0.5 – 0.6 W applied power. The sonications are grouped by the presence of lesions (red) or no lesions (blue) at gross histology, and sonication times of 120 s or less (circles), or 150 and 180 s (triangles). ....	63
Figure 2-5: The average blood-brain-barrier (BBB) permeability surface area product (PS) vs. time curves for the sonicated and contralateral (control) hemispheres in the rabbits, grouped by those that demonstrated visible lesions over the sonicated region at gross histology (n=8), and those that did not (n=4). Error bars indicate standard deviations.	

\*Significantly different from baseline value as determined by paired t-tests with Bonferroni correction for multiple comparisons. .... 64

Figure 2-6: The coronal blood-brain-barrier (BBB) permeability surface area product (PS) maps over time for a rabbit sonicated for 180s at an applied acoustic power of 0.6W that demonstrated reversible increased BBB permeability, Evans Blue (EB) dye leakage, and no visible lesions over the sonicated region..... 65

Figure 2-7: Receiver operating Curve (ROC) and the corresponding area under the curves (AUC) for logistic regressions of Evans Blue (EB) leakage with (a) peak permeability surface area product (PS) and 3-hour post PS; the presence of a lesion with (b) peak PS and 3-hour post PS; (c) the presence of EB leakage with applied sonication power and energy, and (d) the presence of a lesion with applied sonication power and energy. The p-value indicates the significance of rejecting the null hypothesis that  $AUC = 0.5$ . .... 67

Figure 2-8: Blood-brain-barrier (BBB) permeability surface area product (PS) maps at 15 min post sonication and gross histology results for 3 cases using acoustic power of 0.5 – 1.0 W and the same sonication time of 180 s. .... 69

Figure 2-9: Hematoxylin–eosin (H&E) stained tissue sections (a-c) for the 3 cases shown in Figure 2-8. The middle (d-f) is 10X magnification for corresponding sections (a-c). The bottom row is 120X magnification of distinct pathologies in the case sonicated at 1.0 W (c & f): (g) regions of scattered microhemorrhages without neuronal degeneration (short arrows), (h) more severe hemorrhagic regions accompanied by selective neuronal necrosis (dark-stained neurons, long arrows), and (i) ischemic regions accompanied by neuronal necrosis (hollow arrows). .... 70

Figure 3-1: Schematic of the experimental setup - the rat head was placed supine on the surface of the water tank, with the focal zone of the focused ultrasound transducer (FUS) aligned to the tumor..... 82

Figure 3-2: Coronal head CT images of a rat following administration of contrast agent (Isovue). Two slices of the head prior to FUSwMB are shown. A 2x2 voxel arterial input region of interest (ROI) and the corresponding arterial time density curve,  $Ca(t)$ , along with tumor ROI and corresponding tumor time density curve  $Q(t)$  are presented..... 84

Figure 3-3: Serial tumor and control Isovue permeability surface area product (PS), cerebral blood flow (CBF), and cerebral blood volume (CBV) measured in the acute group before and over 4 hours following FUSwMB (n=5). \*Significantly different from baseline as determined by Mann-Whitney U test ( $p < 0.05$ ) after Bonferroni correction for multiple comparisons... 87

Figure 3-4: Native CT Image, permeability surface area product (PS), cerebral blood flow (CBF), and cerebral blood volume (CBV) map for a representative animal in the acute group following FUSwMB. Average tumor value is shown beneath each map. .... 88

Figure 3-5: Serial tumor permeability surface area product (PS), cerebral blood flow (CBF), and cerebral blood volume (CBV), measured with Isovue (760 Da), and eXia (~65 kDa), in the recovery group before and over 72 hours following FUSwMB (n=10). \*Significantly different from baseline as determined by Mann-Whitney U test ( $P < 0.05$ ) after Bonferroni correction was applied..... 90

Figure 3-6: Permeability surface area product (PS) maps, measured with Isovue (760 Da), and eXia (65 kDa) contrast agents, for a representative animal in the recovery group before and following FUSwMB. .... 91

Figure 3-7: Comparison of Isovue (760 Da) and eXia (65 kDa) permeability surface area product (PS) for all 10 subjects (top left). Comparison of cerebral blood flow (CBF) for all 10 subjects (middle left with an identity line (red)), cerebral blood volume (CBV) for all 10 subjects (middle right with an identity line (red)), and Bland Altman plots for agreement between Isovue and eXia measured CBF (bottom left), and CBV (bottom right) for all 10 subjects..... 92

Figure 3-8: The percent error in using permeability surface area product (PS) to approximate the flow extraction product (FE), as shown in Equation 3-4, plotted for different ratios of F/PS. .... 99

Figure 4-1: A schematic diagram for the blood flow (F) scaled impulse residue function,  $R(t)$ , where E is extraction efficiency,  $T_0$  is the time for the contrast to appear, W is the mean transit time, and  $k_2$  is the rate constant that defines transfer from the interstitial space back into the vasculature..... 114

Figure 4-2: Serial tumor PS, extravascular contrast distribution volume (Ve), cerebral blood flow (CBF), and cerebral blood volume (CBV), measured using Isovue (760 Da) contrast agent, out to 72 hours following FUSwMB (n=10). *Significantly different from baseline value as determined by Bonferroni corrected non-parametric t-tests. ....	118
Figure 4-3: Serial tumor longitudinal relaxation time (T1) and fluid attenuated inversion recovery (FLAIR) signal intensity (SI) out to 72 hours following FUSwMB (n=4). ....	118
Figure 4-4: CT Perfusion derived Isovue PS maps, and MRI longitudinal relaxation time (T1), and fluid attenuated inverted recovery (FLAIR) maps for a rat following FUSwMB. ....	119
Figure 4-5: Correlation of CT Perfusion derived extravascular distribution volume (Ve) with MRI longitudinal relaxation time (T1), and fluid attenuated inverted recovery (FLAIR) signal intensity (SI) in 4 rats at baseline, 24 hr, and 72 hr post sonication. ....	119
Figure 4-6: Boxplots of the total number of intact and collapsed CD31 expressing vessels for all 5 fields in the sonicated (r=4) and control (r=3) groups. #Significantly different than the control group, P < 0.05. *Significant difference between the number of intact and collapsed CD31 expressing vessels, P < 0.05. ....	121
Figure 4-7: Representative immunohistochemical stained tumor regions showing intact (hollow arrow) and collapsed (filled arrow) CD31 expressing vessels, as well as vimentin expression score, in the sonicated (n=4) and control groups (n=3). The representative vimentin expression shown was scored as 3 in the sonicated group, and as 1 in the control group.....	122

## Abstract

AIC	Akaike's information criterion
AUC	Area under the curve
BBB	Blood brain barrier
BCNU	Carmustine
BL	Burst length
BTB	Blood tumor barrier
$C_a(t)$	Arterial input function for injected contrast
$C_b(t)$	Blood contrast concentration over time
$C_c(t)$	Tissue contrast concentration over time
CBF or F	Cerebral blood flow
CBV or $V_b$	Cerebral blood volume
CED	Convection enhanced diffusion
CMT	Carrier mediated transport
CNS	Central nervous system
CT	Computed tomography
DC	Duty cycle
DCE	Dynamic contrast enhanced
DCE-CT	Dynamic contrast enhanced computed tomography
DCE-MRI	Dynamic contrast enhanced magnetic resonance imaging
E	Extraction efficiency
$E_{\text{applied}}$	Applied sonication energy
EB	Evans blue
FE	Flow extraction product
FLAIR	Fluid attenuated inverse recovery sequence
FUS	Focused ultrasound
FUSwMB	Focused ultrasound with microbubble administration
GBM	Glioblastoma multiforme
Gd	Gadolinium
GFAP	Glial fibrillary acidic protein
ICV	Intracerebroventricular infusion

IFP	Interstitial fluid pressure
IRF or R(t)	Impulse residue function
$J_c$	Convective solute transfer flux
$J_d$	Diffusive solute transfer flux
$J_t$	Total solute transfer flux (diffusive + convective)
JW	Johnson & Wilson distributed parameter model
JWL	Johnson-Wilson-Lee model
$K_{trans}$	Volume transfer constant
MB	Microbubbles
MRI	Magnetic resonance imaging
MTT or $T_c$	Mean transit time of blood flowing through capillaries
MW	Molecular weight
PRF	Pulse repetition frequency
PS	Permeability surface area product
RF	Radiofrequency
ROC	Receiver operator curve
ROI	Region of interest
RMT	Receptor mediated transport
$V_e$	Extravasation distribution volume
VEGF	Vascular endothelial growth factor

# Chapter 1

## 1 Introduction

### 1.1 Overview

The blood-brain-barrier (BBB) is made up of endothelial tight junctions and associated anatomical structures including the basement membrane, astrocyte foot processes, and pericytes. It is important for maintaining homeostasis in the brain by tightly regulating neurovascular exchange at the endothelium. Only small lipophilic molecules (<500 Da) are able to freely diffuse across the BBB, meaning that the vast majority of intravenously delivered drugs never make it into the brain. As a result, it is widely acknowledged that the BBB is the single most limiting factor in the delivery and development of neurotherapeutics. Recently, it has been demonstrated that the combined use of focused ultrasound (FUS) and intravenously injected microbubbles (MB) is able to non-invasively and transiently disrupt the intact BBB, allowing for the localized delivery of a range of molecules, from small chemotherapeutic agents, to large antibody based drugs, and even nanoparticles. In brain tumors, such as glioblastoma multiforme (GBM), the permeable blood-tumor-barrier (BTB) presents its own challenges in drug delivery due to the build up of interstitial fluid pressure in and around the tumor. For the clinical translation of such a promising drug delivery strategy - it is important to identify vascular parameters that can be used to monitor the exchange of drug between blood vessels and tissue, and predict delivery following FUS sonication with MB administration (FUSwMB). Computed Tomography (CT) Perfusion is a quantitative and functional imaging technique that lets us serially evaluate vascular parameters such as cerebral blood flow (CBF), cerebral blood volume (CBV), and most importantly for this application – permeability surface area product (PS), which approximates the unidirectional flux of blood solutes into tissue. This thesis focuses on using CT Perfusion to quantify the changes in PS following FUSwMB in pre-clinical models, and how these changes relate to drug delivery in the normal intact BBB, and across the BTB in a rat glioma model. This introductory chapter provides an overview of the basic biology and physiology of the BBB and BTB, the mechanisms and current literature for mediated drug delivery

studies with and without FUSwMB, the imaging techniques that will be used in our investigation, followed by an outline of this thesis.

## 1.2 Blood-Brain-Barrier (BBB)

The BBB consists of a series of endothelial tight junctional complexes and associated structures which among other functions, regulate the permeability of solute exchange between the blood and brain tissue (1). These endothelial complexes and structures, each consisting of endothelial cells with proteins sealing the gaps between them, basement membrane, astrocytic foot processes, pericytes, and microglia, together with neurons form the neurovascular unit (2). A schematic of a cerebral capillary cross sectional is shown in Figure 1-1. Attached to the abluminal surface of the endothelium are connective tissue cells known as pericytes (3,4). The pericytes and the endothelium are then surrounded by the basal lamina, which is 30 to 40-nm thick membrane comprised of a number of connective tissues and extracellular matrix proteins (5). Contiguous with the basal lamina, is the plasma membrane of astrocytes, which ensheathes cerebral capillaries and serve many physiological functions regulating the vasculature and neuronal cells (6,7).

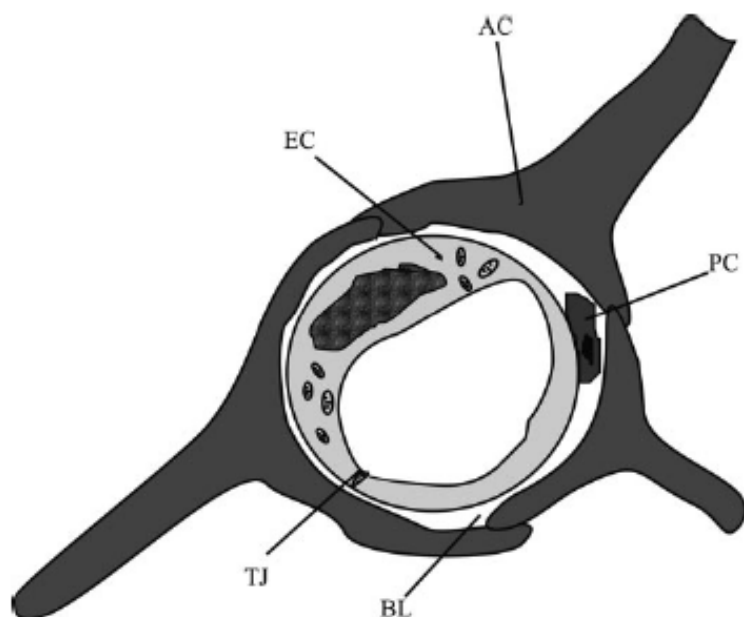


**Figure 1-1: Schematic cross-sectional representation of a cerebral capillary, highlighting a single endothelial cell (EC), the tight junctions (TJ), pericytes (PC), basal lamina (BL), and astrocytes (AC). Adapted from Hawkins et al 2005 (8).**

Functions of the BBB in the neurovascular unit include: 1) maintaining central nervous system (CNS) homeostasis, 2) isolating the brain from other body compartments, 3) providing a constant supply of oxygen and nutrients by specific transport systems, and 4) directing inflammatory cells in response to changes in the local environment (2,9).

These physical and transport barriers work together to maintain and regulate BBB permeability. Since no brain cell is more than 25  $\mu\text{m}$  from basement membrane of the BBB, and the endothelial cytoplasm at the abluminal surface of the BBB spans 200-300nm, the BBB is an ideal target to enhance the delivery of drugs into the brain. (10).

### 1.3 Drug Delivery across the BBB

Around 98% of all small molecules are not able to cross the BBB, and into the brain interstitium (11). A comprehensive review of over 6000 drugs found that only 1% were delivered and demonstrated activity in the CNS (12). The absence of para-cellular or trans-cellular channels that are seen in other endothelium throughout the body means that

molecules in the vasculature may only cross the BBB via one of two mechanisms: 1) Free diffusion of lipid soluble molecules, typically with a molecular mass of less than 500 Da, through the lipid bilayer of the endothelium, and 2) carrier- or receptor- mediated transport (CMT or RMT) through the barrier.

CMT is facilitated by diffusion of certain solutes across the BBB. The solute binds to a transporter on one side of the BBB, triggering a conformational change in the carrier protein, resulting in a transfer of solute across the barrier, from high to low concentration. CMT contributes to the transport of small molecules such as small peptides, glucose, amino acids, and monocarboxylates (13). RMT occurs via bulk- or fluid-phase endocytosis and provides a means to transport macromolecules into the CNS. Although fluid-phase endocytosis is relatively non-specific, RMT is highly selective and occurs to a very limited degree across the BBB for certain ligands, hormones, growth factors, enzymes, and plasma proteins (14). Endogenous RMT systems can also allow for the reengineering of recombinant proteins or peptides using molecular Trojan horses to develop pharmaceuticals that can penetrate the BBB (15). Although CMT and RMT are promising techniques for drug development and delivery across the BBB, their effectiveness is often limited and can benefit in conjunction with other approaches to circumvent the barrier (16).

One strategy for the reversible disruption of the BBB is by the intracarotid arterial infusion of agents such as mannitol (17), vasoactive agents (18), solvents (19), alkylating agents (20), immune adjuvants (21), cytokines (22), and other miscellaneous agents (23). The major limitation of these techniques is the non-localized disruption of the BBB, which can increase neuronal toxicity from the drug delivered (24). More-invasive neurosurgical transcranial drug delivery techniques such as: 1) intracerebral implantation (25), 2) intracerebroventricular infusion (ICV) (26), or convection enhanced diffusion (CED) (27) are also used when justified because of the risk associated with surgery. The first two approaches involve direct injection of the drugs into the brain and ventricles and subsequent diffusion into neighboring brain tissue, whereas CED forces drug containing fluid into the brain against the concentration gradient.

## 1.4 Malignant Gliomas

More than 20,000 North Americans are diagnosed annually with primary malignant brain cancers (28). Gliomas, which represent the majority of brain tumors, are derived from glial cells that maintain the BBB homeostasis as well as other functions in the central nervous system (29,30). They are divided into astrocytic and oligodendroglial subtypes, and are classified as grades I to IV based on their growth rates (31). High-grade or malignant gliomas, which account for approximately 70% of all malignant brain tumors, have particularly poor prognosis (32). Glioblastoma multiforme (GBM), characterized by increased mitotic activity, proliferation of the microvasculature, and necrosis, is the most severe grade, with median survival between 12 to 15 months (31).

Because of their neovascular and infiltrative nature, GBM treatment may vary based on the type, location, and grade of the tumor, and involves combination of debulking surgery when possible, followed by chemotherapy and/or radiation (33). Surgical resection to palliate symptoms and improve function when feasible is the first line standard of care, followed by 40 to 60 Gy fractionated radiotherapy and concurrent Temozolomide at a dose of 75 mg/m<sup>2</sup> per day, beginning within six weeks of surgery. Following this concurrent treatment, cycles of adjuvant chemotherapy cocktails can be administered for improved outcomes, with risk of side effects being a limiting factor.

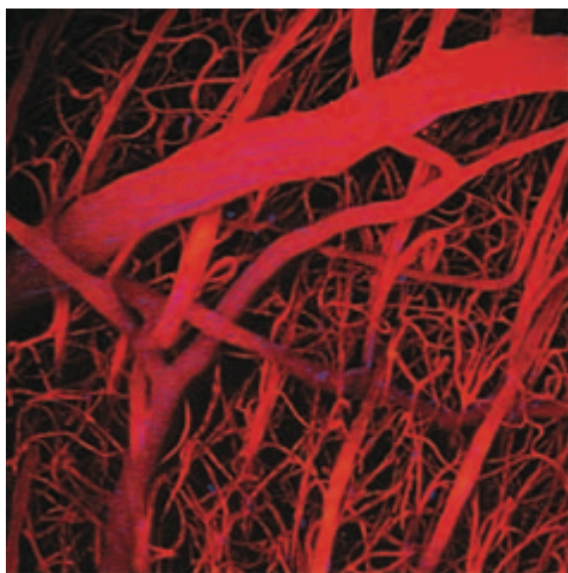
Adjuvant Temozolomide chemotherapy is commonly combined with carmustine, a mixture of procarbazine, lomustine, and vincristine (34), or more recently, bevacizumab (35,36). However, recent phase 3 clinical trials suggest that these chemotherapy cocktails provide a limited response, prolonging progress free or overall survival by only a matter of months (37,38). In addition, the risk of systemic toxicity often limits the administered dose and effectiveness of the treatment (39).

### 1.4.1 Blood-Tumor-Barrier

When a primary brain tumor grows beyond 1-2 mm in diameter within the brain parenchyma, the BBB becomes structurally and functionally compromised (40–42). As the tumor continues to grow and infiltrate into surrounding normal brain, other pathological features include marked angiogenesis and endothelial proliferation, tissue

hypoxia, and eventually tumor necrosis also arise (43–45). In high grade gliomas, vessels become tortuous, disorganized, highly permeable, and are characterized by abnormalities in their endothelial wall, basement membrane, and pericyte coverage (46,47), as seen in Figure 1-2. In patients and pre-clinical models, tumors as compared to normal vessels also have structurally abnormal and significantly larger diameters and thicker basement membranes (48,49).

**a Normal brain vessels**



**b Brain tumour vessels**

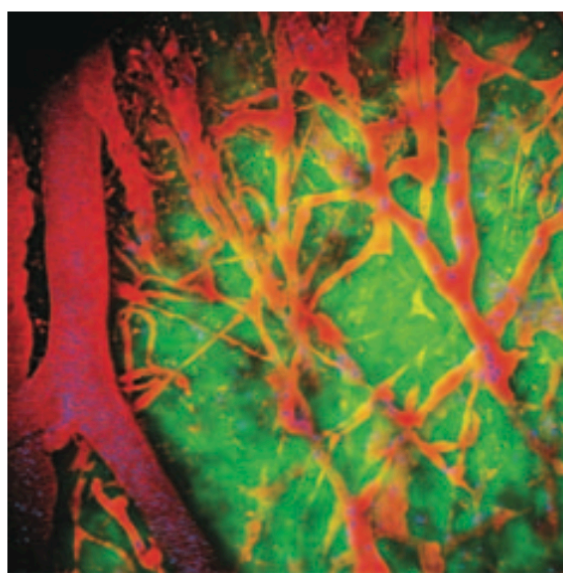


**Figure 1-2: Photomicrograph of (a) normal mice brain vasculature, and (b) a glioma xenograft in an immunodeficient mouse brain. The normal vasculature is optimally organized, appropriately connected and shaped to provide nutrients to all parenchymal cells, whereas the cancer vasculature is disorganized, poorly connected, and tortuous. Adapted from Jain et al. 2007 (50).**

The structural abnormalities present in the BTB also lead to abnormal function, characterized primarily by the increase in vascular permeability. Although some BBB function is retained, evident by the reduced transvascular transport in intracranial tumors compared to subcutaneous ones (41,51), brain tumor vessels contain endothelial pores as large as 550 nm in diameter (52). It's important to note that the loss of BBB integrity is not uniform, but temporally and spatially heterogeneous as tumors progress (53). The

heterogeneous leakiness of brain tumor vessels cause abnormal blood flow, which leads to abnormal delivery of oxygen, leading to hypoxia, as well as the spatially and temporally heterogeneous delivery and distribution of blood-borne drugs throughout the tumor (54).

The abnormal BTB permeability is also accompanied by other pathophysiological states in the tumor microenvironment, including accumulated solid stress (55–58), elevated interstitial fluid pressure (54,59–61), and a dense interstitial structure (62–64). These abnormalities contribute to variable avascular regions, sluggish and non-uniform perfusion, diminished trans-vascular pressure gradients, and highly viscoelastic interstitial components that hinder drug penetration and delivery (65).

### 1.4.2 Drug Delivery in Brain Tumors

All systematically administered cancer therapeutic agents must follow a long and complex journey from the point at which it enters the circulation, up until it reaches its target (65,66). There are three major transport processes that govern this delivery leading up to uptake by the target: 1) vascular transport, 2) transvascular transport, and 3) interstitial transport, as shown in Figure 1-3. In normal vasculature, these transport processes are highly efficient, effectively delivering oxygen and nutrients throughout the brain.

Vascular transport is defined as the convective delivery of drugs into different regions of the tumor, driven by blood flow. It can be defined by the volumetric flow rate,  $Q$ , in blood vessels supplying the volume of tissue and is equal to the pressure drop ( $\Delta p$ ) divided by the resistance of the blood vessels ( $R$ ). The rate of drug delivery to the tumor is defined as the flux of drug  $J_v$  into a tissue region, which is equal to  $Q$  multiplied by the drug concentration in the feeding blood vessels  $C_v$ , or  $J_v = QC_v$ .

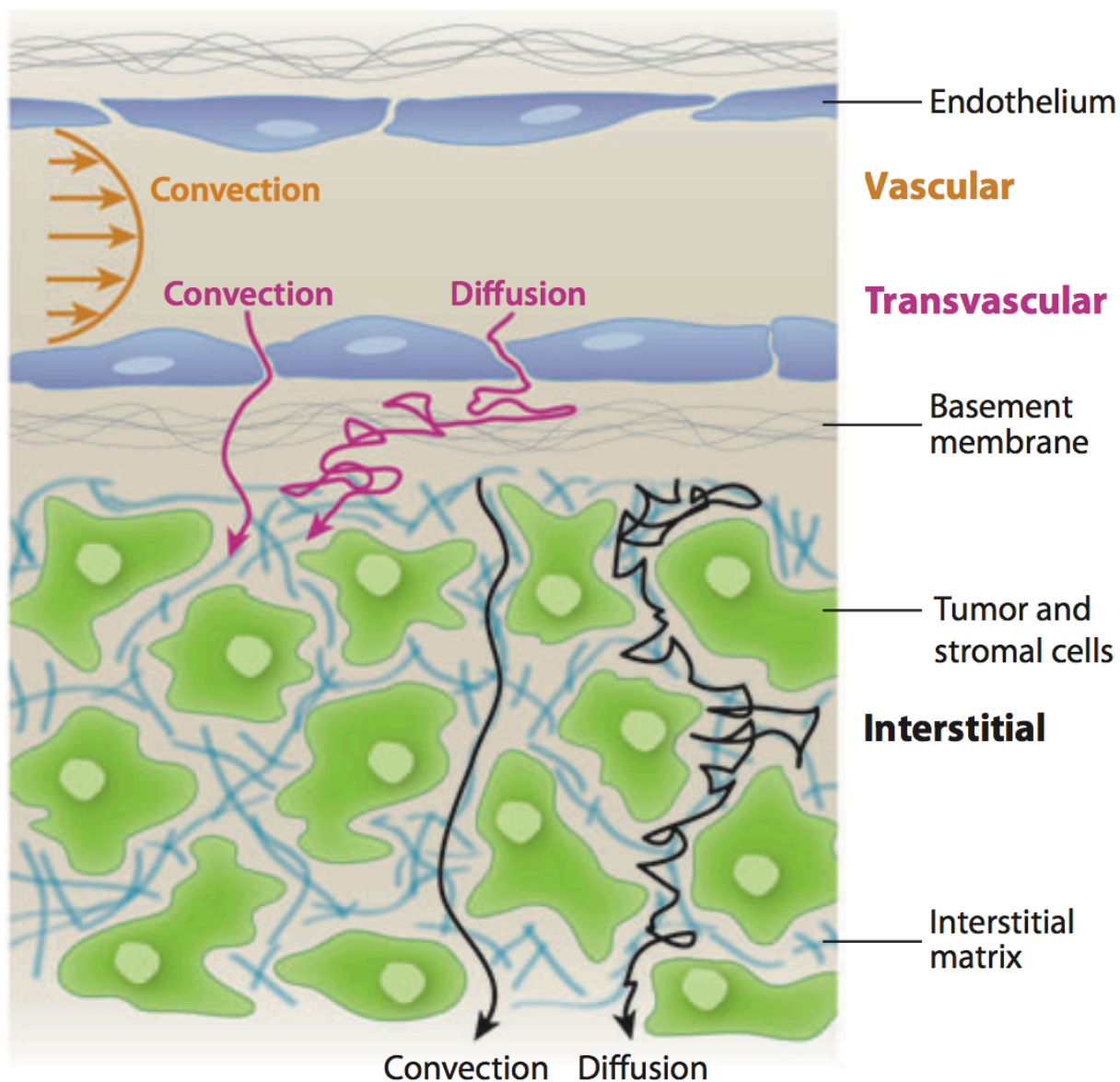


**Figure 1-3: Mechanisms of vascular, transvascular, and interstitial transport in a tumor tissue unit consisting of blood vessels and the surrounding tissue. Adapted from Chauhan et al. 2011 (65).**

The net flux of drug delivery across the BBB is governed by the transvascular transport process. In the brain, transvascular flux of drug  $J_t$ , is a combination of diffusive flux  $J_d$ , and convective flux  $J_c$ .  $J_d$  is dependent on the difference between the plasma concentration  $C_b$ , and the interstitial concentration  $C_e$ , multiplied by the proportionality constants, vascular diffusive permeability  $P_d$ , and the vascular surface area  $S_v$ .

$$J_d = P_d S_v (C_b - C_e) \quad \dots \text{Equation 1-1}$$

Similarly,  $J_c$  is calculated as,

$$J_c = L_t S_v (1 - \sigma_s) (\Delta p_t - \sigma \Delta \Pi) \quad \dots \text{Equation 1-2}$$

where  $L_t$  is the hydraulic conductivity across the BBB,  $\Delta p$  is the transmural hydrostatic pressure gradient,  $\Delta \Pi$  is the transmural osmotic pressure gradient,  $\sigma$  is the osmotic reflection coefficient, and  $\sigma_s$  is the solute's reflection coefficient.

The diffuse permeability,  $P_d$ , and hydraulic conductivity,  $L_t$ , are dependent on biophysical properties of the endothelium and basement membrane, including viscoelasticity and porosity, as well as physiochemical properties of the drug or drug carrier itself, including size, charge, and configuration.

A major barrier for drug delivery in tumors is caused by the build-up of solid stress from uncontrolled proliferation of tumor cells. This also compresses lymphatic vessels which become unable to drain the tumor of accumulating fluid and plasma macromolecules in the tumor interstitium, leading to vasogenic edema (67). With no drainage and small to no transmural oncotic pressure difference, the interstitial fluid pressure (IFP) rises to the microvascular pressure, abolishing the transvascular pressure gradient required for convective transport across the BTB (66), as per Equation 1-2, and is shown in Figure 1-4.

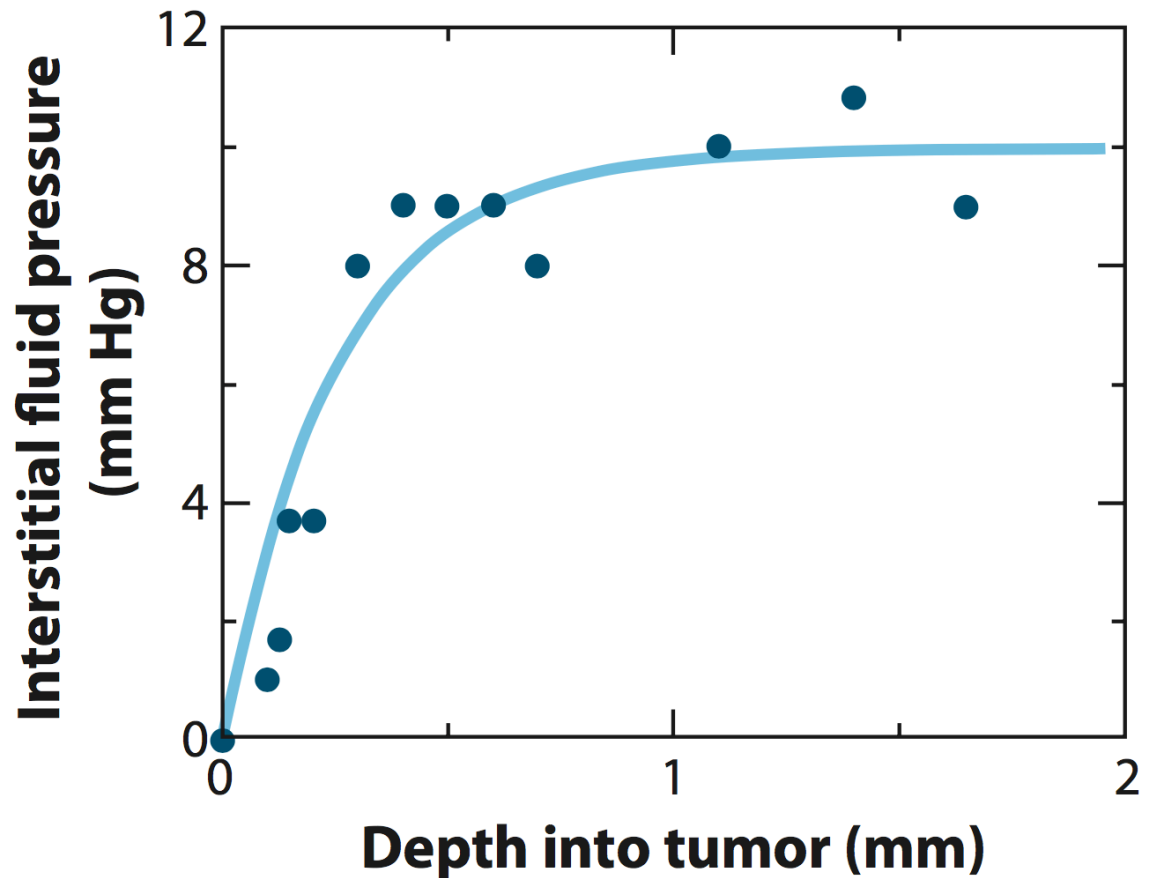


**Figure 1-4: Interstitial fluid pressure profile in the subcutaneous rat tumor, indicating a sharp increase at the periphery and reaching a plateau within the core of the tumor. Adapted from Chauhan et al. 2011 (59).**

Since smaller molecules such as Temozolomide (214 Da) are able to diffuse across the permeable BBB/BTB, this increase in IFP is more problematic for the delivery of larger molecules that rely more heavily on convective transport through the permeable barrier. Convective transport is particularly of interest for delivery of monoclonal antibody based cancer therapeutics, such as Bevacizumab (149 kDa), and Trastuzumab (145 kDa) because of their large size.

## 1.5 FUS and MB induced BBB Disruption

Recent advances in acoustic technology have opened the doors for a novel strategy to temporarily disrupt the BBB in targeted regions of the brain using pulsed FUS, allowing for increased endothelial permeability and therefore drug delivery (68–75). FUS concentrates acoustical energy in a small volume, with minimal effects to neighboring tissue, and can be used to non-invasively induce biological effects in the body. In the presence of intravenously injected gas-filled encapsulated MB, FUS can be used to transcranially and reversibly disrupt the vasculature within the focal spot of the ultrasound transducer. FUSwMB offers a means to effect non-invasive localized opening of BBB and hence delivery of small- or large- molecule drugs, allowing for the development of pharmaceuticals for brain tumors and most CNS disorders (76).

The observed BBB effects from FUSwMB are predominantly due to cavitation, which is an acoustically induced oscillation of MB within the vasculature, resulting in shear stress on the luminal surface of the capillary endothelium (77).

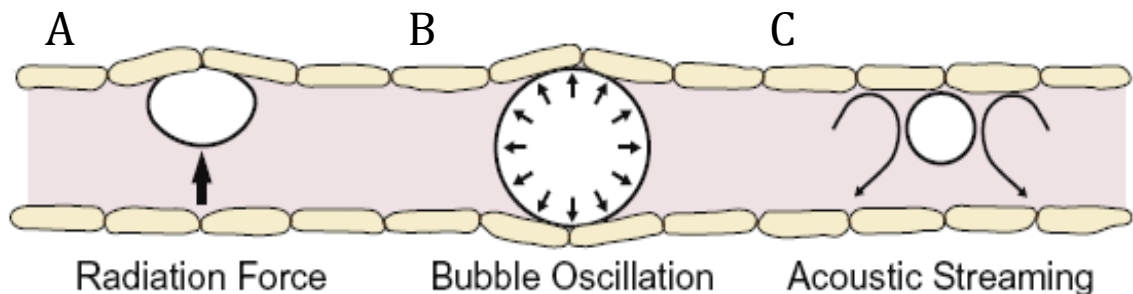


**Figure 1-5: Proposed mechanisms which result in ultrasound induced blood brain barrier disruption in the presence of microbubbles: A) radiation forces, B) bubble oscillation, and C) acoustic streaming. Adapted from (76).**

In actual fact, the BBB effect may be attributed to a combination of cavitation, acoustic streaming, and radiation forces, as shown in Figure 1-5 (77). At relatively low acoustic pressure, MB oscillate within the ultrasound field, which is called “stable” cavitation. The biological effects, including disruption of the BBB, observed on vascular endothelium from stable cavitation can be mostly attributed to direct shear stress, and an

eddy micro-streaming of the fluid resulting from the oscillating bubble (78–80). For the endothelium to be affected, it must be in contact or near to the oscillating bubbles, which is achieved by the acoustic radiation force that pushes bubbles against the endothelium (81). At high acoustic pressures, the bubbles undergo “inertial” cavitation, expanding and collapsing rapidly causing them to burst, which can create high local temperatures and pressures, velocity jets, and the generation of free radicals (80).

At higher power and duty cycles (the fraction of time ultrasound is turned on), FUSwMB can also lead to thermal effects. At temperatures greater than approximately 60°C, FUS can be used as a thermal ablation method and has been used to treat tumors in many organs including the liver, breast, kidney, bone, uterus and pancreas (70,82–85). It has also been used as a technique of inducing thermal coagulation in blood vessels (86–90).

## 1.6 The effect of FUS parameters on BBB Disruption

Much of the early work on BBB disruption mediated by FUSwMB has been focused on optimizing the pulsed FUS exposure parameters in order to produce consistent, localized, and persistent BBB disruption, with minimal damage to the brain. There are several key FUS and MB parameters that can influence the type and extent of the induced BBB disruption. These include the frequency of the ultrasound, the applied pressure amplitude or acoustic power, pulse sequence parameters such as burst length (BL), pulse repetition frequency (PRF), and duty cycle (DC), exposure time, and contrast agent parameters such as size, concentration, and dose of the MB (68–75).

The pre-clinical RK-100 system developed by FUS Instruments Inc. was used for all experiments included in this thesis. The ultrasound was generated using a spherically focused piezoceramic transducer ( $f_0=0.563$  MHz), with a 7 cm diameter, and a focal length of 5.6 cm. The transducer was driven by a function generator generating sinusoidal excitations, which were amplified with a radiofrequency (RF) power amplifier.

### 1.6.1 Transducer Frequency

Since we are working with a non-invasive transcranial approach, identifying the right transducer frequency range is necessary for adequate depth penetration and energy

deposition in the focal zone. High transducer frequencies are not optimal for transcranial FUS applications because of the decreased size of the focal volume, distortion of the FUS beam, and possible over-heating due to high absorption by the bone (91). A study published by McDannold et al. in 2008 comparing the effect of five transducer frequencies, 0.26, 0.69, 1.5, 1.63, and 2.1 MHz, found BBB disruption was observed in frequencies as low as 0.260 MHz, without any ischemia, apoptosis, or any long-term damage from histology (92). Interestingly, a study published in 2010 by Liu et al. using a planar pinhole ultrasound transducer was able to achieve BBB disruption at a frequency as low as 26 kHz (93). Figure 1-6 demonstrates local BBB disruption using contrast enhanced T1-weighted magnetic resonance imaging (MRI) in a rabbit brain at four ultrasound frequencies (92).

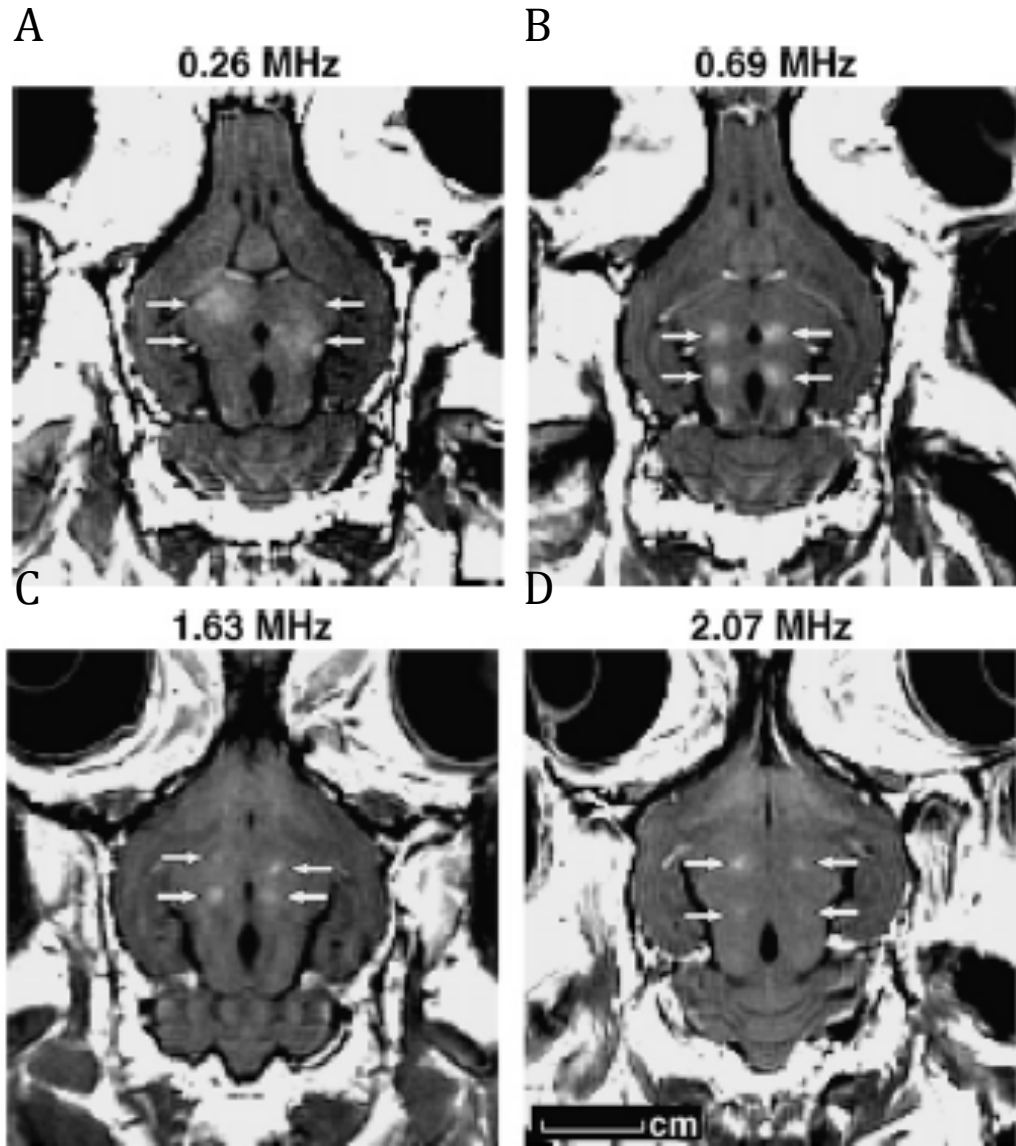


**Figure 1-6: Focal contrast enhancement from dynamic contrast enhanced magnetic resonance imaging (DCE-MRI) after focused ultrasound with MB administration (FUSwMB) induced blood-brain-barrier (BBB) disruption in a rat at four frequencies: A) 0.26 MHz, B) 0.69 MHz, C) 1.63 MHz, and D) 2.07 MHz. Adapted from Hynynen et al. 2006 (92).**

### 1.6.2 Applied Pressure Amplitude or Power

The applied pressure amplitude, also described by the acoustic power, controls the effect on the MB, and has effect on the BBB within the focal zone. A study in 2008 by

McDannold et al. investigated the induced BBB disruption for a range of applied powers (0.1-1.6 W), while all other parameters were held constant, and found that increasing the power increases the likelihood of causing BBB disruption. A summary of this result is shown in Table 1-1 (71).

**Table 1-1: The effect of a range of applied acoustic powers on blood-brain-barrier (BBB) disruption, while other parameters were held constant. All sonications had a duration of 20 s, and were performed using 50 ul/kg Optison microbubbles.**

Acoustic Power (W)	Ultrasound Frequency (MHz)	Burst Length (ms)	PRF (Hz)	Percentage with BBBD	Mean signal enhancement in MRI
0.1	0.69	0.1	1	20% (1/5)	0.8 ± 2.0%
0.2	0.69	0.1	1	17% (1/6)	3.2 ± 4.2%
0.3	0.69	0.1	1	60% (3/5)	7.2 ± 4.9%
0.4	0.69	0.1	1	100% (4/4)	12.6 ± 2.3%
0.5	0.69	0.1	1	100% (4/4)	13.1 ± 3.1%

### 1.6.3 FUS Pulse Sequence

Another important factor in FUS is the pulse sequence used, which is defined by three main parameters: 1) burst length (BL), which is the duration for which ultrasound is on in each pulse, 2) pulse repetition frequency (PRF), which is the number of pulses applied per second, and 3) duty cycle, which is the percentage of the total duration for which the ultrasound is on. An example of a commonly used pulse sequence for FUSwMB induced BBB disruption is shown in Figure 1-7.

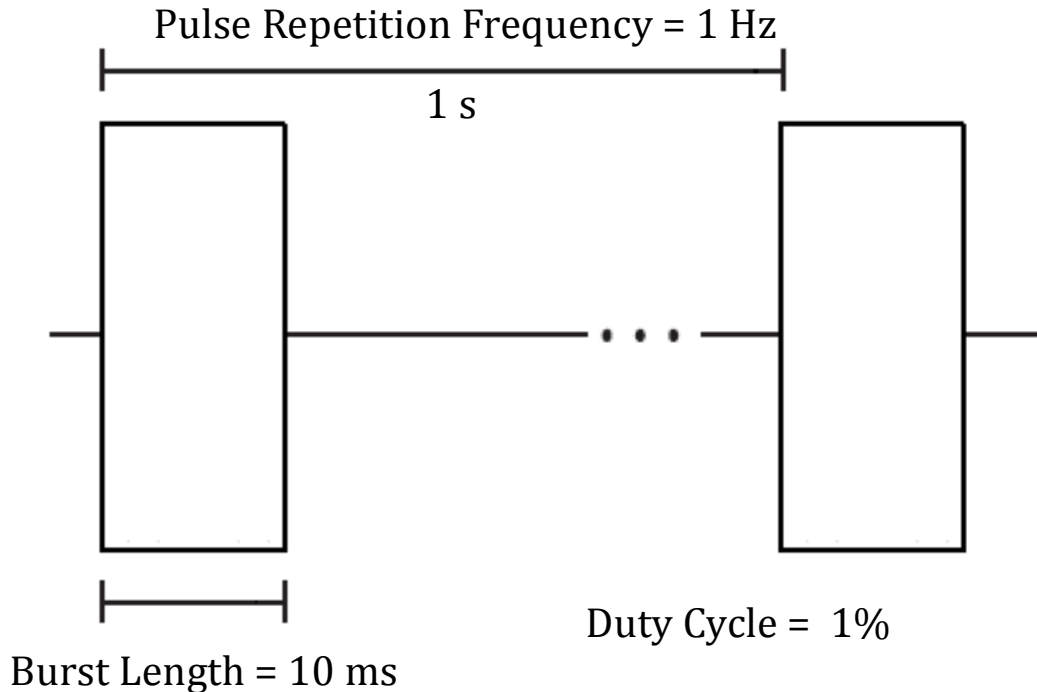


**Figure 1-7: A commonly used pulse sequence for focused ultrasound with microbubble administration (FUSwMB) induced blood-brain-barrier (BBB) disruption with a burst length (BL) of 10 ms, a pulse repetition frequency (PRF) of 1 Hz, for a 1% duty cycle.**

Several studies have aimed to characterize the effects of various pulse sequences on BBB disruption. A study by McDannold et al. in 2008 concluded that reducing the BL from 10 ms to 0.1 ms significantly reduced the MRI contrast enhancement, a surrogate of BBB disruption, whereas altering the PRF alone had no effect on BBB disruption, at least over a particular range from 0.5 to 5 Hz (71). In 2011, Choi et al. published a study which demonstrated the trans-BBB delivery of 3-kDa dextran at BLs as short as 0.03 ms, with increased delivery of dextran as the BLs were increased up to 30 ms (94). However, more heterogeneous distribution of dextran was also observed at higher BLs. Also in 2011, O'Reilly et al. published a similar study using a new accurately timed short burst of 3  $\mu$ s, with burst delays ranging from 6 to 600  $\mu$ s within the BL of each pulse (95). These short bursts and delays were introduced to increase the number of bursts within the previously reported 10 ms BL. A semi-log relationship was found between MRI contrast

enhancement and the number of bursts in a pulse, with a single 3  $\mu$ s burst still capable of inducing BBB disruption. Although no improvements in safety over longer bursts were established, closely-timed micro-pulses, as low as 3  $\mu$ s BL, or even a single shot 3  $\mu$ s pulse, may allow for a greater level of treatment control (95).

#### 1.6.4 Exposure Time

In 2010, Chopra et al. published a study examining the influence of exposure time on BBB disruption in rats in order to help determine the optimal treatment delivery conditions. Using a 1.08 MHz transducer, and at an applied pressure amplitude of 0.38 MPa, it was determined that exposures less than 180 s in duration are associated with a low probability of irreversible damage to brain tissue. Although exposures greater than 300 s were associated with an increased proportion of irreversible brain damage, this may be acceptable for chemotherapy delivery, in which tissue destruction is one of the therapeutic goals. It was also found that weekly repeat exposures were feasible, but resulted in evidence of tissue damage over the focal volume in 50% of the animals (72).

### 1.7 The effect of MB on FUS

The use of MB allows for nucleation of cavitation sites to disrupt the BBB. This allows us to significantly reduce the applied acoustic energy resulting in far greater consistency in BBB disruption, since high intensity ultrasound required to generate cavitation bubbles in the blood are no longer needed (96). Use of MB also improves the practicality and safety of the procedure by reducing the risks of overheating and tissue damage that can result from inertial cavitation (97).

Three commonly used commercially available gas-filled MB are Definity (Lantheus Medical Imaging, USA), Optison (GE Healthcare, USA), and SonoVue (Bracco International, The Netherlands). A comparison of the physical characteristics of these common MB are presented in Table 1-2.

**Table 1-2: Comparison of three types of microbubbles (MB) that are commonly used for blood-brain-barrier (BBB) disruption; Definity, Optison, and SonoVue.**

MB Type	Shell material	Gas	Mean size (um)	Concentration (bubbles/mL)	MB half-life (mins)
<b>Optison</b>	Albumin	C <sub>3</sub> F <sub>8</sub>	2.0-4.5	5.0-8.0x10 <sup>8</sup>	2.5-4.5
<b>Definity</b>	Phospholipid	C <sub>3</sub> F <sub>8</sub>	1.1-3.3	1.2x10 <sup>10</sup>	2-10
<b>SonoVue</b>	Phospholipid	SF <sub>6</sub>	2-8	0.9-6x10 <sup>10</sup>	3-6

Several studies have investigated the physical effect MB have on BBB disruption, but only one attempted to characterize the effect of different MB's using the same acoustic parameters. In 2007, McDannold published a study showing that Optison produced a larger effect than Definity for a sonication at 0.5 MPa (71). Since Definity MB's are more concentrated than Optison, the author speculated that this could result from the fact that the lipid shell of Definity being more difficult to oscillate, and thus cavitate, or that the larger bubble size of Optison MB is closer to the resonant size at the transducer frequency, causing a greater cavitation effect. Other studies investigating the effect of MB properties also found that the extent of cavitation, and the induced disruption is bubble-size dependent (79).

However, more investigation is required to understand the effect of each physical MB property has on the mechanism and ultimately extent of BBB disruption. Yang et al. used three doses of SonoVue 150, 300 and 450 µl/kg in a rat brain model, and found increased Evans blue (EB) extravasation with increasing MB doses. They also detected intracerebral hemorrhage with T2-weighted MRI at the higher MB doses, but not at 150 µl/kg. Treat et al. concluded that although increasing the dose of Optison (10 to 50 µl/kg) led to a greater concentration of the chemotherapeutic agent doxorubicin being delivered to the brain, it was also accompanied by more profound indications of tissue damage (98). In another study, McDannold et al. observed that MB dose had no effect on BBB disruption over the range of 50 to 250 µl/kg of Optison (71), while Choi et al. reported that fluorescence intensity of tagged dextran was not significantly different among 10, 50 and 250 µl/kg of Definity at 0.46 MPa (99).

## 1.8 Pre-clinical drug delivery studies using FUS sonication with MB administration

### 1.8.1 Delivery across the Disrupted BBB

BBB disruption induced by FUSwMB has been used in pre-clinical studies to enhance the delivery of a range of molecules across the BBB, including imaging contrast agents (71,72,74,92), neurotherapeutics (100–102), antibodies (73), nanoparticles (103), fluorescence agents and dyes (94,99), and chemotherapeutic agents in tumor models (100,104–109). A summary of the agents delivered is provided in Table 1-3.

**Table 1-3: Pre-clinical studies on delivery of different molecules and cells across disrupted blood-brain-barrier (BBB) following focused ultrasound with microbubble administration (FUSwMB).**

Type	Agent	Size
MRI or SPECT contrast agent	Omniscan (72–74)	573 Da
	Magnevist (92)	938 Da
	<sup>99m</sup> Tc-DTPA (101)	492 Da
	Superparamagnetic iron oxide (111)	50 nm
Dyes and fluorescence agents	Evans Blue (68,106)	~ 70 kDa
	Dextran (94,99)	3 kDa - 70 kDa
Therapeutic compounds	Doxorubicin (98,100–102)	544 Da
	BDNF (112)	27 kDa
Antibody	Herceptin (113)	148 kDa
	D4 rabbit receptor-targeting (73)	42 kDa
Nano particle	Magnetic nanoparticles (114)	74-83 nm
	Gold nanoparticles (103)	50 nm

Due to the range of sizes and types of molecules that can be delivered across a disrupted BBB, created by FUSwMB, it highlights the importance to develop in-vivo imaging tools that can be used to monitor and quantify the increased endothelial permeability, which can act as a quantitative surrogate of the delivery of the intended molecule.

### 1.8.2 Delivery across the BTB in Glioma Models

Drug delivery in tumors is more complex than the normal brain, which has an intact BBB. Over time, the permeable BTB leads to the development of vasogenic edema, which results from plasma plus plasma proteins leaking into the brain parenchyma (67). This edema, combined with the lack of a lymphatic drainage system in the solid tumor mass, elevates the interstitial fluid pressure in and around the tumor –creating a barrier for drug delivery, particularly for larger molecules that are unable to diffuse across the BTB, and must resort to convective fluid transport (66,115). A summary of pre-clinical glioma studies investigating delivery of imaging or therapeutic agents across the BTB, following FUSwMB are listed in Table 1-4.

**Table 1-4: Summary of studies on delivery of imaging or therapeutic agents across the blood-tumor-barrier (BTB) following focused ultrasound with microbubble administration (FUSwMB) (100,104–109,116,117).**

Author	Agent, Tumor	Results
<b>Treat et al, 2012 (109)</b>	Liposomal Doxorubicin (80-90nm), Rat 9L	- FUSwMB + Liposomal Doxorubicin (DOX) reduced tumor growth compared to DOX only - Significant increase in median survival after single treatment
<b>Aryal et al, 2013 (100)</b>	Liposomal Doxorubicin (80-90nm), Rat 9L	- 3x weekly treatment sessions of FUSwMB + DOX provide complete tumor suppression and improve survival nearly 100%
<b>Aryal et al, 2015 (108)</b>	Liposomal Doxorubicin (80-90nm), Rat 9L	- DOX concentrations significantly enhanced compared to control tumor following FUSwMB at days 9,14, and 17 - Volume transfer constant ( $K_{trans}$ ) significantly enhanced compared to control tumor at day 9, but not 14 or 17 - No correlation between DOX delivery and $K_{trans}$ , possibly due to size mismatch of liposomal DOX (~100 nm) and Gadolinium (Gd)-DTPA (938 Da)
<b>Wei et al, 2013 (104)</b>	Temozolomide (194 Da), Rat 9L	- Temozolomide (TMZ) Cerebrospinal fluid (CSF)/plasma ratio up from 23% to 39% in FUS + TMZ group - FUS + TMZ group 7-day tumor progression ratio reduced from 24 to 5, and extended median survival from 20 to 23 days
<b>Liu et al, 2014 (105)</b>	Temozolomide (194 Da), Mice U87	- Local TMZ accumulation increased from 6.98 to 19 ng/g following FUSwMB - Decreased tumor volume and improved animal survival found with increased TMZ doses (up to 15 and 30%, respectively)
<b>Liu et al, 2010 (106)</b>	BCNU (214 Da), Rat C6	- FUSwMB increased delivery by 202%, - FUSwMB prior to BCNU decreased tumor volume (0.05 vs. 0.28 cm <sup>3</sup> at day 31) and animal survival relative to untreated controls (85.9%), compared to BCNU alone - BCNU alone did not decrease tumor volume, but did significantly improve survival (15.7%)
<b>Park et al, 2012 (107)</b>	Trastuzumab (145 kDa), Rat HER2	- From week seven of treatment to end of study, mean tumor volume of FUSwMB + trastuzumab decreased compared to control groups - In combined group, 4/10 tumors completely resolved on MRI, and median survival 32% longer than untreated control group
<b>Chu et al, 2013 (118)</b>	Gd-DTPA (938 Da), Rat C6	- FUSwMB significantly increased permeability of small tumors, measured with R1 relaxometry and area under the curve (AUC) - Accumulation was higher in large tumors, independent of FUSwMB
<b>Yang et al, 2014 (117)</b>	Gd-DTPA (938 Da), Rat F98	- $K_{trans}$ of sonicated tumor was 2.46x higher at 20 min, and 1.78x higher at 24 h post, compared to untreated tumor

## 1.9 Computed Tomography (CT) Perfusion

### 1.9.1 Imaging the Delivery of Blood Borne Solutes across the BBB

Imaging contrast agents, such as gadolinium based Omniscan and Magnevist has been commonly used to investigate and characterize BBB disruption (71,72,74,92).

Furthermore, tracer kinetic analysis of dynamic contrast enhanced (DCE) studies can provide more quantitative and functionally relevant information about the cerebrovascular system, in particular,  $K_{trans}$ , which is the volume transfer rate of solutes from blood to extravascular extracellular space in the brain parenchyma (interstitium) and is related to the permeability surface area product (PS) of endothelial permeability (P) and surface area (S) of the perfused blood vessels. This transport parameter more accurately measures BBB disruption and predicts drug delivery in a target volume, necessary for clinical translation of FUS for increased drug delivery to the brain.

Studies in mice using DCE MRI demonstrated that  $K_{trans}$  in the sonicated hemisphere of the brain was found to be least an order of magnitude higher than that in the contralateral hemisphere, within a range of ultrasound exposure parameters that induced minimal or no vascular damage (101,119,120). The study by Park et al also demonstrated that  $K_{trans}$  at 30 minutes post FUS showed a linear correlation with doxorubicin delivery to the sonicated regions (101).

For quantitative DCE techniques, CT has advantages over MRI mainly because of the higher temporal resolution while maintaining sub millimeter resolution and superior quantitative accuracy (121). DCE-CT methods have been used to quantify PS in tumor models (122), high-grade glioma (123), and in stroke patients (124).

CT Perfusion, similar to DCE-MRI, is based on imaging methods that characterize tissue hemodynamics by modeling the transport of contrast through the vascular bed into the tissue through a permeable endothelium, e.g. a disrupted BBB from FUSwMB. In DCE-MRI, the contrast from gadolinium-based agents is generated via interactions with nearby water molecules, whereas in CT Perfusion, the contrast from iodinated agents comes from the attenuation of x-rays, measured in Hounsfield units. The typical CT Perfusion protocol involves two serial phases: 1) continuous acquisition phase where images are

acquired rapidly ( $\sim 1$ s per image), and should last long enough to capture the initial wash-in and wash-out of the bolus ( $\sim 30$ - $40$ s), and 2) delay phase where images are acquired less frequently (every 10-15s) to observe the slow exchange of contrast between the blood and tissue through the permeable endothelium. The quantitative evaluation of transport parameters from a CT Perfusion study is based on the theoretical concept of the impulse residue function  $R(t)$ , which describes the concentration-time curve in the ROI,  $C_e(t)$ , when any unit amount of contrast is instantaneously introduced into the arterial input of a tissue region.

Empirically,  $R(t)$  is the fraction of contrast that remains within the tissue as a function of time following an instantaneous contrast injection in the arterial input. Given that the measured signal intensity varies linearly with contrast concentration, and assuming that the blood flow ( $F$ ) and PS are constant within the period of measurement, the tissue time-concentration curve  $C_e(t)$  can be obtained from the convolution between the arterial input function,  $C_a(t)$ , and the model dependent impulse residue function,  $R(t)$  (125). This relationship can be mathematically expressed as:

$$C_e(t) = F \cdot C_a(t) \otimes R(t) \quad \dots \text{Equation 1-3}$$

where  $\otimes$  is a convolution operator.

### 1.9.2 General Closed Two-Compartmental Model

The general closed two-compartmental model, which defines the intravascular space and the extravascular interstitial space as well-mixed compartments, is commonly used to evaluate  $K_{\text{trans}}$  (126). Unlike open compartmental models, in which the contrast is ‘explicitly’ allowed to be cleared from the system, closed compartmental models do not consider any vascular or extravascular clearance. Since contrast agents are usually inert (i.e. not metabolized) in tissue, tracer kinetic modeling of the contrast agent distribution can be achieved with only two compartments. By using a compartment to model intravascular space (vessels), it is implicitly assumed that the transit time through the

vessels is ignored. A schematic of the closed two-compartment model is shown in Figure 1-8.

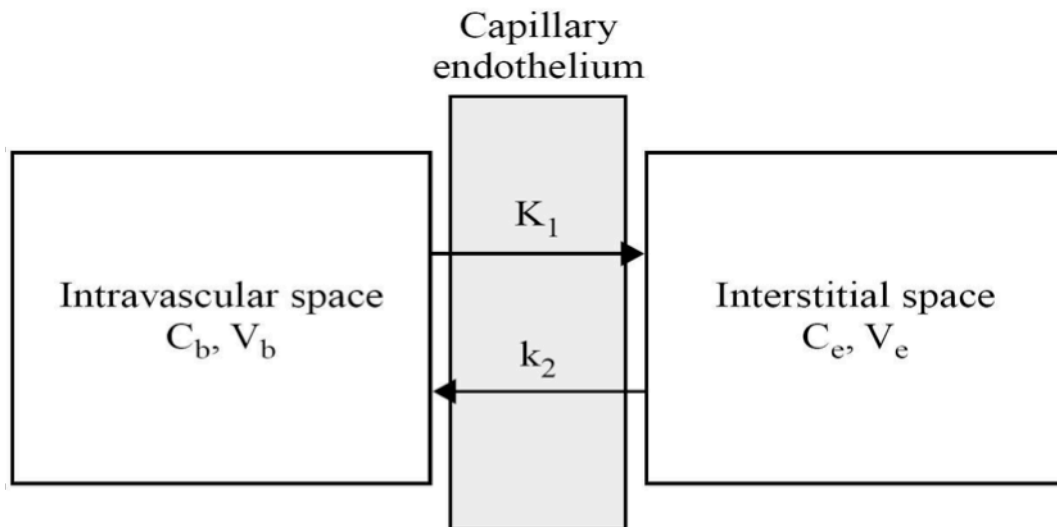


**Figure 1-8: A schematic of the general closed two-compartment model that distributes contrast between the intravascular space and the interstitial space, as two separate ‘well-mixed’ compartments. Adapted from Lee et al. 2003 (127).**

To model the distribution in the interstitial space, the following equation can be written by applying the Fick Principle (conservation of mass):

$$V_e \frac{dC_e(t)}{dt} = K_{trans} \cdot C_b(t) - K_{trans} C_e(t) \quad \dots \text{Equation 1-4}$$

where  $C_b(t)$ ,  $C_a(t)$ , and  $C_e(t)$ , are the blood, arterial, and interstitial concentration of contrast agent solute, respectively;  $V_e$  is the distribution volume of contrast agent in the interstitial space;  $K_1$  or  $K_{trans}$  is the forward volume transfer constant from the intravascular space into the interstitial space and is equal to the backward volume transfer constant because of the assumption that passive diffusion is the exchange mechanism between the two spaces (see Section 1.9.3). The solution for Equation 1-4 leads to an expression for the interstitial concentration of contrast agent:

$$C_e(t) = \frac{K_{trans}}{V_e} \cdot \int_0^t C_a(u) e^{-\frac{K_{trans}}{V_e}(t-u)} du \quad \dots \text{Equation 1-5}$$

and  $k_2 = \frac{K_{trans}}{V_e}$  is the backflux rate constant from interstitial space to intravascular space

Since a CT scanner measures tissue enhancement that has contribution from both the intravascular and interstitial space, thus:

$$Q(t) = V_e \cdot C_e(t) + V_b \cdot C_a(t) = K_{trans} \cdot \int_0^t C_a(u) e^{-\frac{K_{trans}}{V_e}(t-u)} du + V_b \cdot C_a(t) \quad \dots \text{Equation 1-6}$$

where  $Q(t)$  is the mass of contrast agent in a unit mass of tissue.

Equation 1-6 becomes the operating equation for the estimation of the functional parameters:  $K_{trans}$ ,  $V_e$  and  $V_b$ , which can be achieved using a variety of nonlinear regression methods (128). Equation 1-6 can be simplified by invoking the assumption that there is no backflux of contrast agent from the interstitial to intravascular space (129):

$$\frac{Q(t)}{C_a(t)} = K_{trans} \cdot \frac{\int_0^t C_a(u) du}{C_a(t)} + V_b \quad \dots \text{Equation 1-7}$$

Equation 1-7 is better known as the Patlak plot (130): if  $\frac{Q(t)}{C_a(t)}$  is plotted vs  $\frac{\int_0^t C_a(u) du}{C_a(t)}$ ,

the result is a straight line with a slope of  $K_{trans}$  and an intercept of  $V_b$ . Although useful for quantifying the rate of delivery across the BBB as  $K_{trans}$ , it is doubtful whether the no backflux assumption is valid in tumor imaging. In the next section, we show that  $K_{trans}$  is equal to the blood flow (F) and extraction efficiency (E) product: FE. The mass of solute delivered to the tissue and can diffuse into the interstitial space is  $F \cdot (C_a(t) - C_v(t))$ .  $E$  is defined as :

$$E = \frac{C_a - C_v}{C_a - C_e} \approx 1 - e^{-\frac{PS}{F}} \quad \dots \text{Equation 1-8}$$

or the fraction of this mass that is actually transferred from the vascular to interstitial space, during a single passage of blood from the arterial end to the venous end of the capillaries of a tissue (131).

A drawback of compartmental models is that  $F$  and  $E$  (PS) cannot be measured separately because they are determined together as  $K_{\text{trans}}$ . This is expected because by assuming the intravascular space as a well-mixed compartment all information related to the convective transport of solute along the capillaries is lost.

### 1.9.3 Johnson and Wilson Model

As opposed to compartment model with spatially uniform contrast concentration, the intravascular space of the Johnson and Wilson model has a concentration gradient from the arterial to the venous end of capillaries from the diffusion of contrast across the capillary endothelium into the interstitial space as blood travels down the length of capillaries. The Johnson and Wilson (JW) model (132) is one that models both the convective transport of contrast in blood vessels and the diffusion of contrast between vessels and interstitial space. In brief, the model lumps all the capillaries together into a single cylinder of length  $L$  and volume  $V_b$ , with a permeability surface area product  $PS$ , while the interstitial space is assumed to be a cylindrical annulus around the capillary, which behaves like a well-mixed compartment. As a result, it allows for the separate estimation of  $F$  and  $E$  (PS), which is not possible with a compartmental model.

In this section, the JW model is used to justify the expression, Equation 1-8, for the extraction efficiency ( $E$ ). The impulse residue function,  $R(t)$  of the model, which forms the basis of kinetic analysis of the subsequent chapters, will be introduced in the next section.

As the blood borne contrast enters the capillary, it starts to diffuse across the capillary endothelium into the interstitial space, thus the blood concentration of contrast,  $C_b$  will be a function of both axial position,  $x$ , along the capillary as well as time,  $t$ . The interstitial concentration of solute is  $C_e(t)$  and depends only on time, because the interstitial space is

treated as an ‘evenly-mixed’ compartment. A schematic of the Johnson and Wilson distributed parameter model is shown in Figure 1-9.

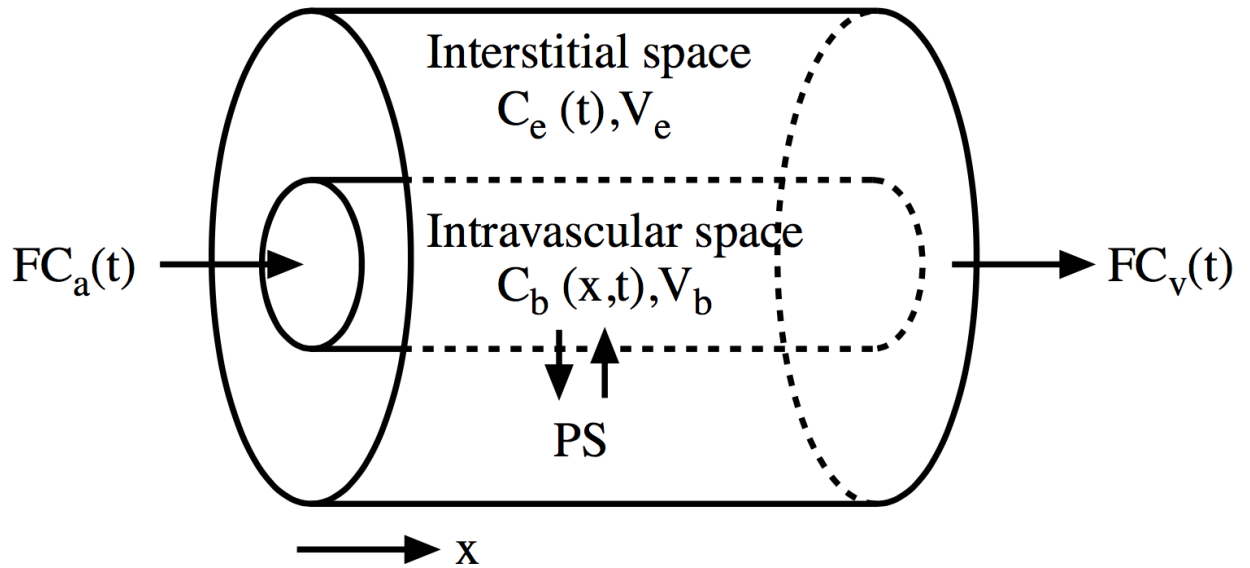


**Figure 1-9: A schematic of the Johnson and Wilson distributed parameter model.**

**Adapted from Lee et al. 2003 (127).**

The transport and exchange of solute through the capillaries can be described by the following equation:

$$\frac{\partial C_b(x,t)}{\partial t} + \frac{FL}{V_b} \frac{\partial C_b(x,t)}{\partial x} + \frac{PS}{V_b} [C_b(x,t) - C_e(t)] = 0 \quad \dots \text{Equation 1-9}$$

For the case when  $C_e(t)$  is a constant, say  $C_e$ , Equation 1-9 has the solution:

$$C_b(x,t) = C_a \left( t - \frac{V_b}{FL} x \right) e^{-\frac{PS}{FL} x} + C_e - C_e e^{-\frac{PS}{FL} x} H \left( t - \frac{V_b}{FL} x \right) \quad \dots \text{Equation 1-10}$$

where  $H(t)$  is the unit step function. As expected, at  $x = 0$   $C_b(x,t) = C_a(t)$  and

$$C_v(t) = C_b(x,t) \Big|_{x=L, t \geq \frac{V_b}{F}} = C_a \left( t - \frac{V_b}{F} \right) e^{-\frac{PS}{F}} + C_e \left( 1 - e^{-\frac{PS}{F}} \right) \quad \dots \text{Equation 1-11}$$

Further the arterio-venous difference can be written as:

$$C_a(t - T_c) - C_v(t) = \left(1 - e^{-\frac{PS}{F}}\right) [C_a(t - T_c) - C_e] \quad \dots \text{Equation 1-12}$$

where  $T_c = \frac{V_b}{F}$  is the capillary transit time. Thus,

$$E \approx \frac{C_a(t - T_c) - C_v(t)}{C_a(t - T_c) - C_e} = 1 - e^{-\frac{PS}{F}} \quad \dots \text{Equation 1-13}$$

as Crone (131) and Renkin (133) have previously derived. Moreover, the Fick Law gives the change in the interstitial concentration as:

$$V_e \frac{dC_e(t)}{dt} = F \cdot [C_a(t - T_c) - C_v(t)] \quad \dots \text{Equation 1-14}$$

which, according to Equation 1-13 can also be expressed as

$$V_e \frac{dC_e(t)}{dt} = FE \cdot [C_a(t - T_c) - C_e] \quad \dots \text{Equation 1-15}$$

Equation 1-15 can be interpreted as that the forward flux rate from the capillary to the interstitial space is  $FE \cdot C_a(t - T_c)$  and the back-flux rate from the interstitial space to the capillary is  $FE \cdot C_e$ . Thus,  $FE$  is the unidirectional flux rate of solute per unit concentration, or volume transfer constant, from blood to interstitial space or from interstitial space to blood. The above derivation is obtained under the special case when  $C_e(t)$  is held constant in time. For the general case when  $C_e(t)$  is an arbitrary function of time, St. Lawrence and Lee has shown that the unidirectional flux of solute per unit concentration is still  $FE$  (134).

### 1.9.4 Adiabatic approximation leading to the Johnson-Wilson-Lee Model

Distributed parameter model has an advantage over closed two-compartmental model in kinetic analysis of DCE MRI or CT studies because it allows blood flow (F) and permeability surface product (PS) or extraction efficiency (E) to be estimated separately which is not possible with compartmental models. Distributed parameter models allow for the separation by introducing a concentration gradient from the arterial to the venous end of the capillary (127). This gradient models the leakage of contrast through permeable endothelium into the tissue as blood traverses the length of the vessels.

The governing equations of the Johnson and Wilson model can be written as:

$$\frac{\partial C_b(x, t)}{\partial t} + \frac{FL}{V_b} \frac{\partial C_b(x, t)}{\partial x} + \frac{PS}{V_b} [C_b(x, t) - C_e(t)] = 0 \quad \dots \text{Equation 1-9}$$

$$V_e \frac{dC_e(t)}{dt} = \frac{PS}{L} \int_0^L [C_b(x, t) - C_e(t)] dx \quad \dots \text{Equation 1-16}$$

Equation 1-9 describes the convective and diffusional transport of solute in capillaries, while Equation 1-16 gives the rate of change of solute concentration in the interstitial compartment. The solution (impulse residue function) of the Johnson and Wilson model can only be expressed in the frequency domain with use of Laplace transform (132), which had severely limited its application in the kinetic analysis of DCE MRI or CT studies. This was until St Lawrence and Lee discovered an adiabatic approximation to derive an analytical solution of the model in the time domain (134).

There are two main motivations for using the adiabatic approximation. First, it can be assumed that the time rate of change of  $C_e(t)$  is much slower than that of  $C_b(x, t)$ , such that  $C_e(t)$  can be approximated by a staircase function consisting of discrete, finite steps provided the time interval of each step is small relative to the transit time of the capillaries. With this approximation  $C_e(t)$  is constant within each step of the staircase. Second, as discussed above in the solution of Equation 1-9, when  $C_e(t)$  is a constant,

$C_b(x,t)$  can be expressed in terms of  $C_e(t)$ . Thus, at each step of the staircase approximation of  $C_e(t)$ , Equation 1-9 is solved for  $C_b(x,t)$  in terms of  $C_e(t)$ . With  $C_b(x,t)$  expressed in  $C_e(t)$ , Equation 1-16 can be used to determine the increase in  $C_e(t)$  at the end of the step. This procedure can be repeated for each step in the staircase approximation of  $C_e(t)$  resulting in a time domain solution for the mass of solute per unit mass of tissue,  $Q(t)$ , which can be expressed as:

$$Q(t) = F \cdot C_a(t) \otimes R(t) \quad \dots \text{Equation 1-17}$$

where  $\otimes$  is a convolution operator and  $R(t)$  is expressed as:

$$R(t) = \begin{cases} 1 & 0 < t \leq \frac{V_b}{F} \\ Ee^{-\frac{FE}{V_c}(t - \frac{V_b}{F})} H(t - \frac{V_b}{F}) & t > \frac{V_b}{F} \end{cases} \quad \dots \text{Equation 1-18}$$

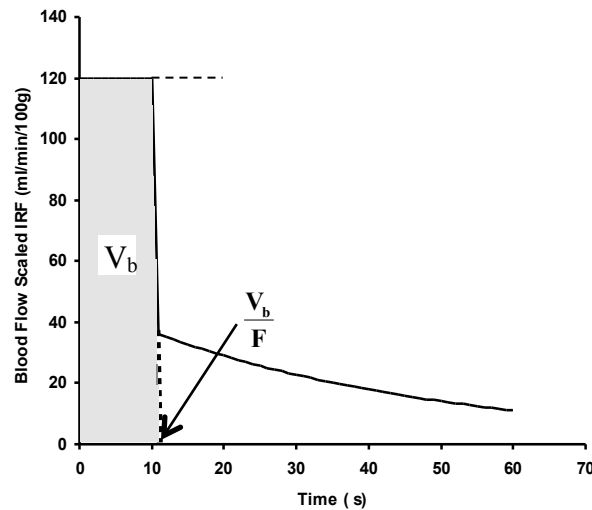


**Figure 1-10: The blood flow scaled impulse residue function according to the Johnson and Wilson model. The symbols are defined in the text. Adapted from Lee et al 2003 (127) .**

Figure 1-10 is a plot of  $F \cdot R(t)$  or the blood flow scaled impulse residue function. It lends itself to the following interpretation: if a bolus of contrast agent is injected directly into the arterial inlet of the tissue, so that  $C_a(t)$  is non-zero for a very short while and the area under  $C_a(t)$  is unity, the total mass of solute delivered to the tissue is numerically equal to  $F$ . The blood flow scaled impulse residue function,  $F \cdot R(t)$ , therefore would reach a height of  $F$  immediately and maintains this height for a duration equal to the mean transit time (MTT) of the tissue,  $V_b/F$ . The area under the curve for when the bolus is traversing the length of the capillary is the blood volume,  $V_b$ , and is represented as the shaded area in Figure 1-10. After a time equal to  $V_b/F$ , unextracted contrast agent starts to leave the tissue,  $F \cdot R(t)$  drops to a height of  $FE$  and thereafter contrast agent in the interstitial space back diffuses into the intravascular space and is washed out by blood flow. This portion of  $F \cdot R(t)$  is described by a decreasing monoexponential function with a rate constant equal to  $FE/V_e$ . With  $C_a(t)$  and  $Q(t)$  measured by CT scanning,  $F \cdot R(t)$  can be determined by model deconvolution (135) according to Equation 1-18 to yield the parameters:  $F$ ,  $V_b$ , MTT and  $E$  (PS).

### 1.9.5 In-vivo Diffusion and Flow Limited Solute Exchange

In the context of drug delivery, the volume transfer constant  $K_{trans}$  ( $FE$ ), which is estimated by the JW model, is more important for drug delivery than PS alone. When predicting PS, there exists three regimes for the diffusive exchange of solute between blood and interstitial space: 1) when  $PS \ll F$ ,  $FE$  approximates PS, the exchange is diffusion-limited; 2) when PS is of the same magnitude as  $F$ , the exchange is neither diffusion nor flow limited; and 3) when  $PS \gg F$ , so that  $FE$  approaches  $F$ , the exchange is flow-limited.

In the diffusion-limited scenario, as is with disrupted BBB, we can approximate  $FE$  with PS, meaning the slope of the Patlak analysis in Equation 1-7 can be used to estimate PS. In brain tumors, where the BTB PS is significantly elevated (136),  $PS \ll F$  is no longer true, therefore  $FE$  is not the same as PS, and  $FE$  is the correct functional parameter to predict drug delivery.

PS measures the diffusional flux between two semi permeable compartments at different concentration of the contrast agent (blood borne solutes) where the content of the compartments is not moving. In the in-vivo situation, whereas interstitial fluid is not moving, blood in the capillaries is moving from arterioles to venules while blood borne solutes are exchanging by diffusion with the interstitial fluid. When endothelial permeability is increased, whether it's from the gaps between tight junction proteins that are opened up following FUSwMB (75), or in brain tumors, where progression is accompanied by breakdown in the BTB (136), the transfer of solutes across the endothelium is no longer governed by diffusion alone, but also by pressure driven fluid flow across such gaps, as governed by Starling's Law:

$$J_c = L_t S_v (1 - \sigma_s) (\Delta p_t - \sigma \Delta \Pi) \quad \dots \text{Equation 1-19}$$

where  $J_c$  is the convective flux of solute across the disrupted BBB or BTB,  $L_t$  is the hydraulic conductivity,  $S_v$  is the vascular surface area,  $\Delta p$  is the transmural hydrostatic pressure gradient,  $\Delta \Pi$  is the transmural osmotic pressure gradient pressure gradient,  $\sigma$  is the osmotic reflection coefficient, and  $\sigma_s$  is the solute's reflection coefficient.

Starling's law, which forms the basis of Equation 1-19, states that the fluid flow across the wall of a capillary is dependent on the balance between the hydrostatic pressure gradient and the oncotic pressure gradient across the capillary. In the microvasculature, diffusion-driven solute fluxes are short lived and will proceed until the concentration of proteins are sufficient to oppose osmotic force of solute diffusion (until  $\sigma \Delta \Pi = 0$ ), and occurs independent of changes in the net filtration pressure. By plotting the cumulative solute flux,  $J_t/S$ , against the change in interstitial oncotic pressure ( $\sigma \Delta \Pi$ ), the Peclet number, which is the ratio of the contributions to solute transport by convection to those by diffusion, can be calculated to identify the extent of solvent drag present (i.e. the contribution from convective solute flux) (137,138). When there is sufficient solvent drag, solute transfer from capillary to interstitial fluid is neither diffusion nor flow limited and may no longer be dependent only on PS. However, by interpreting  $K_{trans}$  (FE) as having contribution from both convective and diffusive flux across the endothelial

barrier, as opposed to diffusion alone, the Johnson-Wilson-Lee (JWL) model could be extended to include both solute transfer processes.

## 1.10 Research Goals and Objectives

The work presented in this thesis focused on two major goals: 1) Using CT Perfusion to measure the PS following FUSwMB, in rats with an intact BBB, and 2) Evaluating the BTB PS response following FUSwMB in a C6 rat glioma model. These goals were accomplished by achieving the following objectives:

1. Titrate FUS exposure parameters to induce a quantifiable and transient BBB disruption as demonstrated by an increase in PS, with minimal tissue damage.
2. Evaluate the acute BTB response following FUSwMB at the exposure parameters found in objective 1.
3. Evaluate the 24-h, and 72-h BTB PS response following FUSwMB using small and large CT contrast agents.
4. Measure edema volume with MRI and CT Perfusion derived vascular distribution volume,  $V_e$ , following FUSwMB.
5. Perform histological and immunohistological analysis to identify the anatomical correlates involved in BTB response following FUSwMB.

## 1.11 Thesis Outline

### 1.11.1 FUS sonication with MB administration Induced BBB Disruption: Quantifying the Increased Endothelial Permeability using CT Perfusion (Chapter 2)

For clinical translation of FUSwMB, as a novel technique to improve drug delivery across the BBB, it is important to evaluate the safety and efficacy of a range of possible parameters, and demonstrate that CT Perfusion can quantify the increase in BBB PS to monitor and predict drug delivery. The purpose of this study was to evaluate CT Perfusion as a tool for quantifying BBB PS following disruption following FUSwMB.

### 1.11.2 Using small (750 Da), and large (65 kDa) contrast agent in CT Perfusion to quantify BTB PS response following FUS

## sonication with MB administration in a C6 rat glioma model (Chapter 3)

Small molecules such as temozolamide, and large molecules such as bevacizumab, are routinely used, often in combination, to treat glioma. Small and large molecules have different contributions of diffusive and convective transport across the BTB, as the governing mechanism of transport. To understand the BTB PS response for small and large drugs, we used CT contrast agents of different sizes, Isovue (760 Da) and eXia (65 kDa) to evaluate BTB PS following FUSwMB.

### 1.11.3 Investigating the decrease in edema following FUS sonication with MB administration using MRI and vascular distribution volume, measured from DCE-CT (Chapter 4).

A decrease in BTB PS following FUSwMB, measured with a diffusible small molecule contrast, should decrease the associated vasogenic edema, resulting in a decrease in the abnormally elevated IFP. This decrease in IFP should also partially restore the transvascular pressure required for the convective transfer of large molecules across the BTB. The purpose of this study was to investigate the change in vasogenic edema following FUSwMB, using qualitative and quantitative MRI, and CT Perfusion derived contrast distribution volume, as well as to investigate the mechanisms behind the resulting BTB response with histopathology.

### 1.11.4 Conclusion and Future Work (Chapter 5)

In the final chapter, the major findings of this thesis are summarized, and their experimental and clinical relevance are discussed. The potential of FUSwMB for increased drug delivery in brain tumors is proposed, and some future experimental directions are presented.

## 1.12 References

1. Pardridge WM. Molecular biology of the blood-brain barrier. *Mol Biotechnol.* 2005;30(1):57–70.

2. Persidsky Y, Ramirez SH, Haorah J, Kanmogne GD. Blood-brain barrier: Structural components and function under physiologic and pathologic conditions. In: *Journal of Neuroimmune Pharmacology*. 2006. p. 223–36.
3. Wolburg H, Lippoldt A. Tight junctions of the blood-brain barrier: Development, composition and regulation. *Vascular Pharmacology*. 2002. p. 323–37.
4. Kniesel U, Wolburg H. Tight junctions of the blood-brain barrier. *Cell Mol Neurobiol*. 2000;20(1):57–76.
5. Armulik A, Genové G, Mäe M, Nisancioglu MH, Wallgard E, Niaudet C, et al. Pericytes regulate the blood-brain barrier. *Nature*. 2010;468(7323):557–61.
6. Abbott NJ, Rönnbäck L, Hansson E. Astrocyte-endothelial interactions at the blood-brain barrier. *Nat Rev Neurosci*. 2006;7(1):41–53.
7. Abbott NJ. Astrocyte-endothelial interactions and blood-brain barrier permeability. *Journal of Anatomy*. 2002. p. 629–38.
8. Hawkins BT, Davis TP. The Blood-Brain Barrier / Neurovascular Unit in Health and Disease. *Pharmacol Rev*. 2005;57(2):173–85.
9. Abbott NJ, Patabendige A a K, Dolman DEM, Yusof SR, Begley DJ. Structure and function of the blood-brain barrier. *Neurobiol Dis* [Internet]. Elsevier Inc.; 2010;37(1):13–25.
10. Abbott NJ, Patabendige AAK, Dolman DEM, Yusof SR, Begley DJ. Structure and function of the blood-brain barrier. *Neurobiology of Disease*. 2010. p. 13–25.
11. Pardridge WM. The blood-brain barrier: bottleneck in brain drug development. *NeuroRx*. 2005;2(1):3–14.
12. Lipinski CA. Drug-like properties and the causes of poor solubility and poor permeability. *J Pharmacol Toxicol Methods*. 2000;44(1):235–49.

13. Tsuji A, Tamai I. Carrier-mediated or specialized transport of drugs across the blood-brain barrier. *Advanced Drug Delivery Reviews*. 1999. p. 277–90.
14. Pardridge WM. Drug and gene targeting to the brain via blood-brain barrier receptor-mediated transport systems. *Int Congr Ser*. 2005;1277:49–62.
15. Pardridge WM. Blood-brain barrier delivery of protein and non-viral gene therapeutics with molecular Trojan horses. *J Control Release*. 2007;122(3):345–8.
16. Pardridge WM. Targeting neurotherapeutic agents through the blood-brain barrier. *Arch Neurol*. 2002;59(1):35–40.
17. Kroll RA, Neuwelt EA. Outwitting the blood-brain barrier for therapeutic purposes: Osmotic opening and other means. *Neurosurgery*. 1998. p. 1083–100.
18. Matsukado K, Sugita M, Black KL. Intracarotid low dose bradykinin infusion selectively increases tumor permeability through activation of bradykinin B2 receptors in malignant gliomas. *Brain Res*. 1998;792(1):10–5.
19. Broadwell RD, Salcman M, Kaplan RS. Morphologic effect of dimethyl sulfoxide on the blood-brain barrier. *Science*. 1982;217(4555):164–6.
20. Gennuso R, Spigelman MK, Chinol M, Zappulla RA, Nieves J, Vallabhajosula S, et al. Effect of blood-brain barrier and blood-tumor barrier modification on central nervous system liposomal uptake. *Cancer Invest*. 1993;11(2):118–28.
21. Rabchevsky AG, Degos JD, Dreyfus PA. Peripheral injections of Freund's adjuvant in mice provoke leakage of serum proteins through the blood-brain barrier without inducing reactive gliosis. *Brain Res*. 1999;832(1-2):84–96.
22. Bolton SJ, Anthony DC, Perry VH. Loss of the tight junction proteins occludin and zonula occludens-1 from cerebral vascular endothelium during neutrophil-induced blood-brain barrier breakdown in vivo. *Neuroscience*. 1998;86(4):1245–57.

23. Vykhodtseva N, McDannold N, Hynynen K. Progress and problems in the application of focused ultrasound for blood-brain barrier disruption. *Ultrasonics*. 2008;48(4):279–96.
24. Dietz GPH, Bähr M. Delivery of bioactive molecules into the cell: The Trojan horse approach. *Molecular and Cellular Neuroscience*. 2004. p. 85–131.
25. Krewson CE, Klarman ML, Saltzman WM. Distribution of nerve growth factor following direct delivery to brain interstitium. *Brain Res*. 1995;680(1-2):196–206.
26. Yan Q, Matheson C, Sun J, Radeke MJ, Feinstein SC, Miller JA. Distribution of intracerebral ventricularly administered neurotrophins in rat brain and its correlation with trk receptor expression. *Exp Neurol*. 1994;127(1):23–36.
27. Ai Y, Markesbery W, Zhang Z, Grondin R, Elseberry D, Gerhardt GA, et al. Intraputamenal infusion of GDNF in aged rhesus monkeys: Distribution and dopaminergic effects. *J Comp Neurol*. 2003;461(2):250–61.
28. Siegel R, Ma J, Zou Z, Jemal A. Cancer statistics, 2014. *CA Cancer J Clin* [Internet]. 2014;64(1):9–29.
29. Dolecek TA, Propp JM, Stroup NE, Kruchko C. CBTRUS statistical report: Primary brain and central nervous system tumors diagnosed in the United States in 2005-2009. *Neuro-Oncology*. 2012.
30. Burger PC, Vogel FS, Green SB, Strike TA. Glioblastoma Multiforme and Anaplastic Astrocytoma. *Cancer* [Internet]. 1985;56:1106–11.
31. Behin A, Hoang-Xuan K, Carpentier AF, Delattre J-Y. Primary brain tumours in adults. *Lancet*. 2003;361(9354):323–31.
32. Grossman S a., Batarra JF. Current management of glioblastoma multiforme. *Semin Oncol* [Internet]. 2004;31(5):635–44.

33. Liu HL, Fan CH, Ting CY, Yeh CK. Combining microbubbles and ultrasound for drug delivery to brain tumors: Current progress and overview. *Theranostics*. 2014;4(4):432–44.
34. Stupp R, Hegi ME, Mason WP, van den Bent MJ, Taphoorn MJ, Janzer RC, et al. Effects of radiotherapy with concomitant and adjuvant temozolomide versus radiotherapy alone on survival in glioblastoma in a randomised phase III study: 5-year analysis of the EORTC-NCIC trial. *Lancet Oncol* [Internet]. 2009;10(5):459–66.
35. Kreisl TN, Kim L, Moore K, Duic P, Royce C, Stroud I, et al. Phase II trial of single-agent bevacizumab followed by bevacizumab plus irinotecan at tumor progression in recurrent glioblastoma. *J Clin Oncol* [Internet]. 2009;27(5):740–5.
36. Friedman HS, Prados MD, Wen PY, Mikkelsen T, Schiff D, Abrey LE, et al. Bevacizumab alone and in combination with irinotecan in recurrent glioblastoma. *J Clin Oncol*. 2009;27(28):4733–40.
37. Chinot OL, Wick W, Mason W, Henriksson R, Saran F, Nishikawa R, et al. Bevacizumab plus radiotherapy-temozolomide for newly diagnosed glioblastoma. *N Engl J Med* [Internet]. 2014;370(8):709–22.
38. Gilbert MR, Dignam JJ, Armstrong TS, Wefel JS, Blumenthal DT, Vogelbaum M a, et al. A randomized trial of bevacizumab for newly diagnosed glioblastoma. *N Engl J Med* [Internet]. 2014;370(8):699–708.
39. Grossman S, Wharam M, Sheidler V, Kleinberg L, Zeltzman M, Yue N, et al. Phase II study of continuous infusion carmustine and cisplatin followed by cranial irradiation in adults with newly diagnosed high-grade astrocytoma. *J Clin Oncol*. 1997;15(7).
40. Fidler IJ, Yano S, Zhang RD, Fujimaki T, Bucana CD. The seed and soil hypothesis: Vascularisation and brain metastases. *Lancet Oncol*. 2002;3(1):53–7.

41. Hobbs SK, Monsky WL, Yuan F, Roberts WG, Griffith L, Torchilin VP, et al. Regulation of transport pathways in tumor vessels: role of tumor type and microenvironment. *Proc Natl Acad Sci U S A*. 1998;95(8):4607–12.
42. Nagy JA, Benjamin L, Zeng H, Dvorak AM, Dvorak HF. Vascular permeability, vascular hyperpermeability and angiogenesis. *Angiogenesis*. 2008. p. 109–19.
43. Plate KH, Mennel HD. Vascular morphology and angiogenesis in glial tumors. *Exp Toxicol Pathol*. 1995;47(2-3):89–94.
44. Rampling R, Cruickshank G, Lewis AD, Fitzsimmons SA, Workman P. Direct measurement of pO<sub>2</sub> distribution and bioreductive enzymes in human malignant brain tumors. *Int J Radiat Oncol Biol Phys*. 1994;29(3):427–31.
45. Valk PE, Mathis CA, Prados MD, Gilbert JC, Budinger TF. Hypoxia in human gliomas: demonstration by PET with fluorine-18-fluoromisonidazole. *J Nucl Med*. 1992;33(12):2133–7.
46. Samoto K, Ikezaki K, Ono M, Shono T, Kohno K, Kuwano M, et al. Expression of vascular endothelial growth factor and its possible relation with neovascularization in human brain tumors. *Cancer Res*. 1995;55(0008-5472 (Print)):1189–93.
47. Neufeld G, Cohen T, Gengrinovitch S, Poltorak Z. Vascular endothelial growth factor (VEGF) and its receptors. *FASEB J [Internet]*. 1999;13(1):9–22.
48. Carmeliet P, Jain RK. Angiogenesis in cancer and other diseases. *Nature*. 2000;407(6801):249–57.
49. Dvorak HF. Vascular permeability factor/vascular endothelial growth factor: A critical cytokine in tumor angiogenesis and a potential target for diagnosis and therapy. *Journal of Clinical Oncology*. 2002. p. 4368–80.
50. Jain RK, di Tomaso E, Duda DG, Loeffler JS, Sorensen a G, Batchelor TT. Angiogenesis in brain tumours. *Nat Rev Neurosci [Internet]*. 2007;8(8):610–22.

51. Yuan F, Salehi HA, Boucher Y, Vasthare US, Tuma RF, Jain RK. Vascular permeability and microcirculation of gliomas and mammary carcinomas transplanted in rat and mouse cranial windows. *Cancer Res.* 1994;54(17):4564–8.
52. Monsky WL, Fukumura D, Gohongi T, Ancukiewicz M, Weich HA, Torchilin VP, et al. Augmentation of transvascular transport of macromolecules and nanoparticles in tumors using vascular endothelial growth factor. *Cancer Res.* 1999;59(16):4129–35.
53. Monsky WL, Carreira CM, Tsuzuki Y, Gohongi T, Fukumura D, Jain RK. Role of host microenvironment in angiogenesis and microvascular functions in human breast cancer xenografts: Mammary fat pad versus cranial tumors. *Clin Cancer Res.* 2002;8(4):1008–13.
54. Jain RK, Tong RT, Munn LL. Effect of vascular normalization by antiangiogenic therapy on interstitial hypertension, peritumor edema, and lymphatic metastasis: Insights from a mathematical model. *Cancer Res.* 2007;67(6):2729–35.
55. Griffon-Etienne G, Boucher Y, Brekken C, Suit HD, Jain RK. Taxane-induced apoptosis decompresses blood vessels and lowers interstitial fluid pressure in solid tumors: Clinical implications. *Cancer Res.* 1999;59(15):3776–82.
56. Helmlinger G, Netti PA, Lichtenbeld HC, Melder RJ, Jain RK. Solid stress inhibits the growth of multicellular tumor spheroids. *Nat Biotechnol.* 1997;15(8):778–83.
57. Leu AJ, Berk DA, Lymboussaki A, Alitalo K, Jain RK. Absence of functional lymphatics within a murine sarcoma: A molecular and functional evaluation. *Cancer Res.* 2000;60(16):4324–7.
58. Padera TP, Stoll BR, Tooredman JB, Capen D, di Tomaso E, Jain RK. Pathology: cancer cells compress intratumour vessels. *Nature.* 2004;427(6976):695.
59. Boucher Y, Jain RK. Microvascular pressure is the principal driving force for interstitial hypertension in solid tumors: Implications for vascular collapse. *Cancer Res.* 1992;52(18):5110–4.

60. Jain RK. Barriers to drug delivery in solid tumors. *Scientific American*, 271(1), 58-65. Retrieved from <http://www.ncbi.nlm.nih.gov/pubmed/8066425>tumors. *Sci Am* [Internet]. 1994;271(1):58–65. A
61. Netti PA, Baxter LT, Boucher Y, Skalak R, Jain RK. Time-dependent behavior of interstitial fluid pressure in solid tumors: Implications for drug delivery. *Cancer Res.* 1995;55(22):5451–8.
62. Chauhan VP, Lanning RM, Diop-Frimpong B, Mok W, Brown EB, Padera TP, et al. Multiscale measurements distinguish cellular and interstitial hindrances to diffusion in vivo. *Biophys J.* 2009;97(1):330–6.
63. McKee TD, Grandi P, Mok W, Alexandrakis G, Insin N, Zimmer JP, et al. Degradation of fibrillar collagen in a human melanoma xenograft improves the efficacy of an oncolytic herpes simplex virus vector. *Cancer Res.* 2006;66(5):2509–13.
64. Netti PA, Berk DA, Swartz MA, Grodzinsky AJ, Jain RK. Role of extracellular matrix assembly in interstitial transport in solid tumors. *Cancer Res.* 2000;60(9):2497–503.
65. Chauhan VP, Stylianopoulos T, Boucher Y, Jain RK. Delivery of Molecular and Nanoscale Medicine to Tumors: Transport Barriers and Strategies. *Annu Rev Chem Biomol Eng.* 2011;2(1):281–98.
66. Baxter LT, Jain RK. Transport of fluid and macromolecules in tumors. I. Role of interstitial pressure and convection. *Microvasc Res.* 1989;37(1):77–104.
67. Papadopoulos MC, Saadoun S, Binder DK, Manley GT, Krishna S, Verkman a. S. Molecular mechanisms of brain tumor edema. *Neuroscience.* 2004;129(4):1011–20.

68. Yang F-Y, Wang. Efficiency of drug delivery enhanced by acoustic pressure during blood brain barrier disruption induced by focused ultrasound. *Int J Nanomedicine*. 2012;2573.
69. Yang FY, Lin YS, Kang KH, Chao TK. Reversible blood-brain barrier disruption by repeated transcranial focused ultrasound allows enhanced extravasation. *J Control Release* [Internet]. Elsevier B.V.; 2011;150(1):111–6.
70. Hynynen K, McDannold N, Clement G, Jolesz F a, Zadicario E, Killiany R, et al. Pre-clinical testing of a phased array ultrasound system for MRI-guided noninvasive surgery of the brain--a primate study. *Eur J Radiol* [Internet]. 2006;59(2):149–56.
71. McDannold N, Vykhodtseva N, Hynynen K. Effects of acoustic parameters and ultrasound contrast agent dose on focused-ultrasound induced blood-brain barrier disruption. *Ultrasound Med Biol* [Internet]. 2008;34(6):930–7.
72. Chopra R, Vykhodtseva N, Hynynen K. Influence of exposure time and pressure amplitude on blood-brain-barrier opening using transcranial ultrasound exposures. *ACS Chem Neurosci*. 2010;1(5):391–8.
73. Kinoshita M, McDannold N, Jolesz F a., Hynynen K. Targeted delivery of antibodies through the blood-brain barrier by MRI-guided focused ultrasound. *Biochem Biophys Res Commun*. 2006;340(4):1085–90.
74. McDannold N, Vykhodtseva N, Raymond S, Jolesz F a., Hynynen K. MRI-guided targeted blood-brain barrier disruption with focused ultrasound: Histological findings in rabbits. *Ultrasound Med Biol*. 2005;31(11):1527–37.
75. Sheikov N, McDannold N, Sharma S, Hynynen K. Effect of Focused Ultrasound Applied With an Ultrasound Contrast Agent on the Tight Junctional Integrity of the Brain Microvascular Endothelium. *Ultrasound Med Biol*. 2008;34(7):1093–104.

76. Vykhodtseva N, McDannold N, Hynynen K. Progress and problems in the application of focused ultrasound for blood-brain barrier disruption. *Ultrasonics*. 2008. p. 279–96.
77. Tung Y-S, Vlachos F, Feshitan J a., Borden M a., Konofagou EE. The mechanism of interaction between focused ultrasound and microbubbles in blood-brain barrier opening in mice. *J Acoust Soc Am*. 2011;130(5):3059.
78. Rooney J, Nyborg W. Acoustic Radiation Pressure in a Traveling Plane Wave. *Am J Phys [Internet]*. 1972;40(12):1825–30.
79. Nyborg WL. Biological effects of ultrasound: Development of safety guidelines. Part II: General review. *Ultrasound Med Biol [Internet]*. 2001;27(3):301–33.
80. Miller DL. A review of the ultrasonic bioeffects of microsonation, gas-body activation, and related cavitation-like phenomena. *Ultrasound Med Biol [Internet]*. 1987;13(8):443–70.
81. Leighton TG. *The Acoustic Bubble*. The Journal of the Acoustical Society of America. 1994. 2616 p.
82. Gelet A, Chapelon JY, Poissonnier L, Bouvier R, Rouvière O, Curiel L, et al. Local recurrence of prostate cancer after external beam radiotherapy: early experience of salvage therapy using high-intensity focused ultrasonography. *Urology [Internet]*. 2004;63(4):625–9.
83. Chapelon JY, Ribault M, Vernier F, Souchon R, Gelet A. Treatment of localised prostate cancer with transrectal high intensity focused ultrasound. *Eur J Ultrasound [Internet]*. 1999;9(1):31–8.
84. Wu F, Wang ZB, Chen WZ, Zou JZ, Bai J, Zhu H, et al. Advanced hepatocellular carcinoma: treatment with high-intensity focused ultrasound ablation combined with transcatheter arterial embolization. *Radiology*. 2005;235(2):659–67.

85. Chen H, Hwang J. Ultrasound-targeted microbubble destruction for chemotherapeutic drug delivery to solid tumors. *J Ther Ultrasound* [Internet]. 2013;1(1):10.
86. Vaezy S, Martin RW, Schmiedl U, Caps M, Taylor S, Beach K, et al. Liver hemostasis using high-intensity focused ultrasound. *Ultrasound Med Biol*. 1997;23(9):1413–20.
87. Hwang JH, Vaezy S, Martin RW, Cho MY, Noble ML, Crum LA, et al. High-intensity focused US: a potential new treatment for GI bleeding. *Gastrointest Endosc* [Internet]. 2003;58(1):111–5.
88. Noble ML, Vaezy S, Keshavarzi A, Paun M, Prokop AF, Chi EY, et al. Spleen hemostasis using high-intensity ultrasound: survival and healing. *J Trauma* [Internet]. 2002;53(6):1115–20.
89. Hynynen K, Colucci V, Chung A, Jolesz F. Noninvasive arterial occlusion using MRI-guided focused ultrasound. *Ultrasound Med Biol* [Internet]. 1996;22(8):1071–7.
90. Rivens IH, Rowland IJ, Denbow M, Fisk NM, ter Haar GR, Leach MO. Vascular occlusion using focused ultrasound surgery for use in fetal medicine. *Eur J Ultrasound*. 1999;9(1):89–97.
91. O'Reilly M a, Huang Y, Hynynen K. The impact of standing wave effects on transcranial focused ultrasound disruption of the blood-brain barrier in a rat model. *Phys Med Biol*. 2010;55(18):5251–67.
92. Hynynen K, McDannold N, Vykhodtseva N, Raymond S, Weissleder R, Jolesz F a, et al. Focal disruption of the blood-brain barrier due to 260-kHz ultrasound bursts: a method for molecular imaging and targeted drug delivery. *J Neurosurg*. 2006;105(3):445–54.

93. Liu HL, Pan CH, Ting CY, Hsiao MJ. Opening of the Blood-Brain Barrier by Low-Frequency (28-kHz) Ultrasound: A Novel Pinhole-Assisted Mechanical Scanning Device. *Ultrasound Med Biol*. 2010;36(2):325–35.
94. Choi JJ, Wang S, Tung YS, Morrison B, Konofagou EE. Molecules of Various Pharmacologically-Relevant Sizes Can Cross the Ultrasound-Induced Blood-Brain Barrier Opening in vivo. *Ultrasound Med Biol*. 2010;36(1):58–67.
95. O'Reilly M a., Hynynen K. Blood-Brain Barrier: Real-time Feedback-controlled Focused Ultrasound Disruption by Using an Acoustic Emissions-based Controller. *Radiology*. 2012;263(1):96–106.
96. Vykhodtseva NI, Hynynen K, Damianou C. Histologic effects of high intensity pulsed ultrasound exposure with subharmonic emission in rabbit brain in vivo. *Ultrasound Med Biol*. 1995;21(7):969–79.
97. Hynynen K, McDannold N, Vykhodtseva N, Jolesz F a. Noninvasive MR imaging-guided focal opening of the blood-brain barrier in rabbits. *Radiology*. 2001;220(3):640–6.
98. Treat LH, McDannold N, Vykhodtseva N, Zhang Y, Tam K, Hynynen K. Targeted delivery of doxorubicin to the rat brain at therapeutic levels using MRI-guided focused ultrasound. *Int J Cancer*. 2007;121(4):901–7.
99. Choi JJ, Selert K, Gao Z, Samiotaki G, Baseri B, Konofagou EE. Noninvasive and localized blood-brain barrier disruption using focused ultrasound can be achieved at short pulse lengths and low pulse repetition frequencies. *J Cereb Blood Flow Metab* [Internet]. Nature Publishing Group; 2011;31(2):725–37.
100. Aryal M, Vykhodtseva N, Zhang YZ, Park J, McDannold N. Multiple treatments with liposomal doxorubicin and ultrasound-induced disruption of blood-tumor and blood-brain barriers improve outcomes in a rat glioma model. *J Control Release* [Internet]. Elsevier B.V.; 2013;169(1-2):103–11.

101. Park J, Zhang Y, Vykhodtseva N, Jolesz F a., McDannold NJ. The kinetics of blood brain barrier permeability and targeted doxorubicin delivery into brain induced by focused ultrasound. *J Control Release* [Internet]. Elsevier B.V.; 2012;162(1):134–42.
102. Yang FY, Wong TT, Teng MC, Liu RS, Lu M, Liang HF, et al. Focused ultrasound and interleukin-4 receptor-targeted liposomal doxorubicin for enhanced targeted drug delivery and antitumor effect in glioblastoma multiforme. *J Control Release* [Internet]. Elsevier B.V.; 2012;160(3):652–8.
103. Etame AB, Diaz RJ, O'Reilly M a., Smith C a., Mainprize TG, Hynynen K, et al. Enhanced delivery of gold nanoparticles with therapeutic potential into the brain using MRI-guided focused ultrasound. *Nanomedicine Nanotechnology, Biol Med* [Internet]. Elsevier Inc.; 2012;8(7):1133–42.
104. Wei KC, Chu PC, Wang HYJ, Huang CY, Chen PY, Tsai HC, et al. Focused Ultrasound-Induced Blood-Brain Barrier Opening to Enhance Temozolomide Delivery for Glioblastoma Treatment: A Preclinical Study. *PLoS One*. 2013;8(3):1–10.
105. Liu H-L, Huang C-Y, Chen J-Y, Wang H-YJ, Chen P-Y, Wei K-C. Pharmacodynamic and Therapeutic Investigation of Focused Ultrasound-Induced Blood-Brain Barrier Opening for Enhanced Temozolomide Delivery in Glioma Treatment. *PLoS One* [Internet]. 2014;9(12):e114311.
106. Liu H-L, Hua M-Y, Chen P-Y, Chu P-C, Pan C-H, Yang H-W, et al. Blood-brain barrier disruption with focused ultrasound enhances delivery of chemotherapeutic drugs for glioblastoma treatment. *Radiology*. 2010;255(2):415–25.
107. Park EJ, Zhang YZ, Vykhodtseva N, McDannold N. Ultrasound-mediated blood-brain/blood-tumor barrier disruption improves outcomes with trastuzumab in a breast cancer brain metastasis model. *J Control Release*. 2012;163(3):277–84.

108. Aryal M, Park J, Vykhodtseva N, Zhang Y-Z, McDannold N. Enhancement in blood-tumor barrier permeability and delivery of liposomal doxorubicin using focused ultrasound and microbubbles: evaluation during tumor progression in a rat glioma model. *Phys Med Biol* [Internet]. IOP Publishing; 2015;60(6):2511–27.
109. Treat LH, McDannold N, Zhang Y, Vykhodtseva N, Hynynen K. Improved Anti-Tumor Effect of Liposomal Doxorubicin After Targeted Blood-Brain Barrier Disruption by MRI-Guided Focused Ultrasound in Rat Glioma. *Ultrasound Med Biol*. 2012;38(10):1716–25.
110. McDannold N, Arvanitis CD, Vykhodtseva N, Livingstone MS. Temporary disruption of the blood-brain barrier by use of ultrasound and microbubbles: Safety and efficacy evaluation in rhesus macaques. *Cancer Res*. 2012;72(14):3652–63.
111. Liu H-L, Wai Y-Y, Hsu P-H, Lyu L-A, Wu J-S, Shen C-R, et al. In vivo assessment of macrophage CNS infiltration during disruption of the blood-brain barrier with focused ultrasound: a magnetic resonance imaging study. *J Cereb Blood Flow Metab* [Internet]. Nature Publishing Group; 2010;30(1):177–86.
112. Baseri B, Choi JJ, Deffieux T, Samiotaki G, Tung Y-S, Olumolade O, et al. Activation of signaling pathways following localized delivery of systemically administered neurotrophic factors across the blood–brain barrier using focused ultrasound and microbubbles. *Phys Med Biol*. 2012;57(7):N65–81.
113. Kinoshita M, McDannold N, Jolesz FA, Hynynen K. Noninvasive localized delivery of Herceptin to the mouse brain by MRI-guided focused ultrasound-induced blood-brain barrier disruption. *Proc Natl Acad Sci U S A* [Internet]. 2006;103(31):11719–23.
114. Chen PY, Liu HL, Hua MY, Yang HW, Huang CY, Chu PC, et al. Novel magnetic/ultrasound focusing system enhances nanoparticle drug delivery for glioma treatment. *Neuro Oncol*. 2010;12(10):1050–60.

115. Jain RK. Vascular and interstitial barriers to delivery of therapeutic agents in tumors. *Cancer Metastasis Rev.* 1990;9(3):253–66.
116. Chu PC, Chai WY, Hsieh HY, Wang JJ, Wey SP, Huang CY, et al. Pharmacodynamic analysis of magnetic resonance imaging-monitored focused ultrasound-induced blood-brain barrier opening for drug delivery to brain tumors. *Biomed Res Int.* 2013;2013.
117. Yang FY, Ko CE, Huang SY, Chung IF, Chen GS. Pharmacokinetic changes induced by focused ultrasound in glioma-bearing rats as measured by dynamic contrast-enhanced MRI. *PLoS One.* 2014;9(3).
118. Chu P, Chai W, Hsieh H, Wang J, Wey S, Huang C, et al. Pharmacodynamic Analysis of Magnetic Resonance Barrier Opening for Drug Delivery to Brain Tumors. 2013;2013.
119. Vlachos F, Tung Y-S, Konofagou EE. Permeability assessment of the focused ultrasound-induced blood-brain barrier opening using dynamic contrast-enhanced MRI. *Phys Med Biol.* 2010;55(18):5451/–66.
120. Vlachos F, Tung YS, Konofagou E. Permeability dependence study of the focused ultrasound-induced blood-brain barrier opening at distinct pressures and microbubble diameters using DCE-MRI. *Magn Reson Med.* 2011;66(3):821–30.
121. Wintermark M, Maeder P, Thiran JP, Schnyder P, Meuli R. Quantitative assessment of regional cerebral blood flows by perfusion CT studies at low injection rates: A critical review of the underlying theoretical models. *Eur Radiol.* 2001;11(7):1220–30.
122. Jain R. Perfusion CT imaging of brain tumors: an overview. *AJNR Am J Neuroradiol* [Internet]. 2011;32(9):1570–7.
123. Yeung TPC, Wang Y, He W, Urbini B, Gaf R, Ulazzi L, et al. Survival prediction in high-grade gliomas using CT perfusion imaging. *J Neurooncol.* 2015;123(1):93–102.

124. Aviv RI, Esterre CD, Murphy BD, Hopyan JJ, Buck B, Mallia G, et al. Hemorrhagic Transformation of Ischemic Stroke : Prediction with CT Purpose : Methods : Results : Conclusion : 2009;250(3):867–77.
125. Zierler KL. Equations for Measuring Blood Flow By External Monitoring of Radioisotopes. *Circ Res.* 1965;16:309–21.
126. Heilmann M, Kiessling F, Enderlin M, Schad LR. Determination of pharmacokinetic parameters in DCE MRI: Consequence of nonlinearity between contrast agent concentration and signal intensity. *Invest Radiol.* 2006;41(6):536–43.
127. Lee T-Y, Purdie TG, Stewart E. CT imaging of angiogenesis. *Q J Nucl Med.* 2003;47(3):171–87.
128. Gill PE, Murray W. Algorithms for the Solution of the Nonlinear Least-Squares Problem. *SIAM J Numer Anal* [Internet]. 1978;15(5):977–92.
129. Miles KA. Tumour angiogenesis and its relation to contrast enhancement on computed tomography: A review. *European Journal of Radiology.* 1999. p. 198–205.
130. Patlak CS, Blasberg RG. Graphical evaluation of blood to brain barrier transfer constants from multiple time uptake data. Generalizations. *J Cereb Blood Flow Metab.* 1985;5(4):584–90.
131. Crone C. The Permeability of Capillaries in Various Organs as Determined by Use of the “Indicator Diffusion” Method. *Acta Physiol Scand* [Internet]. 1963;58:292–305.
132. Johnson JA, Wilson TA. A model for capillary exchange. *Am J Physiol -- Leg Content* [Internet]. 1966 Jun 1;210(6):1299–303.
133. Renkin E. Transport of potassium-42 from blood to tissue in isolated mammalian skeletal muscles. *Am J Physiol* [Internet]. 1959;197(6):1205–10.

134. St Lawrence KS, Lee TY. An adiabatic approximation to the tissue homogeneity model for water exchange in the brain: II. Experimental validation. *J Cereb Blood Flow Metab.* 1998;18(12):1378–85.
135. Lawson CL, Hanson RJ. Solving Least Squares Problems. *Journal of Chemical Information and Modeling.* 1974. 1689-1699 p.
136. Jain RK, di Tomaso E, Duda DG, Loeffler JS, Sorensen a G, Batchelor TT. Angiogenesis in brain tumours. *Nat Rev Neurosci.* 2007;8(8):610–22.
137. Curry FE, Huxley VH, Adamson RH. Permeability of single capillaries to intermediate-sized colored solutes. *Am J Physiol [Internet].* 1983;245(3):H495–505.
138. Michel CC. Transport of macromolecules through microvascular walls. *Cardiovascular Research.* 1996. p. 644–53.
139. KETY SS. The theory and applications of the exchange of inert gas at the lungs and tissues. *Pharmacol Rev [Internet].* 1951;3(1):1–41.

## Chapter 2

# 2 Focused Ultrasound Sonication with Microbubble Administration Induced Blood-Brain-Barrier Disruption: Quantifying the Increased Endothelial Permeability Surface Area using Dynamic Contrast Enhanced-Computed Tomography in Rabbits

### 2.1 Introduction

The blood-brain-barrier (BBB) consists of endothelial tight junctional complexes surrounded by associated anatomical and functional structures, with a combined purpose to limit solute exchange between the blood and the central nervous system which requires a tightly controlled homeostasis for its proper functioning (1). The undesired consequence is that it is the single most limiting factor in the delivery, and thus development of neurotherapeutics (2). Typically, only lipid soluble drugs with molecular masses less than approximately 500-Da are able to passively diffuse through the lipid bilayer (3).

Over the years, a number of trans-BBB delivery strategies had been experimented with and clinically implemented, but there are limitations related to the invasive nature of these techniques (4) or the non-localized disruption caused by systematically delivered agents that temporarily increase BBB permeability (5). The modification or conjugation of drugs with liposomes (6), nanoparticles (7) or peptide vectors (8) to increase permeability across the BBB has been shown to be promising, but these methods also suffer from toxicity and non-selectivity issues, and would benefit by being supplemented with other approaches.

Recent advances in acoustic technology have opened the door for an exciting new strategy to reversibly disrupt the BBB with the use of focused ultrasound (FUS). FUS allows for the concentration of acoustical energy within a focal spot, with minimal effects to near-field tissue, and can thus be used to non-invasively induce biological effects in the body (9). In the brain, when FUS is pulsed in the presence of intravenously injected

gas filled microbubbles (MB), interactions between the sonicated bubbles and the endothelium induce BBB disruption (10). It has been proposed that the mechanical effects involved in this process may be associated with the mechanical stresses induced to the vessel walls (11) and/or radiation force induced bubble movement (12).

Electron microscopy studies have demonstrated that the disruption was a result of the breakdown and widening of the tight functional complexes that maintain BBB integrity, and was restored within 4 hours at appropriate sonication parameters (13), with no or minimal vascular damage (14,15). Studies have demonstrated that the dynamics of the opening were dependent on different acoustic parameters such as frequency, applied pressure amplitude of the ultrasound, sonication time, burst length, and pulse repetition frequency of the ultrasound, and on the size and dose of MB's (16–18).

FUS sonication with MB administration (FUSwMB) BBB disruption has previously been used in pre-clinical studies to enhance the delivery of a range of molecules across the BBB, including chemotherapeutic agents (19), fluorophores (20), nanoparticles (21), and antibodies (22). However, to translate this technique into clinic, or for therapeutic evaluation in clinical trials, it is necessary to investigate markers that can be used to monitor and measure the increased permeability of the BBB. These markers can also be used as surrogates for predicting drug delivery over the targeted region, which are needed for increased confidence in the results of drug efficacy studies.

Imaging contrast agent techniques, such as gadolinium (Gd)-enhanced magnetic resonance imaging (MRI), are commonly used to qualitatively investigate and characterize BBB disruption (14,16). However, tracer kinetic analysis of dynamic contrast enhanced imaging studies can be used to provide more quantitative and functionally relevant information such as cerebral blood flow (CBF), cerebral blood volume (CBV) and for our interests, the permeability surface area product (PS) of endothelial permeability (P) and surface area (S) of the perfused blood vessels (23). As discussed in Chapter 1 (Section 1.9.5), when PS is much smaller than the volume transfer constant ( $FE$  or  $K_{trans}$ ), it approximates the latter which represents the rate of solute extravasation per unit surface area from the perfused blood vessels into brain

parenchyma. Therefore, PS can act as a surrogate measure to model and predict drug delivery across a target volume of the BBB.

In tracer kinetic modeling, most techniques estimate the volume transfer constant (FE or  $K_{\text{trans}}$ ) instead of estimating F and E separately to permit a calculation of PS according to Equation 1-13 (Chapter 1). Studies in mice using dynamic contrast enhanced (DCE) MRI have demonstrated that  $K_{\text{trans}}$  in the sonicated hemisphere of the brain was found to be at least an order of magnitude higher than that in the contralateral hemisphere, within a range of FUS parameters that induce minimal or no vascular damage (24,25). The study by Park et al also demonstrated that the  $K_{\text{trans}}$  at 30 minutes post FUSwMB showed a linear correlation with doxorubicin delivery over the sonicated region (24).

For quantitative DCE techniques, CT could have advantages over MRI – mainly because of its greater spatial resolution and better quantitative accuracy in measuring tissue and blood contrast concentration (26). DCE-CT (or CT Perfusion) methods have been used to quantify PS in brain tumor patients (27), and also in stroke patients (28). In this study, we present our initial findings evaluating CT Perfusion as a tool for quantifying the increased endothelial PS following FUSwMB induced BBB disruption in a rabbit model.

## 2.2 Methods and Materials

### 2.2.1 Animals

All experiments were approved by the Animal Use Subcommittee of the Canadian Council on Animal Care at our institution. Sixteen rabbits (2.2-4.0 kg) were anaesthetized with 2.5 % isoflurane using a nose cone, before their heads were shaved and depilated and a catheter was inserted into a saphenous vein. Ketamine-xylazine (10:1) was then administered at a rate of 5-10 ml/hr via the catheter as isoflurane was turned off. The first two rabbits underwent FUSwMB where BBB disruption was monitored by MRI followed by CT Perfusion imaging up to 40 minutes post. The remaining fourteen rabbits underwent baseline CT Perfusion imaging before FUSwMB, followed by serial CT Perfusion imaging out to 270 minutes.

Twenty minutes after anesthesia was switched from isoflurane to ketamine-xylazine, baseline CT Perfusion scans were performed, after which the rabbits were placed on the FUS system for FUSwMB. Immediately following sonication, 7-10 ml of Evans Blue (EB) dye was intravenously injected via the saphenous vein catheter and allowed to circulate for the duration of the study for histological confirmation of BBB disruption after sacrifice. Follow-up CT Perfusion scans were performed at 5, 15, 30, 45, 60, 90, 120, 150, 180, 210, 240, and 270 minutes post at which point the rabbit was sacrificed.

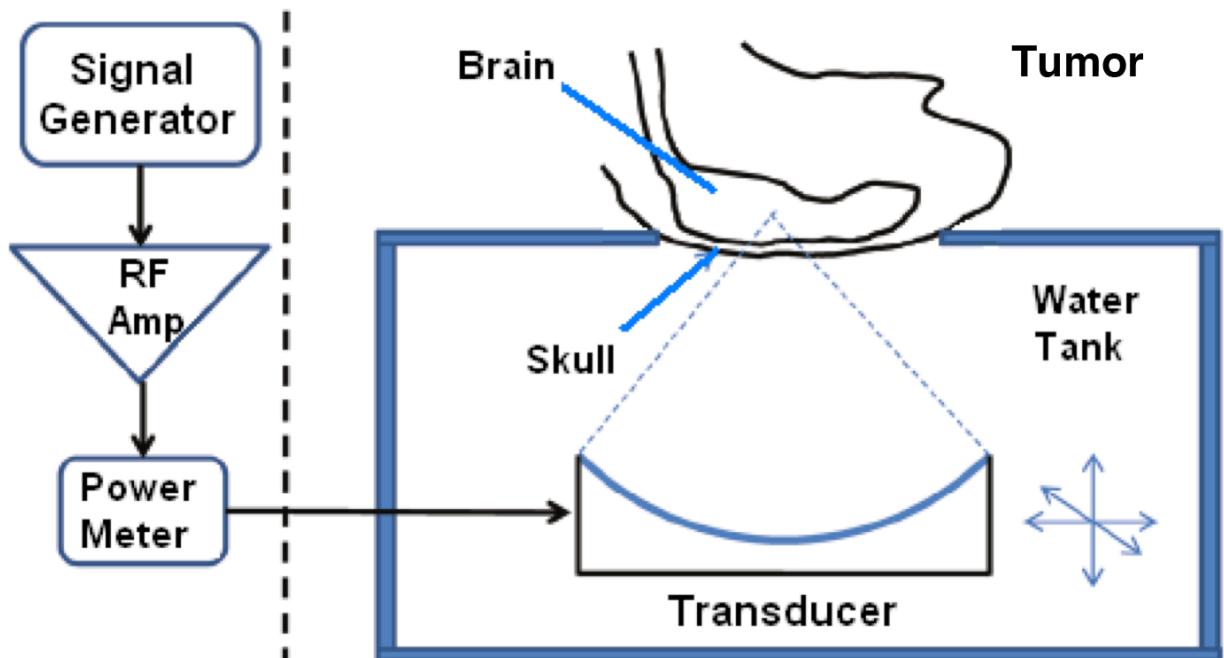


**Figure 2-1: Schematic of the setup of a focused ultrasound with microbubble administration (FUSwMB) experiment, showing the rabbit head placed supine on the surface of the water tank of the FUS instrument, with the focal zone of the focused ultrasound transducer targeted in the brain.**

### 2.2.2 Focused Ultrasound Sonication with Microbubble Administration

The rabbit was placed supine on the FUS system (RK100, FUS Instruments Inc., Canada) and was carefully positioned for optimal trans-cranially sonication, with the transducer aligned orthogonally to the surface of the rabbit's head. A layer of ultrasound gel was

placed on the surface of the skull prior to sonication, to allow for smooth acoustic impedance transition from water in the FUS system to bone in the skull. A schematic of the experimental setup is provided in Figure 2-1. With the rabbit on the FUS system, an axial CT scan (140 kVp, 200mA, 1s rotation time, 2.5 mm slice thickness) was performed to locate a region in the right or left striatum. These coordinates were then input into the FUS system to target the located region.

Each sonication was guided to the selected region and was pulsed with 10ms burst lengths at a 1 Hz pulse repetition frequency, for a 1% duty cycle (DC). The transducer was spherically focused with a diameter of 75mm, a radius of curvature of 60mm, and operated at a frequency of 0.763 MHz. Since this was a pilot study looking to identify a range at which we can measure the increase in BBB PS, we titrated the acoustic powers from 0.5-3.0 W and sonication times from 30-180s. We started at a power of 3 W before decreasing it to a range between 0.5-0.6 W, then began decreasing the sonication time down from 180s. The total applied sonication energy ( $E_{\text{applied}} = \text{Power} \times \text{sonication time}$ ) was noted for each sonication.

A single bolus of Definity (Lantheus Medical Imaging, USA) microbubbles at a dose of 20  $\mu\text{l}/\text{kg}$  and at a 1:10 dilution in saline, was manually injected via the saphenous vein catheter at the start of each sonication. All animals were sonicated once, except the last four rabbits which were sonicated four times, twice in each hemisphere at different locations. In the case of multiple sonications, 5 minutes were allowed to pass between MB injections.

### 2.2.3 Magnetic Resonance Imaging

In the first two rabbits, the sonications were guided by MRI (3T Verio, Siemens) using T2-weighted images (FSE, TE = 61.7 ms, TR = 2000 ms, ETL = 4, FOV = 6 x 6 cm, slice thickness = 1mm, 128 X 128). The BBB disruption was qualitatively confirmed using 0.2 ml/kg Gd (Magnevist, Bayer Pharma) enhanced T1-weighted MRI (FSE, TE = 10 ms, TR = 500 ms) at 20 minutes post sonication before relocating to the CT scanner (VCT, GE Healthcare) where a CT perfusion study was performed at 40 min post. An area of

increased image intensity over the FUS targeted region in the Gd-enhanced T1-weighted images was used to qualitatively confirm BBB disruption.

#### 2.2.4 CT Perfusion Protocol

The CT perfusion study used to quantitatively evaluate the BBB PS adopted a two-phase scanning protocol (First phase: two images per second acquired continuously for 30s with 80 kV, 250 mA, 0.5s rotation time, 2.5 mm slice thickness; Second phase: one image acquired every 15s for another 180 seconds using the same scanning parameters as the first phase). A 5 ml/kg bolus of 300 mg Iodine/ml contrast (Isovue-300, 760 Da) was intravenously infused via the saphenous vein catheter over 5 seconds at the start of the first phase.

#### 2.2.5 Tracer Kinetic Analysis

The Johnson-Wilson-Lee (JWL) distributed parameter model (23,29) was used to model the distribution of injected contrast in the brain (tumor) using permeability surface area product (PS), cerebral blood flow (CBF or F), cerebral blood volume (CBV or  $V_b$ ), and the distribution volume of contrast in the brain parenchyma ( $V_e$ ), as the model parameters. The technique is explained in detail in Chapter 1 (Section 1.9.4) of this thesis. One internal carotid artery was identified in the source CT perfusion images and a 2 x 2 pixel region was placed in the artery to generate the time-density curve which was used as an arterial input function,  $C_a(t)$  to the JWL model. A typical arterial time density curve (input function) and the tissue time density curve,  $Q(t)$  from a rabbit study are shown in Figure 2-2.

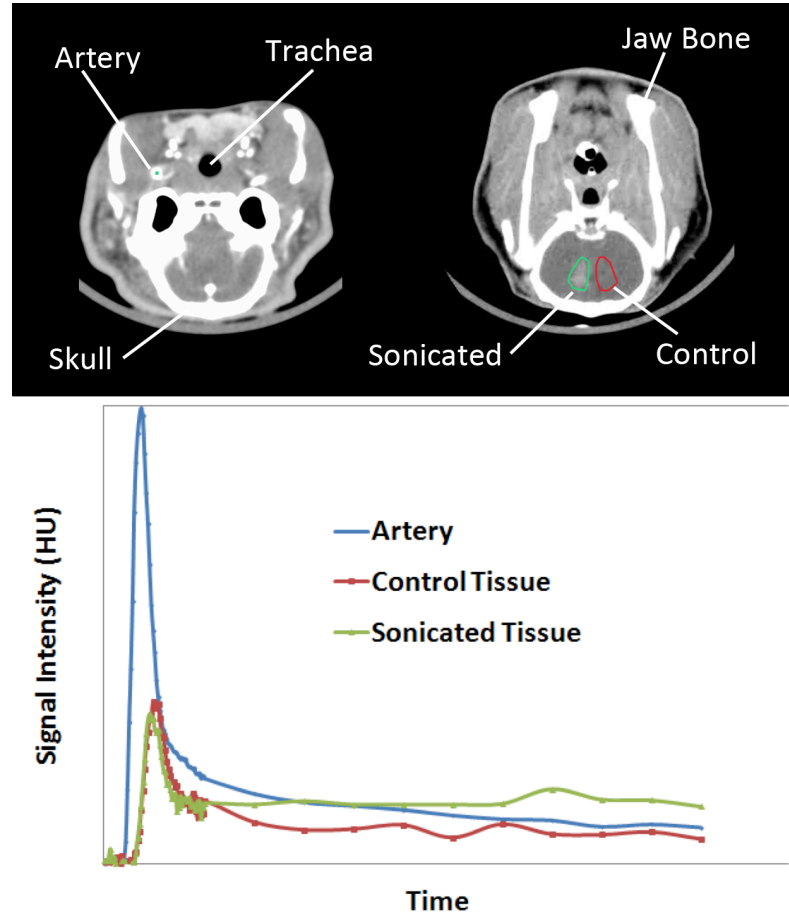


**Figure 2-2: Coronal head CT images of a representative rabbit, acquired with Iovue contrast injection, following focused ultrasound with microbubble administration (FUSwMB). The 2x2 voxel arterial input region of interest (ROI) and corresponding arterial time density curve,  $C_a(t)$ , along with sonicated and control ROIs in the striata, and their corresponding time density curves  $Q(t)$  are presented.**

Under the assumptions that brain blood flow ( $F$  or  $CBF$ ) is constant and  $Q(t)$  is linear with respect to the arterial concentration of contrast  $C_a(t)$ ,  $Q(t)$  is the product of  $F$  and the convolution of the arterial input function and the impulse residue function,  $R(t)$ , of the JWL model, as shown in Equation 2-1.

$$Q(t) = F \cdot [C_a(t) * R(t - T_0)] \quad \dots \text{Equation 2-1}$$

$R(t)$  is defined as:

$$R(t) = \begin{cases} 1, & 0 < t \leq \frac{V_b}{F} \\ E e^{-\frac{FE}{V_e}(t - \frac{V_b}{F})} H(t - \frac{V_b}{F}), & t > \frac{V_b}{F} \end{cases} \quad \dots \text{Equation 2-2}$$

where  $T_0$  is the appearance time of contrast agent in the brain relative to that in the input artery,  $V_b$  (or CBV) is the volume of contrast distributed in the intravascular space,  $E = 1 - e^{-\frac{PS}{F}}$  is the extraction fraction, and  $H$  is the unit step function. As shown in Equation 2-2,  $R(t)$  of the JWL model is parameterized by  $F$  (or CBF),  $PS$ ,  $V_b$  (or CBV), and  $V_e$ , the distribution volume in the tissue. CT Perfusion 5 (a prototype of CT Perfusion 4D, GE Healthcare, Waukesha, Wis) was used to estimate and generate parametric maps of  $PS$ ,  $CBF$ , and  $CBV$ , by iteratively changing their values until an optimum fit to the tissue time density curve,  $Q(t)$  is reached according to Equations 2-1 and 2-2.

### 2.2.6 CT Perfusion Map Analysis

CT Perfusion derived  $PS$  map was used to measure the increase in endothelial  $PS$  following FUSwMB. An elliptical region of interest (ROI) with an area of  $20 \text{ mm}^2$  was placed over the center of the FUS target to cover the focal zone of the transducer, and the control ROI was defined as a duplicate in the contralateral hemisphere. The FUS transducer focal zone was defined as 3 dB of intensity pressure, and had a cross sectional focal area of approximately  $10 \text{ mm}^2$  and a volume of approximately  $33 \text{ mm}^3$ . The sonicated and control ROIs defined on the  $PS$  map from the baseline study were superimposed on the follow-up maps, after the different studies were manually registered using the skull and vascular markers.

### 2.2.7 Histology

Following CT Perfusion imaging, the rabbits were anaesthetized using 5% Isoflurane for 2 minutes, euthanized by 3 ml of intravenous potassium chloride, then perfusion fixed

with 4% paraformaldehyde before the brain was removed intact and left in a 10% formalin solution until histological analysis. For gross histological analysis, the brains were coronally sliced into 4-mm thick sections using a rabbit brain matrix (ProTech International, Lowell, NC) visually assessed for EB dye leakage as confirmation of BBB disruption and hemorrhagic lesion for tissue damage. For three representative rabbits, the sonicated slices were embedded in paraffin, sliced into 20- $\mu$ m sections, stained with hematoxylin and eosin (H&E), and the sonicated regions examined under a microscope.

## 2.2.8 Statistical Analysis

The difference in the likelihood of lesions between cases with applied powers of 1.0 W or above, compared with applied powers between 0.5 – 0.6 W with sonication time of 150 – 180, or with sonication time of 120 s or less were assessed using Fisher's Exact test, with Bonferroni correction applied to account for 3 comparisons ( $m = 3$ ). For statistical comparison of the effects of varying applied energy on the dynamics of the induced disruption, all the sonications with a sonication time of 180 s were retrospectively grouped into those that caused visible lesions from histology ( $n=8$ ), and those that did not ( $n=4$ ). The differences in CT Perfusion derived PS between time points were assessed using Mann-Whitney U Tests, with Bonferroni correction applied to account for 3 comparisons ( $m = 3$ ), comparing baseline with the peak PS and 180 min post, and the peak PS with 180 min post. The peak PS was defined as the time point when the highest PS following FUSwMB was measured. Regression analysis was used to investigate the correlation between  $E_{\text{applied}}$  and PS. Akaike's information criterion (AIC) was then used to test which regression model (linear vs. exponential) provides the best model fit. Logistic regressions were also used to investigate the association between the presence of EB leakage with PS at the peak and at 3 hours post sonication, the presence of a lesion with PS at the peak and at 3 hours post sonication, the presence of EB leakage with applied sonication power and  $E_{\text{applied}}$ , and the presence of a lesion with applied sonication power and  $E_{\text{applied}}$ . Significance was determined for rejecting the null hypothesis that the area under the curve (AUC) for the receiver operator curve (ROC) was equal to 0.5. Statistical significance was determined as  $p < 0.05$  for all analyses. All statistical analyses were performed with IBM SPSS v23.

## 2.3 Results

The first goal of the study was to confirm BBB disruption using Gd enhanced T1-weighted MRI in two rabbits, before quantitative evaluation of BBB with CT Perfusion. Both rabbits were sonicated at 3 W for a duration of 180s. Figure 2-3 shows the 10-minute post MR images in the coronal, axial, and sagittal planes, and the 40-minute post axial BBB PS maps for the sonicated. The 40 minute post BBB PS over the sonication region measured from the corresponding functional maps were 3.9 and 4.5 ml/min/100g for rabbits 1 and 2, respectively. At the same timepoint, the untreated contralateral hemisphere BBB PS was 0.0 for both rabbits.

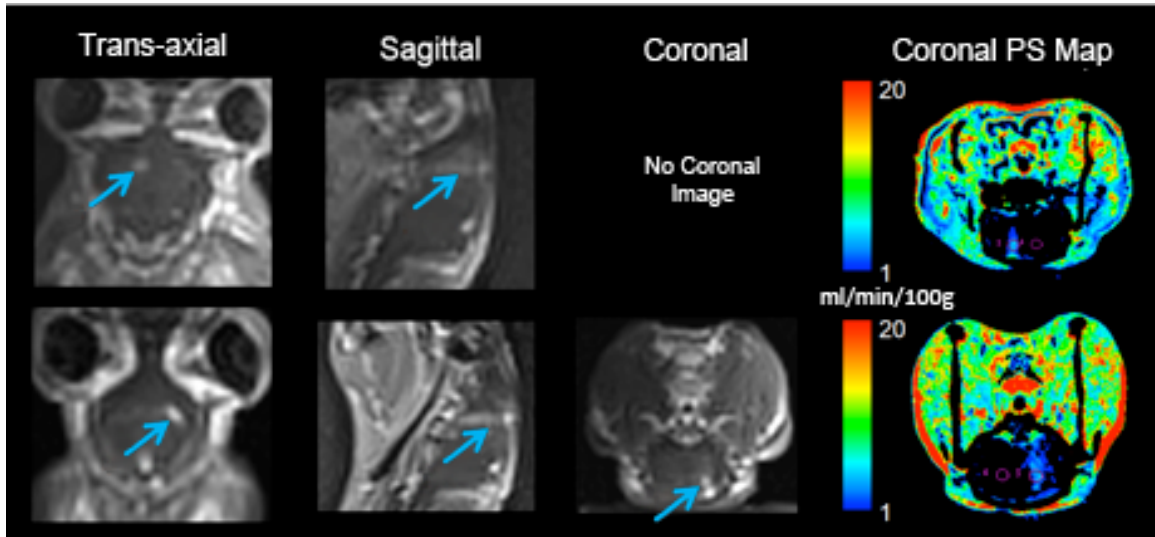
The second goal of this study was to titrate the applied power and sonication time to identify a range of values that can induce a transient increase in BBB permeability, with minimal or no injury in a rabbit model. Table 2-1 summarizes the results for rabbits 3 to 16 including exposure parameters, BBB PS at baseline, the peak, and 180 min post,  $E_{\text{applied}}$  and gross histology results. These experiments started with an applied power of 3.0 W at a constant sonication time of 180 s. Then the applied power was reduced down to a range of 0.5 – 0.6 W, after which the sonication time was reduced from 180 s to 30 s. All 6 cases with an applied power of 1.0 W or above demonstrated lesions at gross histological analysis. When the applied power was 0.5 – 0.6 W and the sonication time between 150 – 180 s, the incidence of lesions dropped to 6 out of 10, which was not significantly different than 1.0 W or above ( $p = 0.1$ ). Only 1 out of 10 cases with 0.5 – 0.6 W applied powers and sonication times of 120 s or less resulted in lesions, which was less likely than sonication times between 150 - 180 ( $p < 0.03$ , but not significant after Bonferroni correction), and less likely than all cases with an applied power of 1.0 W or above ( $p < 0.005$ , remained significant after Bonferroni correction). All the 13 cases that demonstrated lesions also showed signs of EB leakage, but there were 3 cases in which EB leakage was observed in the absence of lesions on gross histology.

**Table 2-1: Summary of Focused Ultrasound (FUS) exposure parameters including applied power, sonication time, and total sonication energy ( $E_{\text{applied}}$ ), as well as permeability surface area product (PS) and gross histology results.**

Rabbit	Power (W)	Time (s)	$E_{\text{applied}}$ (J)	PS Baseline (ml/min/100g)	PS at Peak [time of Peak] (ml/min/100g)	PS 3 hrs post (ml/min/100g)	Lesion/Hemorrhage	EB leakage
3	3.00	180	5.40	0.0	9.4 [5 mins]	3.4	Yes	Yes
4	3.00	180	5.40	0.0	13 [5 mins]	6.6	Yes	Yes
5	3.00	180	5.40	0.0	6.9 [15 mins]	5.5	Yes	Yes
6	2.00	180	3.60	0.2	6.3 [5 mins]	3.1	Yes	Yes
7	1.50	180	2.70	0.1	6.4 [5 mins]	3.1	Yes	Yes
8	1.00	180	1.80	0.3	8.5 [5 mins]	6.2	Yes	Yes
9	0.50	180	0.90	0.1	1.1 [15 mins]	0.1	No	No
10	0.60	180	1.08	0.0	1.1 [15 mins]	0.1	No	No
11	0.60	180	1.08	0.3	2.4 [15 mins]	0.7	No	Yes*
12	0.60	180	1.08	0.0	4.1 [5 mins]	0.9	Yes	Yes
13	0.60	180	1.08	0.2	1.8 [30 mins]	0.1	No	Yes*
	0.55	180	0.99	0.1	5.2 [15 mins]	2.6	Yes	Yes
	0.60	150	0.90	0.2	4.7 [30 mins]	2.7	Yes	Yes
	0.55	150	0.83	0.1	3.3 [15 mins]	1.0	Yes	Yes
14	0.55	150	0.83	0.1	3.9 [30 mins]	3.0	Yes	Yes
	0.50	150	0.75	0.0	4.0 [30 mins]	3.4	Yes	Yes
	0.55	120	0.66	0.1	2.1 [30 mins]	1.4	Yes	Yes
	0.50	120	0.60	0.1	1.2 [15 mins]	0.3	No	Yes*
15	0.60	120	0.72	0.1	0.4 [15 mins]	0.2	No	No
	0.60	90	0.54	0.1	0.2 [30 mins]	0.2	No	No
	0.60	60	0.36	0.1	0.3 [15 mins]	0.3	No	No
	0.60	30	0.18	0.1	0.2 [15 mins]	0.2	No	No
16	0.55	120	0.66	0.2	0.9 [5 mins]	0.1	No	No
	0.55	90	0.50	0.1	0.6 [15 mins]	0.2	No	No
	0.55	60	0.33	0.1	0.5 [15 mins]	0.1	No	No
	0.55	30	0.17	0.1	0.1 [15 mins]	0.1	No	No

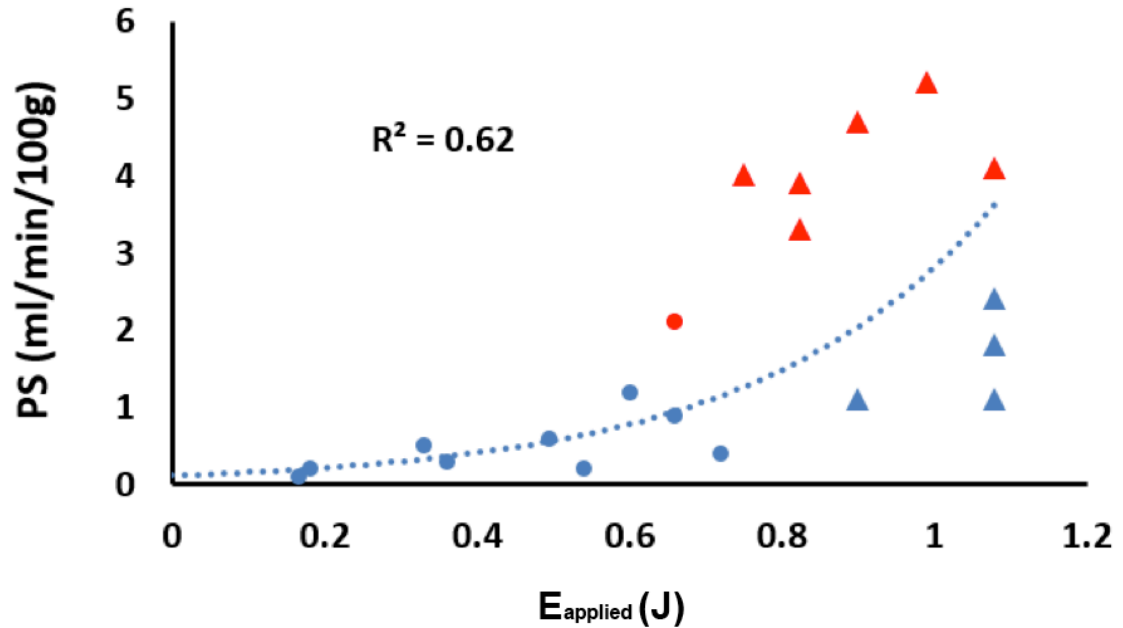
\* Cases showed EB leakage without any visible tissue damage

To better investigate the effect of total applied sonication energy ( $E_{\text{applied}}$ ), the peak PS values were plotted against it in Figure 2-4. The sonications were identified by the presence of lesions (red) and no lesion (blue) at gross histology, and sonication times less than 120 s (triangles), or 150 and 180 s (circles).  $E_{\text{applied}}$  and peak PS showed a stronger fit with an exponential curve ( $R^2 = 0.62$ ) than a linear relationship ( $R^2 = 0.40$ ). The AIC determined that the exponential regression was a significantly better fit than the linear regression ( $p < 0.005$ ).



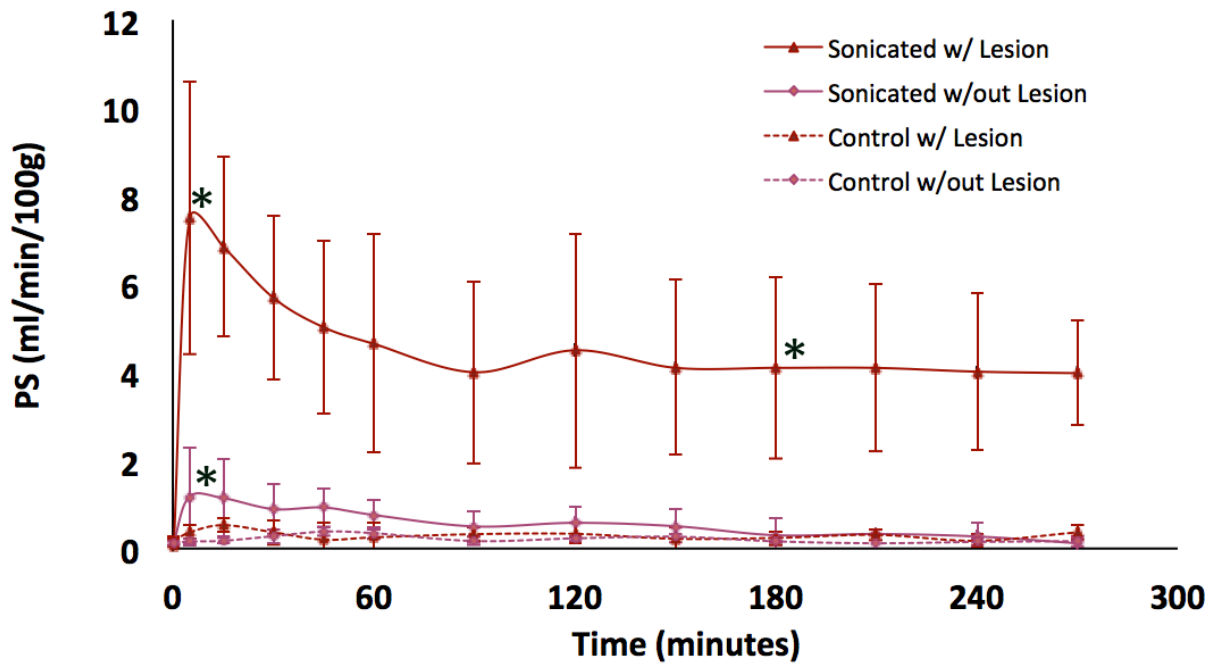
**Figure 2-3: Gadolinium (Gd) enhanced T1-weighted magnetic resonance imaging (MRI) in multiple planes and blood-brain-barrier (BBB) permeability surface area product (PS) maps for two rabbits that demonstrated BBB disruption. In MR images, the regions of increased BBB permeability are indicated with blue arrows.**

For the group that demonstrated lesions over the sonicated region (lesion group), the BBB PS at the peak ( $7.5 \pm 3.1$  ml/min/100g;  $p < 0.0005$ , significant after Bonferroni correction), and at 180 min post ( $4.1 \pm 2.1$  ml/min/100g;  $p < 0.0005$ , significant after Bonferroni correction) were significantly higher than baseline ( $0.1 \pm 0.1$  ml/min/100g). The BBB PS at the peak was also significantly higher than that at 180 min post ( $p < 0.0005$ , significant after Bonferroni correction). For the group that did not demonstrate any lesions over the sonicated region (non-lesion group), the BBB PS was significantly higher at the peak ( $1.2 \pm 1.1$  ml/min/100g;  $p < 0.005$ , significant after Bonferroni correction), when compared to baseline ( $0.1 \pm 0.1$  ml/min/100g), and the BBB PS at the peak was significantly higher than at 180 min post ( $0.3 \pm 0.3$  ml/min/100g;  $p < 0.005$ , significant after Bonferroni correction). However, there was no difference in BBB PS between baseline and 180 min post ( $p = 0.2$ ). These differences can be visualized in the averaged BBB PS time curves for both the lesion and non-lesion groups, presented in Figure 2-5. The time series of BBB PS maps of the sonicated slice for a representative rabbit that demonstrated a transient disruption, and displayed EB leakage without any visible lesions is shown in Figure 2-6.

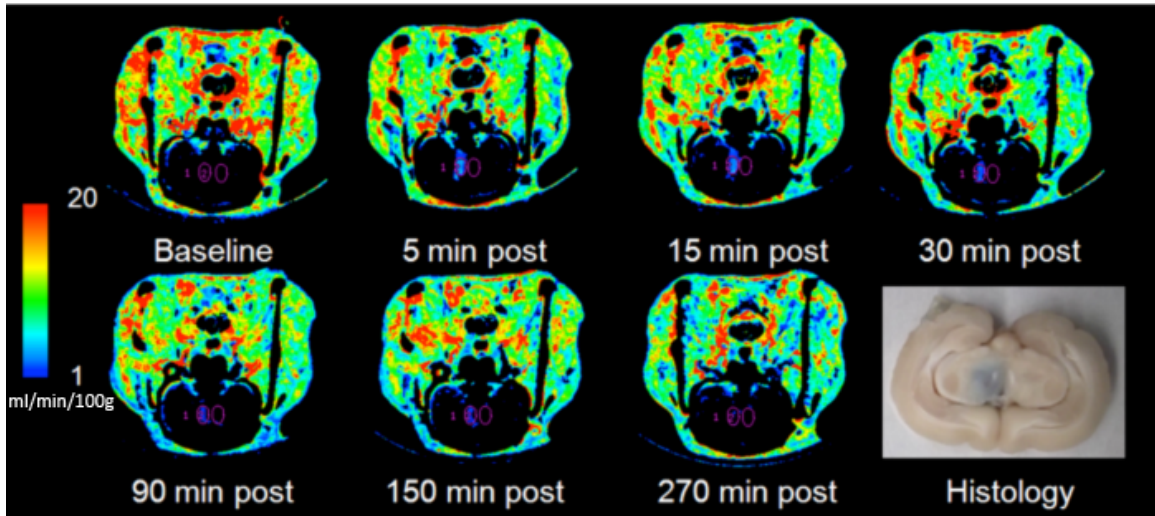


**Figure 2-4: Total applied sonication energy ( $E_{\text{applied}}$ ) plotted against peak permeability surface area product (PS) for all sonications with 0.5 – 0.6 W applied power. The sonications are grouped by the presence of lesions (red) or no lesions (blue) at gross histology, and sonication times of 120 s or less (circles), or 150 and 180 s (triangles).**

Receiver operating curve (ROC) analysis found that peak PS (AUC = 0.994,  $p < 0.001$ ; AUC = 1.000,  $p < 0.005$ ) and 3-hour post PS at sonication (AUC = 1.000,  $p < 0.001$ ; AUC = 0.950,  $p < 0.005$ ) are strong predictors of EB leakage (Figure 2-7a) and presence of a lesion (Figure 2-7b) respectively. ROC analysis also found that  $E_{\text{applied}}$  (AUC = 0.849,  $p < 0.005$ ) was a predictor of the presence of EB leakage, but applied sonication power (AUC = 0.675,  $p = 0.1$ ) was not (Figure 2-7c), and that  $E_{\text{applied}}$  (AUC = 0.891,  $p < 0.005$ ) was a predictor of the presence of a lesion, but applied sonication power (AUC = 0.644,  $p = 0.2$ ) was not (Figure 2-7d).



**Figure 2-5: The average blood-brain-barrier (BBB) permeability surface area product (PS) vs. time curves for the sonicated and contralateral (control) hemispheres in the rabbits, grouped by those that demonstrated visible lesions over the sonicated region at gross histology (n=8), and those that did not (n=4). Error bars indicate standard deviations. \*Significantly different from baseline value as determined by paired t-tests with Bonferroni correction for multiple comparisons.**



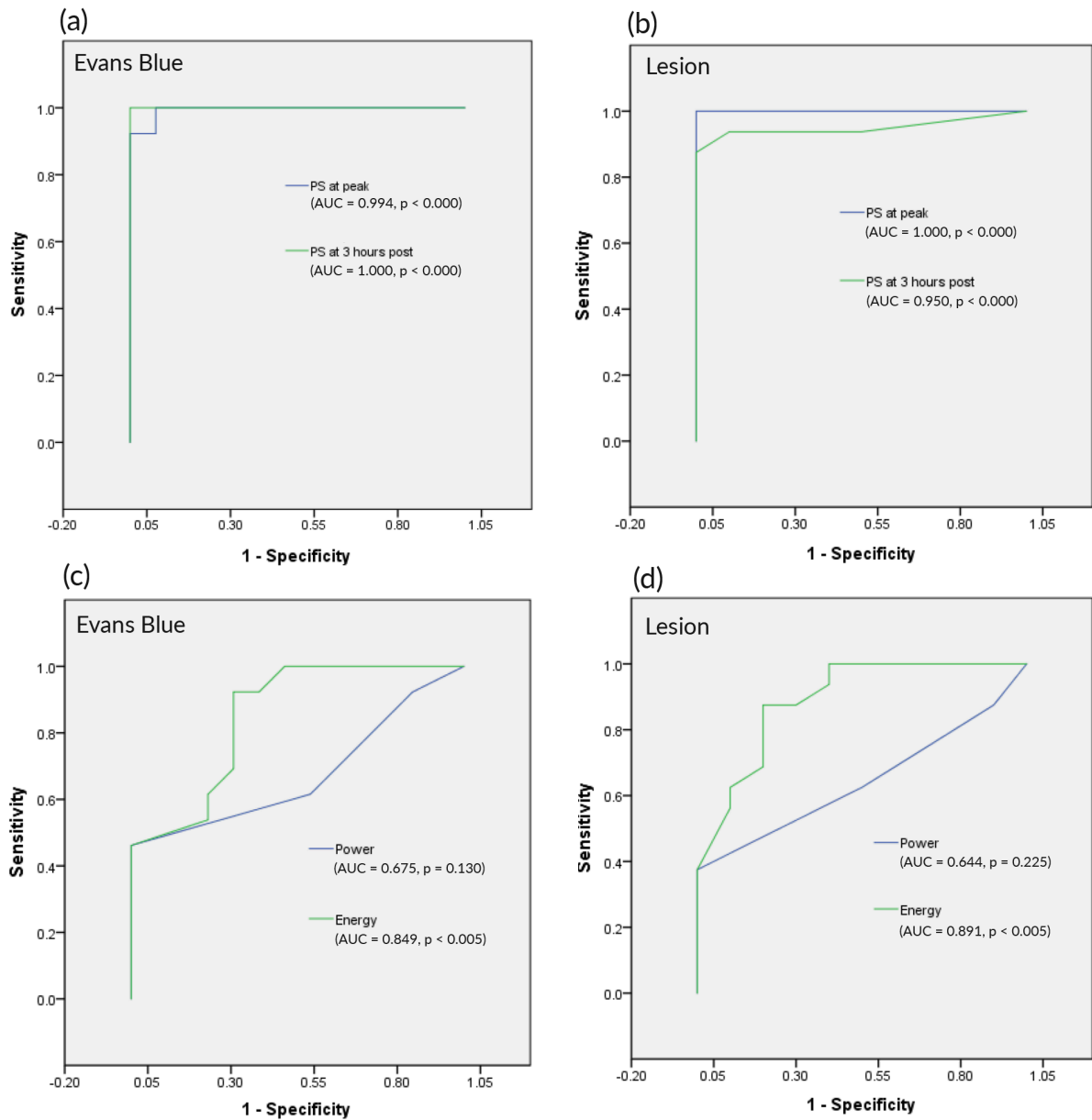
**Figure 2-6: The coronal blood-brain-barrier (BBB) permeability surface area product (PS) maps over time for a rabbit sonicated for 180s at an applied acoustic power of 0.6W that demonstrated reversible increased BBB permeability, Evans Blue (EB) dye leakage, and no visible lesions over the sonicated region.**

Figure 2-8 shows the coronal BBB PS maps and gross histology findings from three rabbits. The first case had a peak PS of 1.1 ml/min/100g, but did not indicate EB leakage or lesions at gross histology; the second case had a peak PS of 2.4 ml/min/100g, showed EB leakage, but did not show any lesion; and the third case which had a peak PS of 8.5 ml/min/100g, showed EB leakage and lesions. In addition, tissue sections from the cases presented in Figure 2-8 were stained with hematoxylin and eosin (Figure 2-9) to investigate the vascular and tissue effects over the range of induced BBB disruption. With sonication at 0.5 W (Figure 2-9a,d) and 0.6 W (Figure 2-9b,e) there were no observed lesions over the sonicated region. With sonication at 1 W (Figure 2-9c,f) there were regions of scattered microhemorrhages without neuronal degeneration (Figure 2-9g), more severe hemorrhagic regions accompanied by selective neuronal necrosis (Figure 2-9h), and ischemic regions accompanied by neuronal necrosis (Figure 2-9i) dispersed over the sonicated region.

## 2.4 Discussion

Our study demonstrates the feasibility of using CT Perfusion derived BBB PS measurements as a tool for measuring the increased PS response following FUSwMB. The first goal of this study was to qualitatively confirm the BBB disruption using Gd-enhanced T1-weighted MRI, before using CT Perfusion to obtain quantitative BBB PS measurements (Figure 2-3). The better quantitative accuracy of CT over MRI techniques relative to changes in contrast concentration provides greater confidence in tracer kinetic model derived measures of PS (30,31). The goal for the second part of the study was to optimize the exposure parameters to obtain a transient BBB disruption with minimal or no damage to the tissue and vasculature. Our results demonstrate a range of exposure values that can be used to induce transient BBB disruption in a rabbit model without adverse vascular and tissue effects.

The optimal power and sonication time for no adverse effects were 0.5 – 0.6 W and 120 s respectively. As the power and sonication times were increased, the likelihood of inducing lesions began to increase. Logistic regressions found that the total applied sonication energy ( $E_{\text{applied}} = \text{Power} \times \text{time}$ ) was a predictor of lesion and EB leakage, but power by itself was not. Histological analysis (Figure 2-9) of the lesions in the sonicated region revealed scattered micro- and more severe hemorrhages, some accompanied by neuronal injury, and signs of ischemia. A study by Chopra et al. investigating the effects of FUS exposure parameters on BBB disruption in rabbits found similar results (16). They showed that for applied power between 0.5 and 4.5W at sonication times of 180 s or above, hemorrhages or lesions accompanied by neuronal injury were seen in all cases, the incidence of which decreased as sonication time was decreased.



**Figure 2-7: Receiver operating Curve (ROC) and the corresponding area under the curves (AUC) for logistic regressions of Evans Blue (EB) leakage with (a) peak permeability surface area product (PS) and 3-hour post PS; the presence of a lesion with (b) peak PS and 3-hour post PS; (c) the presence of EB leakage with applied sonication power and energy, and (d) the presence of a lesion with applied sonication power and energy. The p-value indicates the significance of rejecting the null hypothesis that  $AUC = 0.5$ .**

The relationship between  $E_{\text{applied}}$  and the peak PS was used to evaluate the combined effect of the applied power and sonication time on the induced BBB disruption (Figure 2-4). The fit between  $E_{\text{applied}}$  and peak PS was found to be stronger as an exponential curve ( $R^2 = 0.62$ ) as opposed to a linear relationship ( $R^2 = 0.40$ ). This indicates that there appears to be a threshold at which increased exposure parameters begin to rapidly increase the extent of BBB disruption with respect to  $E_{\text{applied}}$ . We also found that as the induced PS increases, whether at the peak or at 3 hours post, the likelihood of causing tissue effects also increases. This agrees with earlier studies (14,16).

Since the MB was administered intravenously, recirculated bubbles were present throughout the sonication period, as their concentration gradually decreased over the 180 s. Chopra et al. 2010 has previously reported that as the sonication time increases, MB decay results in a plateau of effectiveness in BBB disruption. Goertz et al. 2010 has reported that the decay in MB concentration over time results from FUS cavitation as well as vascular clearance, and can be substantially influenced by FUS exposure parameters. Although we assumed the MB decay remained constant with different exposure parameters used in our study, these prior findings highlight the importance of monitoring the temporal concentration of MB agents at the FUS targeted regions when optimizing FUS induced BBB disruption.

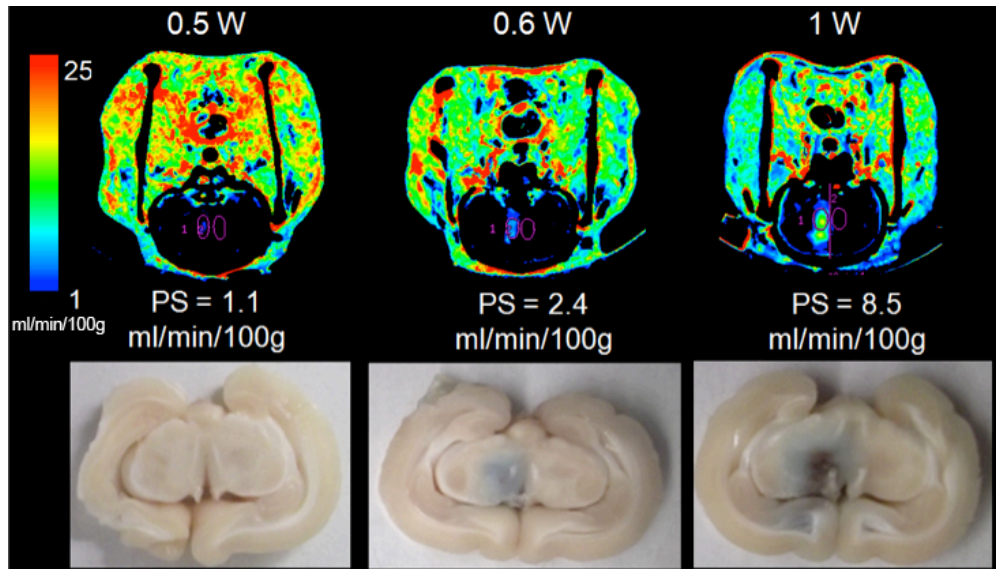


**Figure 2-8: Blood-brain-barrier (BBB) permeability surface area product (PS) maps at 15 min post sonication and gross histology results for 3 cases using acoustic power of 0.5 – 1.0 W and the same sonication time of 180 s.**

All the sonications with a time of 180 s (n=12) were retrospectively grouped into those that showed lesions from gross histology, and those that did not. Induced BBB disruption, by FUSwMB, in cases that did not result in any lesions was transient in nature- the increased PS returned to baseline level at around 3 hours post sonication – indicating a distinct therapeutic window for increased drug delivery in the sonicated region that can be monitored using CT Perfusion (Figures 2-5 and 2-6). For the cases in which lesions were observed, the BBB PS remained significantly elevated when compared to baseline, up until the animals were sacrificed at 5 hours post sonication.

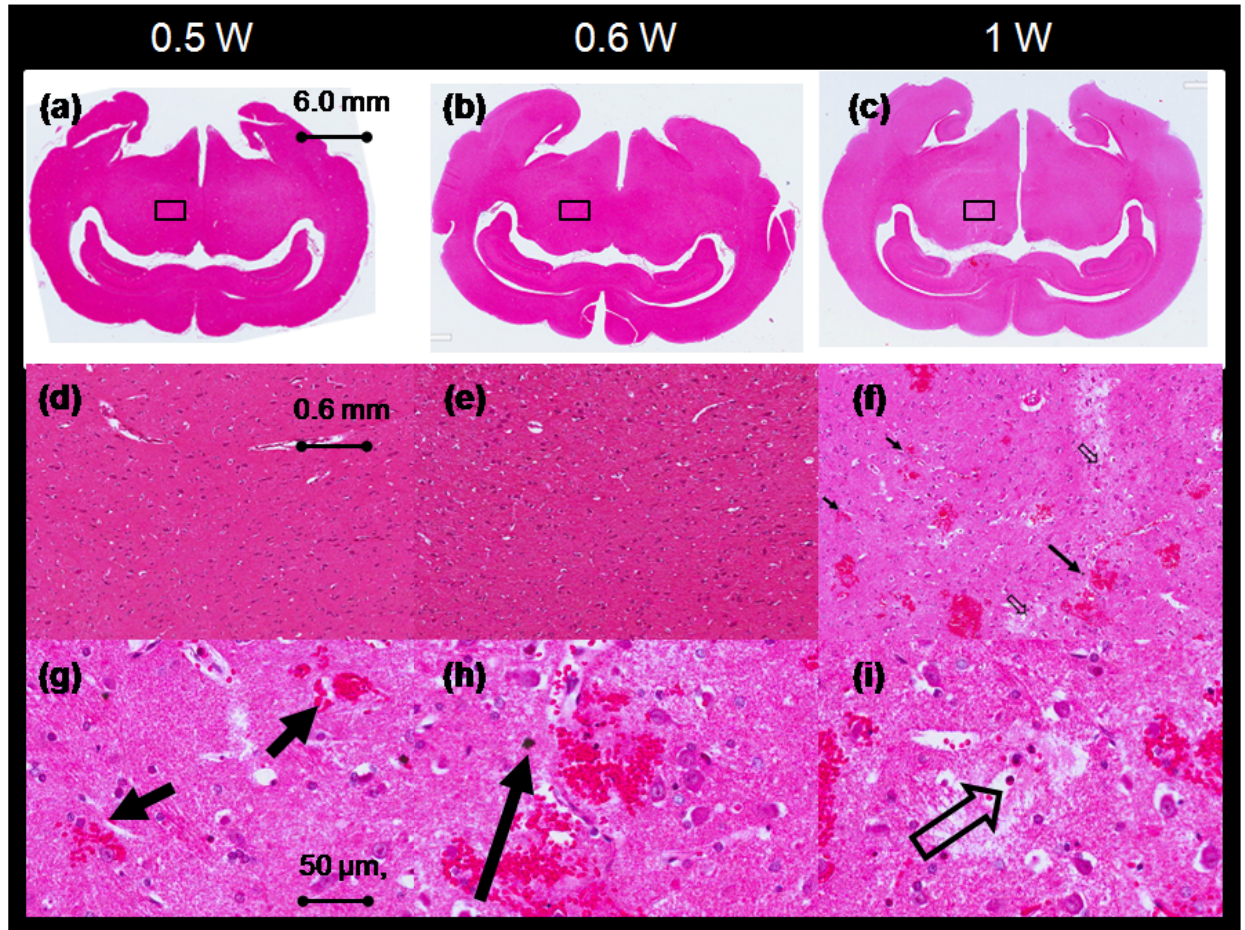


**Figure 2-9: Hematoxylin–eosin (H&E) stained tissue sections (a-c) for the 3 cases shown in Figure 2-8. The middle (d-f) is 10X magnification for corresponding sections (a-c). The bottom row is 120X magnification of distinct pathologies in the case sonicated at 1.0 W (c & f): (g) regions of scattered microhemorrhages without neuronal degeneration (short arrows), (h) more severe hemorrhagic regions accompanied by selective neuronal necrosis (dark-stained neurons, long arrows), and (i) ischemic regions accompanied by neuronal necrosis (hollow arrows).**

Figure 2-8 shows the BBB disruptions in three rabbits at applied sonication powers of 0.5 W, 0.6 W, and 1.0 W respectively, while sonication times were kept at 180 s. EB in blood binds to serum albumin, which has an average molecular size of about 65,000 Da, and other large proteins such that EB extravasation is an indicator of BBB permeability to molecules significantly larger than our contrast agent, which is around 760 Da. This

result suggests that the BBB disruption induced by FUSwMB facilitates delivery of both small and large molecules.

When blood flow (F) is at least 5 times greater than permeability (PS), the flow extraction product (FE) can be approximated by PS, in which case PS can be interpreted as the unidirectional flux of solutes from blood plasma to parenchymal tissue in a unit mass of tissue, and is expressed in units of ml/min/100g. Stated in another way, PS is the volume (mL) of blood that is completely cleared of contrast per minute in a unit mass of tissue by transfer to the interstitial space. As such, the area under PS x drug concentration vs time curve would give the amount of drug delivered to a volume in the brain. This estimation is important not only for accurately quantifying drug delivery in clinical trials, but also to monitor the treatment effect from BBB disruption on the patient in the clinical case.

Endothelial permeability, P, is dependent on both the number of endothelial pores and their size. Given the endothelial pore size, permeability is inversely related to the square root of molecular weight (MW) of a molecule (32).

Then:

$$\frac{P_1}{P_2} = \sqrt{\frac{MW_2}{MW_1}} \quad \dots \text{Equation 2-3}$$

Using this relationship PS measured at one molecular weight can be scaled to that for a different molecular weight. Future histological studies using fluorescent-tagged markers of different molecular weights can validate this relationship between PS and the molecular weight of permeable solutes.

The data in Table 2-1 shows that the minimum peak PS value that showed signs of EB extravasation was 1.2 ml/min/100g. There were also two instances of a peak PS value of 1.1 ml/min/100g that did not show any EB extravasation. From our data set, we can assume that a PS of 1.2 ml/min/100g is the threshold contrast PS that will allow serum albumin bound EB to pass through the FUSwMB disrupted BBB. This study found that

both peak and 3-hr post PS were strong predictors of EB leakage and lesions, indicating that PS is sensitive enough to monitor both the extent of BBB disruption, and the safety of the procedure.

Our findings were consistent with previous studies that have attempted to estimate BBB PS permeability using DCE-MRI through calculation of  $K_{\text{trans}}$  (24,25). In the study by Park, 30 s pulsed sonications with MB administration were applied at exposure parameters that had previously been shown to be safe and cause minimal vascular damage - 0.3 to 0.54 W with 10ms bursts at 1% duty cycle - increased permeability in the sonicated hemisphere to at least an order of magnitude higher than contralateral hemispheres. Doxorubicin delivery was also evaluated in this study and showed a 101 % increase in the sonicated region over the control hemisphere. When  $K_{\text{trans}}$  was plotted against doxorubicin delivery over the sonicated regions, a correlation was observed with  $r=0.7$  (24). Our future studies will also look to correlate the delivery of neurotherapeutics with measurements of PS, as a quantitative marker of drug delivery across the BBB.

A major limitation with using FUSwMB to induce BBB disruption was the variability in the induced BBB disruption, even when sonications with similar exposure parameters, MB dose, and skull thickness were used. Because of the narrow window for which BBB disruption can be safely achieved, it is important to develop mechanisms to adequately control the sonications. Without this control, FUS exposure can either impart excessive forces on the MB resulting in inertial cavitation which is associated with vascular and tissue damage (33), or lead to very small oscillations that are insufficient to induce BBB disruption (34). Recently, the use of real-time acoustic emissions feedback to monitor MB behavior on a burst-by-burst basis has been used to control the harmonics of FUS, by adjusting exposure parameters to avoid those signatures. Spectral content and the strength of emissions can be used to search for harmonic (35) or ultra-harmonic (36) emissions that are indicative of stable cavitation, and therefore a safe and controlled BBB disruption.

## 2.5 Conclusions

This study demonstrates that CT Perfusion is a promising tool for monitoring and measuring the increased BBB PS, following FUSwMB. We present a range of exposure parameters, power and sonication time, that cause transient BBB disruption with and without visible brain injury, in a rabbit model. The PS vs. time profiles allow for the visualization of the distinct window for increased drug delivery following sonication. More importantly, we determined that the threshold contrast PS of  $\sim 1.2$  mL/min/100g would allow serum albumin bound EB dye ( $\sim 65$  kDa) to leak across the FUSwMB disrupted BBB. As this was a pilot study with the goal to determine FUS sonication exposure parameters to induce transient and measurable BBB disruption with little or no damage to the vasculature or tissue, it is limited by the number of animals and the range of exposure parameters used. Future studies can investigate the relationships among the induced PS over time, delivery of different agents, and treatment efficacy for various disease models with prospective study designs.

## 2.6 References

1. Pardridge WM. Recent advances in blood-brain barrier transport. *Annu Rev Pharmacol Toxicol*. 1988;28:25–39.
2. Pardridge WM. The blood-brain barrier: bottleneck in brain drug development. *NeuroRx*. 2005;2(1):3–14.
3. Pardridge WM. Drug transport across the blood-brain barrier. *J Cereb Blood Flow Metab* [Internet]. 2012;32(11):1959–72.
4. Pardridge WM. Blood-brain barrier delivery. *Drug Discovery Today*. 2007. p. 54–61.
5. Kroll RA, Neuwelt EA. Outwitting the blood-brain barrier for therapeutic purposes: Osmotic opening and other means. *Neurosurgery*. 1998. p. 1083–100.
6. Huwyler J, Wu D, Pardridge WM. Brain drug delivery of small molecules using immunoliposomes. *Proc Natl Acad Sci U S A* [Internet]. 1996;93(24):14164–9.
7. Gulyaev AE, Gelperina SE, Skidan IN, Antropov AS, Kivman GY, Kreuter J.

- Significant transport of doxorubicin into the brain with polysorbate 80- coated nanoparticles. *Pharm Res.* 1999;16(10):1564–9.
8. Pardridge WM. Molecular Trojan horses for blood-brain barrier drug delivery. *Current Opinion in Pharmacology.* 2006. p. 494–500.
  9. Hynynen K, McDannold N, Vykhodtseva N, Jolesz F a. Noninvasive MR imaging-guided focal opening of the blood-brain barrier in rabbits. *Radiology.* 2001;220(3):640–6.
  10. Nyborg WL. Biological effects of ultrasound: Development of safety guidelines. Part II: General review. *Ultrasound Med Biol.* 2001;27(3):301–33.
  11. Hosseinkhah N, Goertz DE, Hynynen K. Microbubbles and blood-brain barrier opening: A numerical study on acoustic emissions and wall stress predictions. *IEEE Trans Biomed Eng.* 2015;62(5):1293–304.
  12. Dayton P, Klibanov A, Brandenburger G, Ferrara K. Acoustic radiation force in vivo: A mechanism to assist targeting of microbubbles. *Ultrasound Med Biol.* 1999;25(8):1195–201.
  13. Sheikov N, McDannold N, Sharma S, Hynynen K. Effect of Focused Ultrasound Applied With an Ultrasound Contrast Agent on the Tight Junctional Integrity of the Brain Microvascular Endothelium. *Ultrasound Med Biol.* 2008;34(7):1093–104.
  14. McDannold N, Vykhodtseva N, Raymond S, Jolesz F a., Hynynen K. MRI-guided targeted blood-brain barrier disruption with focused ultrasound: Histological findings in rabbits. *Ultrasound Med Biol.* 2005;31(11):1527–37.
  15. McDannold N, Zhang Y, Vykhodtseva N. Blood-Brain Barrier Disruption and Vascular Damage Induced by Ultrasound Bursts Combined with Microbubbles can be Influenced by Choice of Anesthesia Protocol. *Ultrasound Med Biol.* 2011;37(8):1259–70.
  16. Chopra R, Vykhodtseva N, Hynynen K. Influence of exposure time and pressure amplitude on blood-brain-barrier opening using transcranial ultrasound exposures. *ACS Chem Neurosci.* 2010;1(5):391–8.

17. Vykhodtseva N, McDannold N, Hynynen K. Progress and problems in the application of focused ultrasound for blood-brain barrier disruption. *Ultrasonics*. 2008;48(4):279–96.
18. Wang F, Cheng Y, Mei J, Song Y, Yang Y, Liu Y, et al. Focused ultrasound microbubble destruction-mediated changes in blood-brain barrier permeability assessed by contrast-enhanced magnetic resonance imaging. *J Ultrasound Med*. 2009;28(11):1501–9.
19. Liu H-L, Hua M-Y, Chen P-Y, Chu P-C, Pan C-H, Yang H-W, et al. Blood-brain barrier disruption with focused ultrasound enhances delivery of chemotherapeutic drugs for glioblastoma treatment. *Radiology*. 2010;255(2):415–25.
20. Choi JJ, Wang S, Tung YS, Morrison B, Konofagou EE. Molecules of Various Pharmacologically-Relevant Sizes Can Cross the Ultrasound-Induced Blood-Brain Barrier Opening in vivo. *Ultrasound Med Biol*. 2010;36(1):58–67.
21. Chen PY, Liu HL, Hua MY, Yang HW, Huang CY, Chu PC, et al. Novel magnetic/ultrasound focusing system enhances nanoparticle drug delivery for glioma treatment. *Neuro Oncol*. 2010;12(10):1050–60.
22. Kinoshita M, McDannold N, Jolesz F a., Hynynen K. Targeted delivery of antibodies through the blood-brain barrier by MRI-guided focused ultrasound. *Biochem Biophys Res Commun*. 2006;340(4):1085–90.
23. Lee T-Y, Purdie TG, Stewart E. CT imaging of angiogenesis. *Q J Nucl Med*. 2003;47(3):171–87.
24. Park J, Zhang Y, Vykhodtseva N, Jolesz F a., McDannold NJ. The kinetics of blood brain barrier permeability and targeted doxorubicin delivery into brain induced by focused ultrasound. *J Control Release* [Internet]. Elsevier B.V.; 2012;162(1):134–42.
25. Vlachos F, Tung Y-S, Konofagou EE. Permeability assessment of the focused ultrasound-induced blood-brain barrier opening using dynamic contrast-enhanced MRI. *Phys Med Biol*. 2010;55(18):5451–66.
26. Wintermark M, Maeder P, Thiran JP, Schnyder P, Meuli R. Quantitative

- assessment of regional cerebral blood flows by perfusion CT studies at low injection rates: A critical review of the underlying theoretical models. *Eur Radiol.* 2001;11(7):1220–30.
27. Yeung TPC, Wang Y, He W, Urbini B, Gaf?? R, Ulazzi L, et al. Survival prediction in high-grade gliomas using CT perfusion imaging. *J Neurooncol.* 2015;123(1):93–102.
  28. Aviv RI, Esterre CD, Murphy BD, Hopyan JJ, Buck B, Mallia G, et al. Hemorrhagic Transformation of Ischemic Stroke : Prediction with CT Purpose : Methods : Results : Conclusion : 2009;250(3):867–77.
  29. St Lawrence KS, Lee TY. An adiabatic approximation to the tissue homogeneity model for water exchange in the brain: II. Experimental validation. *J Cereb Blood Flow Metab.* 1998;18(12):1378–85.
  30. Eastwood JD, Lev MH, Wintermark M, Fitzek C, Barboriak DP, Delong DM, et al. Correlation of Early Dynamic CT Perfusion Imaging with Whole-Brain MR Diffusion and Perfusion Imaging in Acute Hemispheric Stroke. *Am J Neuroradiol.* 2003;24(9):1869–75.
  31. Wintermark M, Reichhart M, Cuisenaire O, Maeder P, Thiran JP, Schnyder P, et al. Comparison of admission perfusion computed tomography and qualitative diffusion- and perfusion-weighted magnetic resonance imaging in acute stroke patients. *Stroke.* 2002;33(8):2025–31.
  32. Sarin H. Physiologic upper limits of pore size of different blood capillary types and another perspective on the dual pore theory of microvascular permeability. *J Angiogenes Res [Internet].* 2010;2(1):1–19.
  33. Miller DL, Quddus J. Diagnostic ultrasound activation of contrast agent gas bodies induces capillary rupture in mice. *Proc Natl Acad Sci U S A.* 2000;97(18):10179–84.
  34. Goertz DE, Wright C, Hynynen K. Contrast agent kinetics in the rabbit brain during exposure to therapeutic ultrasound. *Ultrasound Med Biol.* 2010;36(6):916–24.

35. Arvanitis CD, Livingstone MS, Vykhodtseva N, McDannold N. Controlled Ultrasound-Induced Blood-Brain Barrier Disruption Using Passive Acoustic Emissions Monitoring. *PLoS One*. 2012;7(9).
36. O'Reilly M a., Hynynen K. Blood-Brain Barrier: Real-time Feedback-controlled Focused Ultrasound Disruption by Using an Acoustic Emissions-based Controller. *Radiology*. 2012;263(1):96–106.

## Chapter 3

### 3 Comparison of Small (760 Da), and Large (65 kDa) Contrast Agent Dynamic Contrast-Enhanced Computed Tomography to measure Blood-Tumor-Barrier Permeability Surface Response Following Focused Ultrasound Sonication with Microbubble Administration in a C6 Rat Glioma Model

#### 3.1 Introduction

Despite the aggressive treatment regime of surgical de-bulking, radiotherapy, and/or chemotherapy administration, brain tumor remains a difficult challenge because of high rates of recurrence and mortality. Recent interest in therapeutic targeting of angiogenesis has led to the development of bevacizumab, a humanized monoclonal antibody targeting vascular endothelial growth factor (VEGF), which has demonstrated significant responses on magnetic resonance imaging (MRI) among patients with recurrent tumors in phase II clinical trials (1,2). After FDA approval however, two placebo-controlled, randomized trials that combined bevacizumab with the best standard of care for newly diagnosed glioblastoma (GBM) - radiotherapy and temozolamide, showed a 3-to-4 month prolongation of progression free survival, but no significant effect on overall survival (3,4).

As a monoclonal antibody, bevacizumab is a relatively large molecule, with a mass of approximately 149 kDa. Because of its size, delivery across the blood-tumor-barrier (BTB) remains a concern, and needs to be addressed when investigating its efficacy. The dilemma is that while increasing the dose delivered to the tumor may improve treatment outcomes, it will also likely result in substantial systemic toxicity (5). Therefore, it is critical to develop techniques for delivering chemotherapeutic agents across the BTB, such that a sufficiently high therapeutic dose can be delivered to the tumor, while dose to normal brain and the rest of the body is minimized (6).

In brain tumors, and particularly in GBM, BTB breakdown is highly heterogeneous within the tumor, resulting in highly variable permeability within different areas of the same tumor (7). The success of chemotherapy is hampered by these intratumoral heterogeneities (8), especially in areas where the ‘incompletely disrupted’ blood-brain-barrier becomes an obstacle for optimal delivery of chemotherapeutics to the tumor. Another challenge in treating brain tumors is its infiltrative nature, as tumor cells can migrate great distances from the periphery of the tumor (9) and this migration is partly responsible for the high rate of GBM recurrence (10,11). Tumor cells tend to invade individually or in small groups, where they co-opt existing blood supplies for oxygen and nutrients, rather than growing their own de-novo (12). Because of these micro-invasions, using radiotherapy to eradicate diffuse infiltrative glioma, without significantly increasing the toxic effects of treatment from the greater mass of normal tissue irradiated, is difficult to achieve (13,14).

The intact and functional blood-brain-barrier (BBB) is typically permeable only to lipid soluble small molecules with a molecular mass of less than 400 Da (15). As GBM progresses, increased BTB permeability result in vasogenic edema from plasma that leaks into the tumor and surrounding brain (16,17). This together with uncontrolled proliferation of tumor mass are often accompanied by elevated interstitial fluid pressure (IFP) in the tumor (18,19). In the context of drug delivery, elevated IFP is another barrier, particularly for larger molecules such as bevacizumab that are less able to passively diffuse across the BTB (20,21). It can be hypothesized that such large molecules have to rely more on the transvascular pressure gradient for convective flux across the barrier, as opposed to passive diffusion. For this reason, it is important to consider the delivery mechanisms of both small (diffusion and convection) and large molecules (more convection than diffusion) when assessing the tumor microenvironment and transport of a desired chemotherapeutic agent in GBM treatment.

Several BTB permeability-enhancing strategies have been used to increase the delivery and accumulation of drugs within the tumor core and periphery, and can generally be classified into three groups: 1) physically circumventing the BTB, 2) pharmacologically opening the BTB, and 3) increased site-specific delivery across the BTB. The first

approach involves direct delivery into the tumor, bypassing systemic circulation, and involves techniques such as direct intratumoral injection (22), implanting drug-releasing polymers (23), convection-enhanced delivery (24), and intranasal delivery (25). The second approach, which involves enhancing BTB permeability with hypertonic mannitol, alkylglycerols, or a bradykinin analog (11), has been associated with better therapeutic outcomes, but has unacceptable high rates of complications due to lack of specificity (26). The third approach effects localized and transient disruption of the BBB with techniques such as focused ultrasound, photodynamic therapy, and photochemical internalization, with minimal damage to the surrounding brain (27).

In the last decade, pre-clinical studies using focused ultrasound (FUS) sonications with intravenously injected microbubbles (MB) have demonstrated the increased delivery of a range of imaging tracers and therapeutic agents across the BTB. These include small molecules such as Temozolomide, 194 Da (28,29), and Carmustine (BCNU), 214 Da (30), imaging contrast such as Gadolinium-DTPA (Gd-DTPA), 938 Da (31–33), monoclonal antibodies such as Trastuzumab, 145 kDa (34), and liposomal Doxorubicin, 80-90nm (33,35,36). For the translation of this technique into clinic, it is important to evaluate the dynamics and safety of enhanced drug delivery across the BTB from FUS sonication with MB administration (FUSwMB). Therefore, the purpose of this study is to investigate using dynamic contrast-enhanced computed tomography (DCE-CT), also known as CT Perfusion, the change in BTB transport of a standard small, Isovue (760 Da), and large, eXia (65 kDa), contrast agent up to 72 hours following a single episode of FUSwMB.

## 3.2 Methods and Materials

### 3.2.1 Study Protocol and Experimental Groups

All experiments were approved by the Animal Use Subcommittee of the Canadian Council on Animal Care at our institution. Fifteen male Wistar rats (300-450g) were used in this study. For each rat,  $1 \times 10^6$  C6 glioma cells were surgically implanted into the right striatum of the brain, using a stereotactic frame, with coordinates 3 mm to the right, and 1 mm posterior to the center of the bregma, along the coronal suture. Follow-up CT

Perfusion scanning was performed at day 7 post implant, and every 2 days after that, until the following criteria were met at 8-15 days after implantation: 1) the tumor was greater than 3 mm in diameter, measured using the average CT image map (derived by averaging all images of the same slice in the CT Perfusion study), and 2) the tumor permeability surface-area product (PS) was greater than 1 ml/min/100g, at which time the tumors underwent FUSwMB. Anesthesia was induced with 2.5% isoflurane using a nose cone, before the head was shaved and depilated, and a tail vein catheter was inserted.

Ketamine-xylazine (10:1) was then administered at a rate of 5-10 ml/hr via the tail vein catheter as isoflurane was turned off. A baseline CT Perfusion scan was performed 20 minutes after switching isoflurane off, then the rat was placed on the FUS system inside the CT gantry and the tumor underwent FUSwMB under CT image guidance. The animals were separated into an acute group (n=5), where repeat CT Perfusion scans were performed at 0.5, 1, 2, 3, and 4 h post sonication, and a recovery group where the animals were recovered at 1 hour following sonication, and follow-up CT Perfusion scans were performed at 24 and 72 h post (n=10). Animals in the acute group were also sonicated in the contralateral hemisphere as a control for normal BBB response. Following the final follow-up scan, the rats in both acute and recovery group were sacrificed with intravenous administration of potassium chloride solution.

### 3.2.2 Focused Ultrasound Sonication with Microbubble Administration

The rat was placed supine on the FUS system (RK100, FUS Instruments Inc., Toronto, Canada) and was carefully positioned for optimal trans-cranial sonication, with the transducer placed orthogonally to the surface of the head. A layer of ultrasound gel was applied to the skull prior to sonication, to allow for smooth transmission between water in the FUS system and the skull. A schematic of the experimental setup is shown in Figure 3-1. With the rat on the FUS system, an axial CT scan (140 kVp, 200 mA, 1s rotation time, 2.5 mm slice thickness) was performed to locate the brain followed by a baseline CT Perfusion scan (see below for details) to locate the center of the tumor. These coordinates were then input into the FUS system to target the tumor center. All sonications were pulsed at 1 Hz, 0.5 W and a 10 ms burst length (1 % duty cycle) for 120

s. The transducer was spherically focused with a diameter of 75mm, a radius of curvature of 60mm, and operated at a frequency of 0.763 MHz. A single bolus of Definity (Lantheus Medical Imaging, USA) microbubbles in 1:10 saline dilution at a dose of 20  $\mu\text{l}/\text{kg}$  was manually injected via the vein catheter simultaneous with the start of sonication. In the case of multiple sonications, at least 5 minutes were allowed for clearance of MB between each episode of FUSwMB (37).

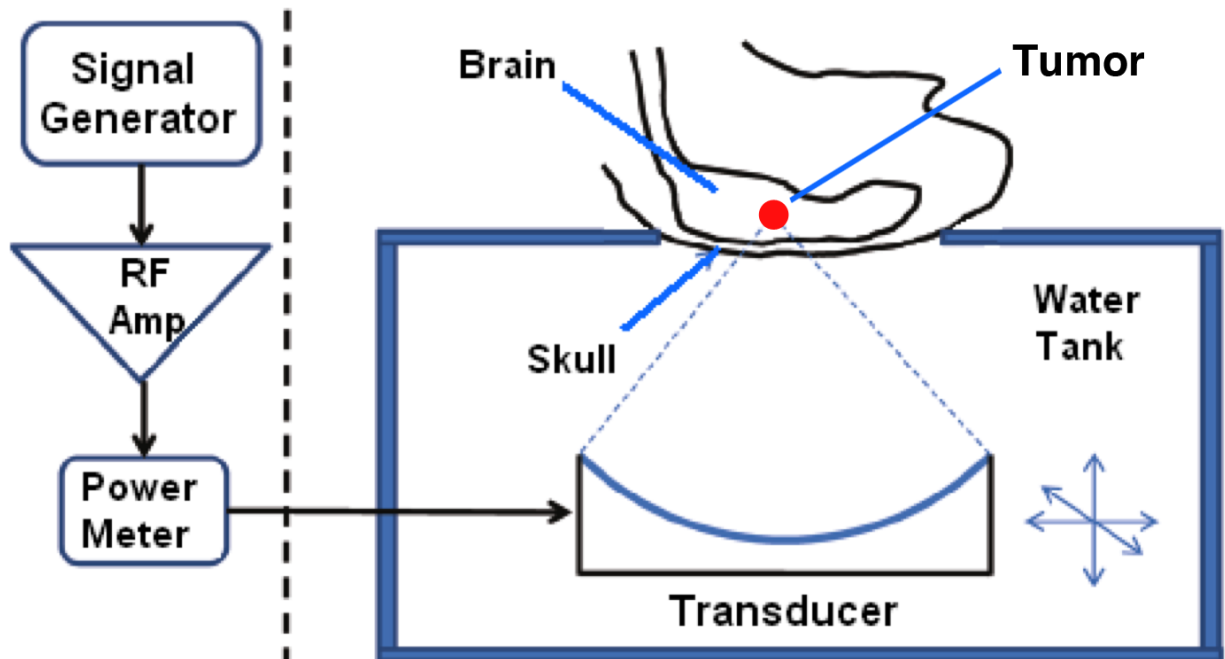


**Figure 3-1: Schematic of the experimental setup - the rat head was placed supine on the surface of the water tank, with the focal zone of the focused ultrasound transducer (FUS) aligned to the tumor.**

### 3.2.3 Dynamic Contrast Enhanced Computed Tomography Perfusion

To quantitatively evaluate the BBB PS and other CT Perfusion derived parameters, a two-phase scanning protocol was used: first phase - two images per second acquired continuously for 30s with 80 kV, 250 mA, 0.5s rotation time, 2.5 mm slice thickness; second phase - one image acquired every 15s for another 180 seconds using the same scanning parameters. A 2.5 ml/kg bolus of 300 mg Iodine/ml (Isovue-300, 760 Da molecular weight), or a 2.5 ml/kg bolus of 160 mg Iodine/ml (eXia, Benitio Biomedical

Inc., 65 kDa molecular weight) was intravenously infused over 5 seconds at the start of the first phase. The acute group was only administered one Isovue CT Perfusion scan per time point, while the recovery group was administered an eXia scan first, followed by an Isovue scan after 10 min of clearance of eXia.

### 3.2.4 Tracer Kinetic Modeling

The Johnson-Wilson-Lee (JWL) distributed parameter model (38,39) was used to model the distribution of injected contrast in the brain (tumor) using permeability surface area product (PS), cerebral blood flow (CBF or F) and cerebral blood volume (CBV or  $V_b$ ) as the model parameters. The technique is explained in detail in Chapter 1 (section 1.9.4) of this thesis. One internal carotid artery was identified in the CT Perfusion images and a 2 x 2 pixel region was placed in the artery to generate the arterial time-density curve which was background subtracted to generate the arterial time-enhancement curve or the arterial input function,  $C_a(t)$  to JWL model. An arterial and the tumor time density curve from a rat study are shown in Figure 3-2.

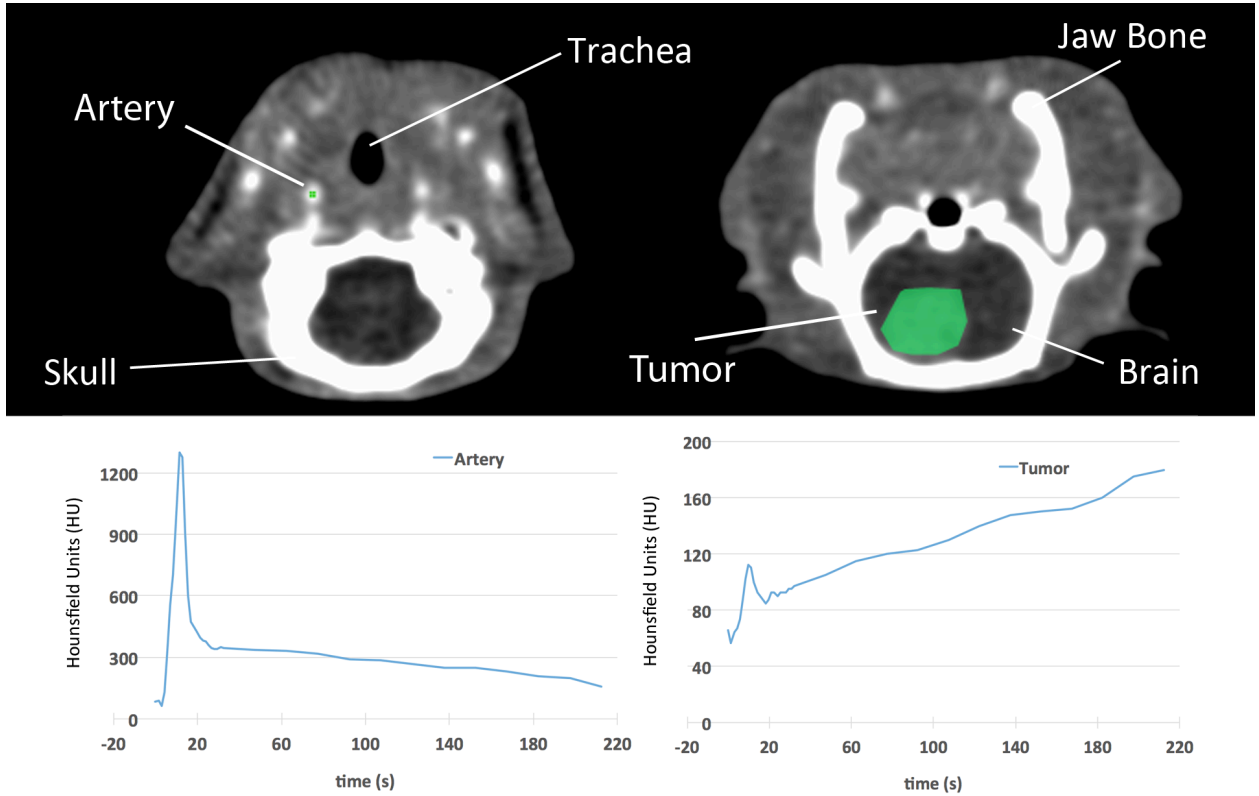


**Figure 3-2: Coronal head CT images of a rat following administration of contrast agent (Isovue). Two slices of the head prior to FUSwMB are shown. A 2x2 voxel arterial input region of interest (ROI) and the corresponding arterial time density curve,  $C_a(t)$ , along with tumor ROI and corresponding tumor time density curve  $Q(t)$  are presented.**

Under the assumption that brain blood flow ( $F$  or CBF) is constant and CT measured signal in artery and brain is linear with respect to the concentration of contrast, the brain time-enhancement curve,  $Q(t)$  is the product of  $F$  and the convolution of the arterial input function and the impulse residue function  $R(t)$ , as shown in Equations 3-1 and 3-2.

$$Q(t) = F \cdot [C_a(t) * R(t - T_0)] \quad \dots \text{Equation 3-1}$$

$$R(t) = \begin{cases} 1, & 0 < t \leq \frac{V_b}{F} \\ E e^{-\frac{FE}{V_e}(t - \frac{V_b}{F})} H(t - \frac{V_b}{F}), & t > \frac{V_b}{F} \end{cases} \quad \dots \text{Equation 3-2}$$

where  $T_0$  is the appearance time of contrast agent in the brain relative to that in the input artery,  $V_b$  (or CBV) is the volume of ‘flowing’ blood that is in large vessels, arterioles, capillaries, venules, and veins,  $V_e$  is the distribution volume of contrast in the extravascular space,  $E = 1 - e^{-\frac{PS}{F}}$  is the extraction fraction, or the fraction of mass that is transferred from the vascular to extravascular space during a single passage of blood from the arteriole end to the venous end of the capillaries of a tissue (40), and  $H$  is the unit step function.

As shown in Equation 3-2,  $R(t)$  of the JWL model is parameterized by  $F$  (or CBF),  $PS$ ,  $V_b$  (or CBV), and  $V_e$ . CT Perfusion 5 (a prototype of CT Perfusion 4D, GE Healthcare, Waukesha, Wis) was used to estimate and generate parametric maps of  $PS$ ,  $CBF$ ,  $CBV$  and  $V_e$ , by iteratively changing their values until an optimal fit to  $Q(t)$  was reached according to Equations 3-1 and 3-2 for each voxel. As discussed in Chapter 1, the volume transfer constant of solutes from blood to interstitial space is  $FE$  instead of  $PS$  (41). The relationship between  $FE$  and  $PS$  is given by the Equation 3-3:

$$FE = F(1 - e^{-\frac{PS}{F}}) \quad \dots \text{Equation 3-3}$$

### 3.2.5 CT Perfusion Map Analysis

The tumor was delineated using thresholds in the baseline  $PS$ ,  $CBF$ , and  $CBV$  maps. A  $PS$  of over 1 ml/min/100g was used as the threshold for the tumor margin, as this value has previously been measured in high-grade brain tumors (42). Relative tumor  $CBF$  and  $CBV$  thresholds of 1.5x with respect to the contralateral hemisphere were also used to guide delineation of the tumor rim (43). An autologous control region in the contralateral hemisphere was also defined.

For the acute group,  $PS$ ,  $CBF$ , and  $CBV$  maps generated using Isovue contrast agent were analyzed to measure the acute response following FUSwMB. The tumor and control ROIs from the baseline maps were superimposed on the follow-up maps, after they were

manually registered together using the skull and vascular structures as landmarks (ImageJ, NIH).

For the recovery group, both Isovue and eXia PS, CBF, and CBV maps were analyzed to measure the response up to 3 days following sonication. The tumor ROIs from the Isovue maps at each time-point were superimposed on the corresponding eXia maps, after the maps were manually registered together as in the acute studies.

### 3.2.6 Statistical Analysis

In the acute group, the differences in Isovue CT Perfusion parameters between time points were assessed using Mann-Whitney U Test, with Bonferroni correction applied to account for 3 comparisons ( $m = 3$ ), comparing baseline with 30, 60 and 240 min post. Similarly, in the recovery group, the differences in Isovue and eXia CT Perfusion parameters between time points were assessed using Mann-Whitney U Tests, with Bonferroni correction applied to account for 3 comparisons ( $m = 3$ ), comparing baseline with 1 h, 24 h, and 72 h post. Regression analysis was used to investigate the correlation between PS, CBF and CBV measured with both contrast agents at all time points. Bland-Altman plots (44) were used to look at the agreement between Isovue and eXia CBF and CBV, with the range of agreement defined as mean bias  $\pm 2$  standard deviations. Statistical significance was determined as  $P < 0.05$ . All statistical analysis was performed with IBM SPSS v23.

## 3.3 Results

In the first 4 hours following FUSwMB in the acute group, the contralateral and tumor Isovue (760 Da) PS, CBF, and CBV over time is shown in Figure 3-3. For the contralateral region with intact BBB, the PS at 30 min post ( $1.1 \pm 0.3$  ml/min/100g) was significantly increased ( $p < 0.01$ , significant with Bonferroni correction) when compared to baseline ( $0.2 \pm 0.06$  ml/min/100g) before returning to baseline at 60 minutes post and thereafter. The tumor PS, which was elevated at baseline, did not show an immediate transient increase, instead decreased gradually over four hours following sonication.

The tumor PS was lower at 240 min post ( $3.9 \pm 2.3$  ml/min/100g;  $p < 0.03$ , not significant after Bonferroni correction) compared to baseline ( $5.9 \pm 3.0$  ml/min/100g). There were decreases in tumor CBF and CBV at 60 min post sonication ( $36 \pm 14$  ml/min/100g;  $p < 0.03$ , not significant after Bonferroni correction) and ( $2.6 \pm 0.8$  ml/min;  $p < 0.02$ , significant after Bonferroni correction) when compared to baseline ( $60 \pm 23$  ml/min/100g) and ( $3.4 \pm 0.9$  ml/min), respectively. Although not significant, there was a trend that tumor CBF and CBV remained suppressed compared to baseline out to 240 minutes following FUSwMB. The contralateral CBF and CBV did not show any significant changes before and following sonication. Sequential PS, CBF, and CBV maps at baseline and following FUSwMB for a rat in the acute group are shown in Figure 3-4.

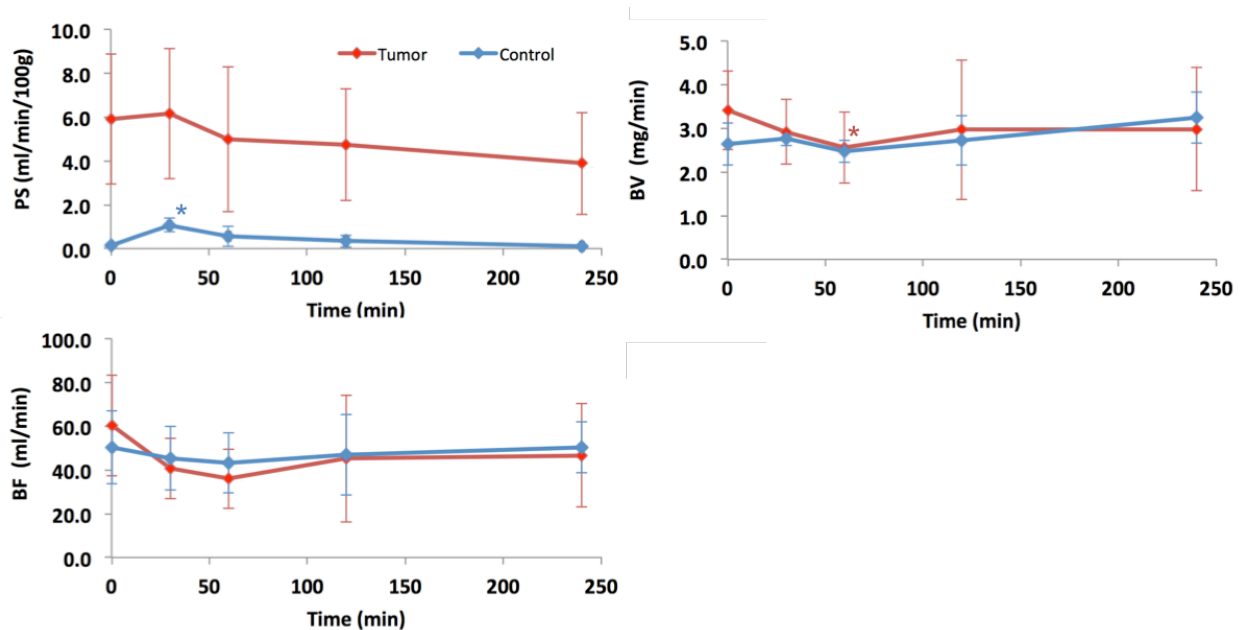


**Figure 3-3: Serial tumor and control Isovue permeability surface area product (PS), cerebral blood flow (CBF), and cerebral blood volume (CBV) measured in the acute group before and over 4 hours following FUSwMB (n=5). \*Significantly different from baseline as determined by Mann-Whitney U test ( $p < 0.05$ ) after Bonferroni correction for multiple comparisons.**

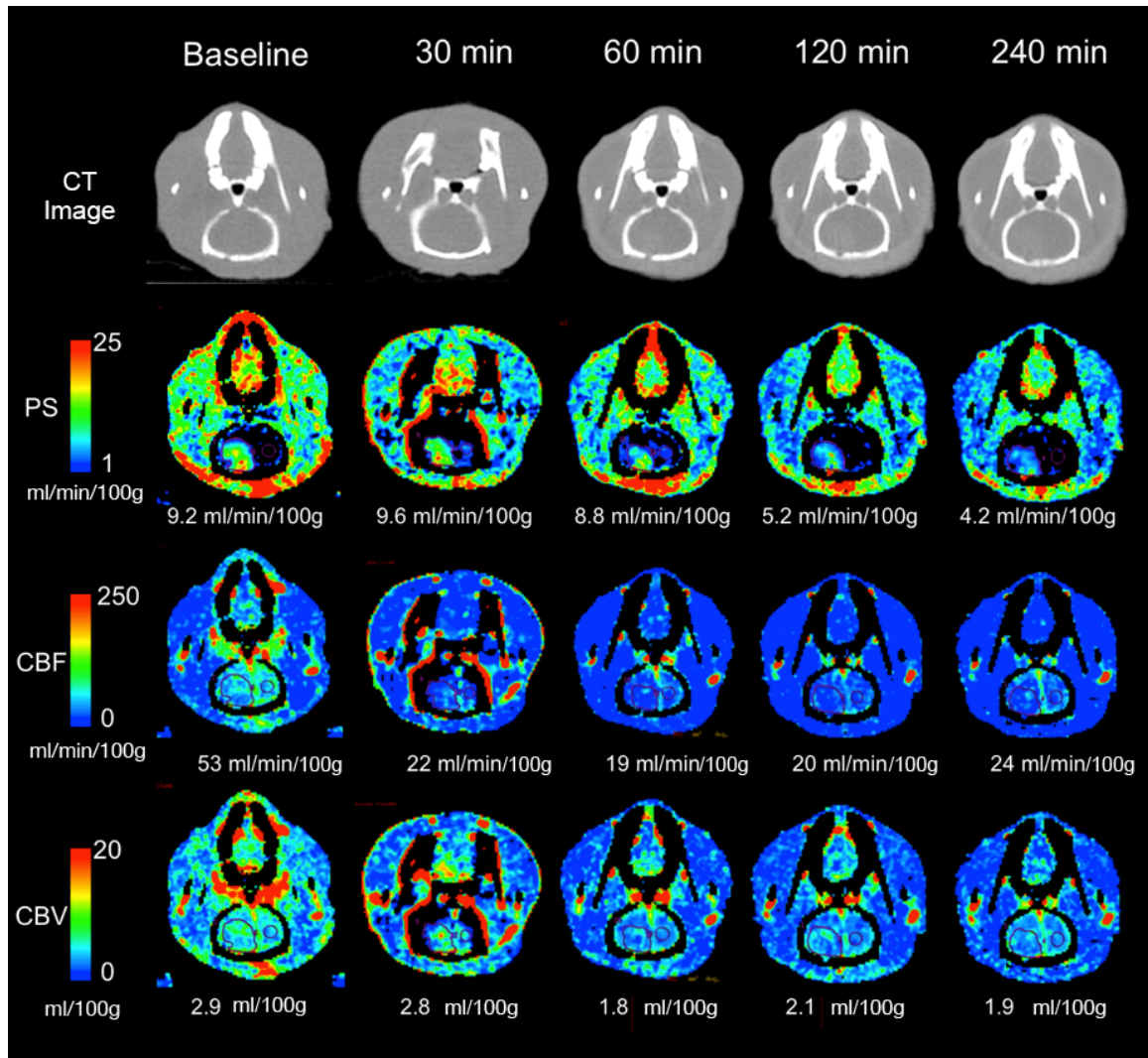


**Figure 3-4: Native CT Image, permeability surface area product (PS), cerebral blood flow (CBF), and cerebral blood volume (CBV) map for a representative animal in the acute group following FUSwMB. Average tumor value is shown beneath each map.**

For the recovery group, tumor PS, CBF, and CBV using both contrast agents over time are shown in Figure 3-5. Tumor Isovue PS was significantly lower at 24 h post ( $6.3 \pm 4.3$  ml/min/100g;  $P < 0.01$ , significant after Bonferroni correction) compared to baseline ( $9.6 \pm 6.6$  ml/min/100g), before returning back to baseline levels at 72 h post sonication ( $8.1 \pm 5.2$  ml/min/100g;  $P = 0.08$ ). In contrast to Isovue PS, there was a trend of increased tumor eXia PS at 24 h post ( $0.13 \pm 0.13$  ml/min/100g;  $P = 0.2$ ) and 72 h post sonication ( $0.16 \pm 0.14$  ml/min/100g;  $P = 0.3$ ), when compared to baseline ( $0.11 \pm 0.09$

ml/min/100g), although neither of these were significant. In addition, for the recovery group, Isovue CBF was higher at 24 h post ( $75 \pm 30$  ml/min/100g;  $P < 0.03$ , not significant after Bonferroni correction), but not at 72 h post sonication ( $69 \pm 26$  ml/min/100g;  $P = 0.07$ ) when compared to baseline ( $62 \pm 19$  ml/min/100g). Similarly, eXia CBF was higher at 24 h post ( $59 \pm 18$  ml/min/100g;  $P < 0.02$ , not significant after Bonferroni correction), but not at 72 h post ( $56 \pm 17$  ml/min/100g;  $p = 0.05$ ), when compared to baseline ( $46 \pm 7$  ml/min/100g). Isovue CBV and eXia CBV at 24 h post ( $4.4 \pm 1.3$  ml/100g and  $4.4 \pm 1.2$  ml/100g; both  $P < 0.03$ , not significant after Bonferroni correction) were both higher than baseline ( $3.8 \pm 0.8$  ml/100g and  $3.5 \pm 0.8$  ml/100g) respectively, but those at 72 h post sonication ( $3.9 \pm 1.0$  ml/100g and  $3.7 \pm 0.9$  ml/100g;  $P = 0.2$  and  $P = 0.1$ ) respectively, were not. A comparison of tumor Isovue and eXia PS maps for a representative subject at different time points in the recovery are shown in Figure 3-6.

Figure 3-7 shows the correlations of tumor PS, CBF, and CBV measured with both contrast agents for all time-points as well as Bland-Altman plots investigating the agreement between Isovue and eXia derived CBF and CBV. When measurements from all rats were considered, there was no correlation of PS measured with Isovue and eXia ( $p = 0.3$ ). Isovue and eXia CBF were moderately correlated ( $R^2 = 0.63$ ,  $m = 0.51$ ;  $p < 0.005$ ), as were Isovue and eXia CBV ( $R^2 = 0.48$ ,  $m = 0.71$ ;  $p < 0.005$ ). Bland-Altman plots were used to investigate the agreement between Isovue and eXia derived CBF and CBV. The Bland-Altman analysis indicates that Isovue and eXia CBF had a mean bias of 19.1 ml/min/100g, with the 95% limits of agreement ranging from -18.9 to 57.0 ml/min/100g, while for CBV, the mean bias was 0.82 ml/100g, with 95% limits of agreement ranging from -2.34 ml/100g to 3.98 ml/100g.

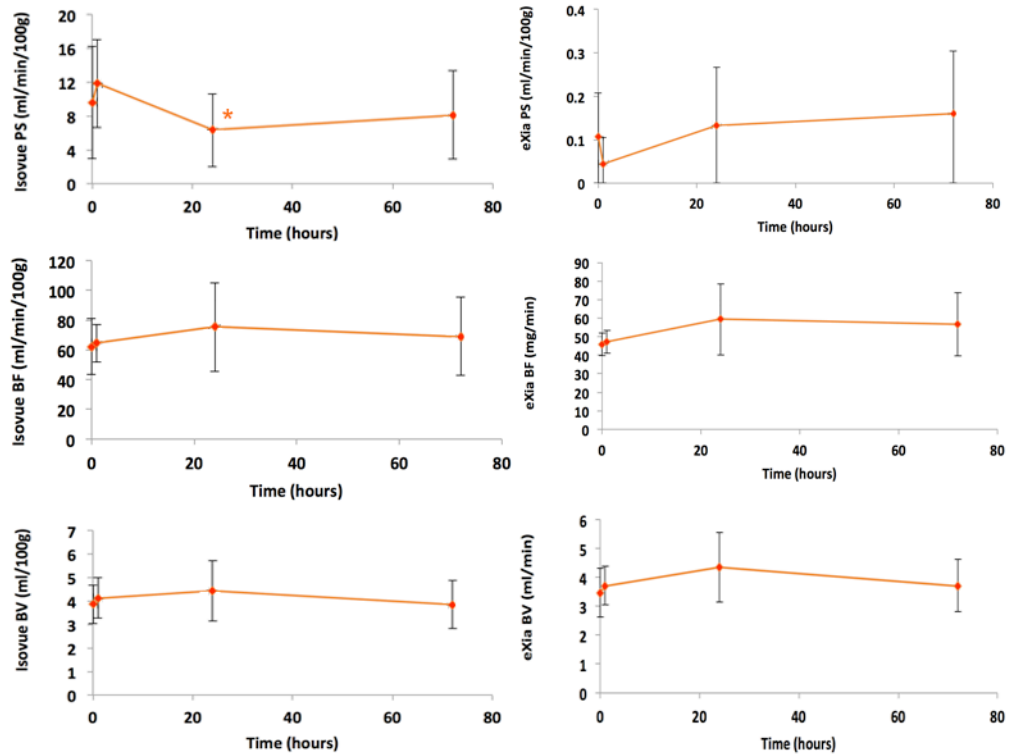


**Figure 3-5: Serial tumor permeability surface area product (PS), cerebral blood flow (CBF), and cerebral blood volume (CBV), measured with Isovue (760 Da), and eXia (~65 kDa), in the recovery group before and over 72 hours following FUSwMB (n=10). \*Significantly different from baseline as determined by Mann-Whitney U test ( $P < 0.05$ ) after Bonferroni correction was applied.**

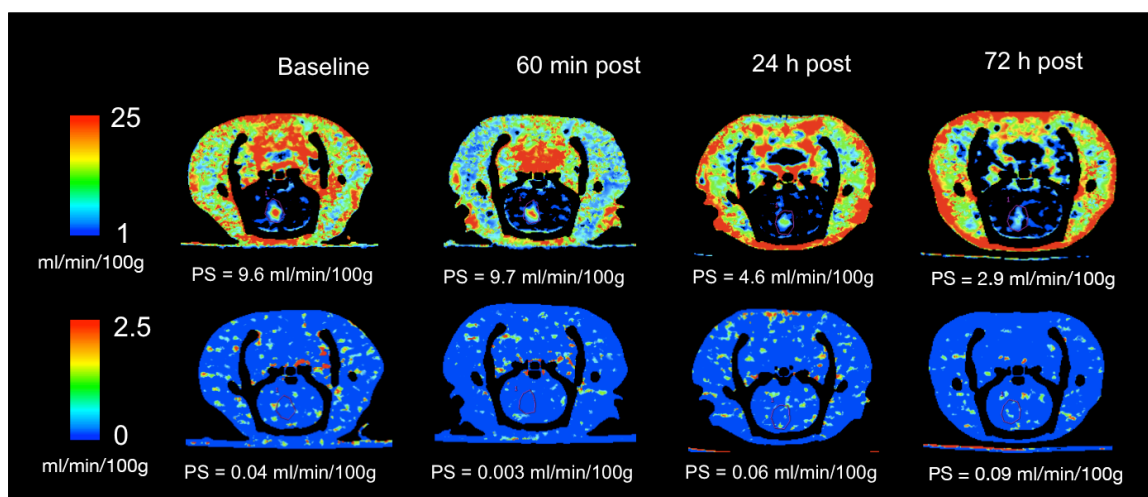


**Figure 3-6: Permeability surface area product (PS) maps, measured with Isovue (760 Da), and eXia (65 kDa) contrast agents, for a representative animal in the recovery group before and following FUSwMB.**

### 3.4 Discussion

This study uses CT Perfusion derived permeability surface product (PS) and perfusion measurements, from data obtained with a standard small (Isovue, 760 Da) and a large (eXia, ~65 kDa) molecular weight CT contrast agent to investigate the tumor response over 4 hours and over 3 days following FUSwMB in a C6 rat glioma model.

The purpose of the first part of this study was to evaluate the tumor permeability surface product response over 24 hours following FUSwMB, at the same FUS exposure parameters, as determined in Chapter 2 of this thesis, which were titrated to induce transient BBB disruption in the normal brain with minimal damage. Surprisingly, the tumor Isovue PS, which was elevated at baseline, demonstrated a gradual decrease over four hours following sonication, instead of a significant immediate and transient increase that was seen with the intact BBB in Chapter 2.

To expand on these findings, a second group of rats underwent FUSwMB, but were recovered from anesthesia at 1 h post sonication and underwent follow-up CT Perfusion studies at 24 and 72 h. post. We found that tumor Isovue PS remained decreased and was

significantly lower at 24 h post, compared to baseline, before returning to baseline levels at 72 h.

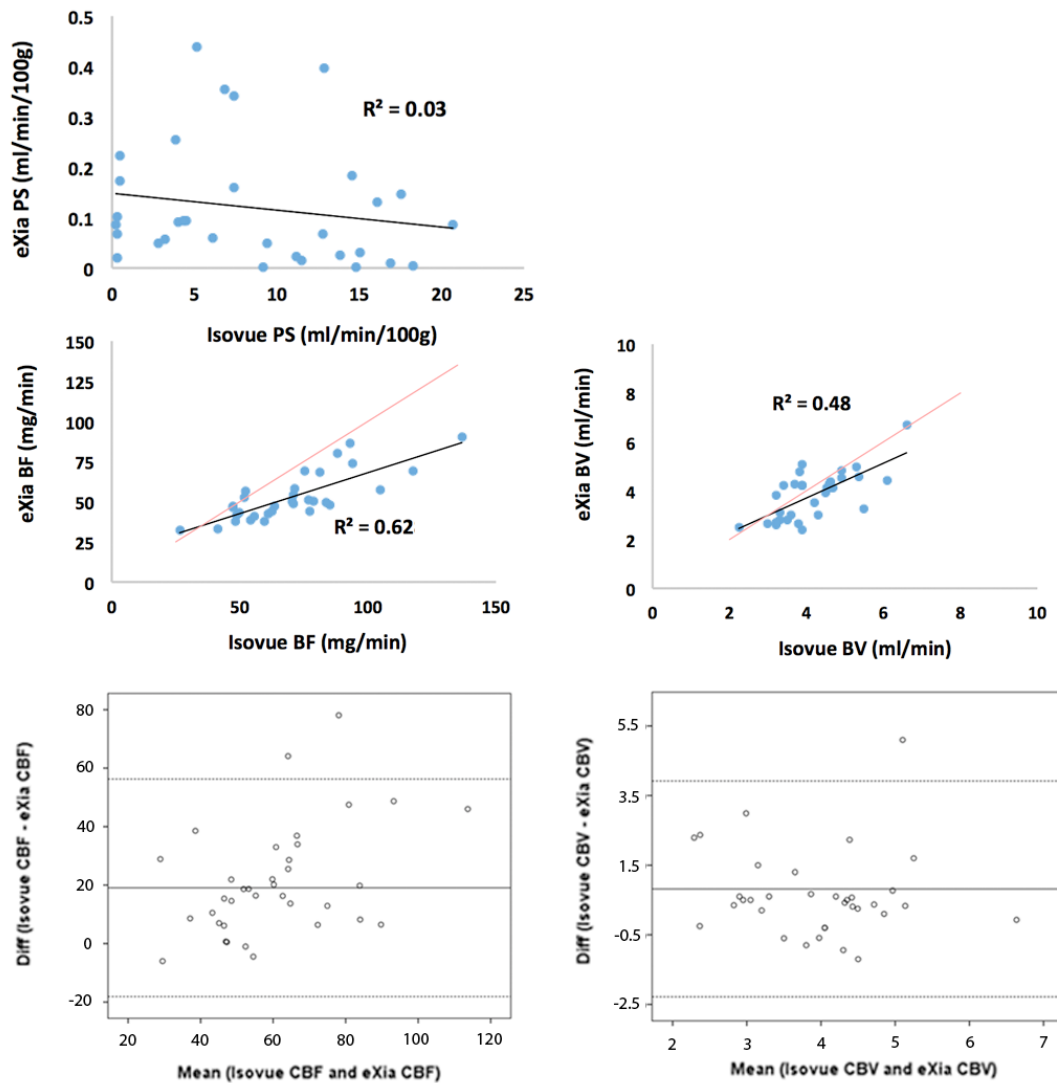


**Figure 3-7: Comparison of Isovue (760 Da) and eXia (65 kDa) permeability surface area product (PS) for all 10 subjects (top left). Comparison of cerebral blood flow (CBF) for all 10 subjects (middle left with an identity line (red)), cerebral blood volume (CBV) for all 10 subjects (middle right with an identity line (red)), and Bland Altman plots for agreement between Isovue and eXia measured CBF (bottom left), and CBV (bottom right) for all 10 subjects.**

This was an unexpected result as it contradicted results reported in previous pre-clinical studies. These studies can be grouped into those where the primary outcome was to

investigate tumor PS using imaging tracers, typically Gd-DTPA (29,31,32,33), or those that evaluate the delivery of chemotherapeutic drugs, and/or investigate its impact on clinical outcomes such as overall survival and tumor progression (28,30,32,34–36) following FUSwMB. When comparing FUS sonication studies that investigated tumor PS, using standard small molecule MRI imaging tracers, such as Gd-DTPA (molecular weight - 938 Da), it is important to note: 1) the time between tumor implant and sonication, in other words, the development stage of the tumor at the time of sonication, and 2) the time following sonication at which the follow-up PS and/or other perfusion parameters were measured. Details on these studies and their findings are summarized in Table 3-1.

**Table 3-1: Summary of pre-clinical studies that investigated tumor PS following focused ultrasound with microbubble administration (FUSwMB) (31,32,33).**

Author	Glioma Cell line (Rat)	Tumor Treatment Post Implant (days)	Results
<b>Chu et al, 2013 (31)</b>	C6 Glioma cells (Sprague Dawley rats)	10	- Increased accumulation with R1 (immediately following sonication)
		17	- Did not increase accumulation with R1 (immediately following sonication)
<b>Yang et al, 2014 (32)</b>	F98 Glioma cells (Fischer rats)	8	- $K_{trans}$ increased 2.46 times relative to untreated control (immediately following sonication) and 1.78 times relative to untreated control (24 h post sonication)
<b>Aryal et al, 2015 (33)</b>	9L Glioma cells (Fischer rats)	9	- $K_{trans}$ increased (immediately following sonication)
		14	- $K_{trans}$ did not change (immediately following sonication)
		17	- $K_{trans}$ did not change (immediately following sonication)

These studies indicated that in early stage tumors, defined as tumor treatment at between 8 to 10 days post-surgical implant (31,32,33), FUSwMB did result in an immediate increase in Gd-DTPA tumor PS, and it may remain increased at 24 h post, albeit less than the peak immediately following sonication. In later stage tumors, however, there was no change in Gd-DTPA tumor PS immediately following FUSwMB. None of the studies investigated the tumor PS response over 3 days following sonication for late stage tumors, particularly at 24 h post when we observed a significant decrease in Isovue tumor

PS. Yang et al did investigate the increase in PS at 24 hours post, but only for tumors treated at day 8 post implant, not for late stage tumors.

The sonication criteria for our study, which included a PS threshold of 1 ml/min/100g as high-grade tumor (42), resulted in sonication at 8 to 15 days post-surgical implant, highlighting the variability of tumor growth rates across different animals. To our knowledge, this study was the first that serially characterized the tumor PS response out to 3 days following FUSwMB. With our multiple time point studies, we showed that instead of increasing immediately following sonication, tumor Isovue PS gradually decreased up to 4 hours post sonication, and remains decreased at 24 hours post sonication. This observation was a previously unreported result.

VEGF induced angiogenic proliferation and associated PS increase are hallmarks of glioma progression (45). Analysis of the three studies in Table 3-1 indicated that newly formed or early stage brain tumors did demonstrate an immediate transient increase in tumor PS to small molecular contrast agent following FUSwMB, however, this increase was attenuated in more developed or late stage brain tumors. This suggests that beyond a certain point in tumor development, FUSwMB is unable to enhance the already elevated tumor PS to small molecules in glioma.

As brain tumor progresses, the elevated PS results in vasogenic edema and fluid accumulation which increase the interstitial fluid pressure (IFP) in and around the tumor leading to diminished transvascular pressure gradient required for convective delivery of solutes across the BTB (19,20,46,47). We hypothesize that the decrease in Isovue (760 Da) PS up to 3 days following FUSwMB should also decrease the elevated IFP, restoring the transvascular pressure gradient required for the delivery and accumulation of larger molecules, such as bevacizumab, across the BTB. In the recovery group, CT Perfusion was performed first with a much larger molecular weight contrast agent, eXia (65 kDa), followed by the standard small molecular weight agent, Isovue (760 Da), at each time point before and after FUSwMB. The results showed that there was a trend towards increased eXia PS at 24 h and 72 h post, indicating that large molecule PS did increase after a decrease in small molecular (Isovue) PS in the 24-72 hr period following

FUSwMB. Although neither of these PS increases were statistically significant, they support the plausibility of our hypothesis and suggest further study is warranted.

For both Isovue and eXia, CBF and CBV demonstrated an increasing trend at 24-h post FUSwMB, before returning to baseline levels by 72 h post, although these results were not significant. This finding, which is similar to outcomes seen with anti-angiogenic treatment (48–50), indicates that there was less edema and therefore, IFP, at 24-h post, allowing for a more ‘normalized’ perfusion across the tumor, further increasing drug delivery to and distribution throughout the tumor.

Plausible mechanisms for the decrease in PS to small molecules such as Isovue, following FUSwMB may include: 1) destruction from MB cavitation of the newly formed and highly permeable angiogenic vessels which have significantly less pericyte coverage, leaving the more ‘normal’ and mature blood vessels functionally intact, or 2) FUS stimulates microglia in and around the tumor vasculature, temporarily restoring BBB function. Angiogenic tumor blood vessels go through a maturation process over time. Immature vessels in glioblastoma exhibit sparse pericyte coverage, compared to normal mature blood vessels in the brain (51), rendering them more susceptible to destruction by FUSwMB, whereas mature vessels with more pericyte coverage are protected against FUSwMB. In late stage tumors with proportionally more mature vessels, destruction of immature vessels by FUSwMB would lead to a decrease in PS, whereas in early stage tumors, there is an overwhelming number of immature vessels - the destruction of which is more than offset by the increase in vessel (endothelial) permeability, resulting in a net increase in PS.

To test this hypothesis, rats in the recovery group were retrospectively grouped into the five lowest baseline PS (early stage), and those with the five highest baseline PS (late stage). We found that compared to baseline, the PS to small molecules for early stage tumors did not change at 24 h post, whereas in the late stage tumors, there was a significant decrease in PS at 24 h FUSwMB. This reinforces the conclusion that FUSwMB for developed or late stage tumors does not further elevate the PS, but instead may result in a decrease in PS following sonication. It has also been reported that reactive

astrogliosis is strongly correlated with glioma growth (52). Astrocytes become activated (proliferative), to varying degrees, in response to many CNS pathologies, including stroke, trauma, tumor growth, or neurodegenerative diseases (53,54). It is plausible that microglia in late stage tumors that demonstrate increased astrogliosis are stimulated by FUSwMB whereas those in early stage tumors are less affected in this respect.

These results pose three interesting questions concerning drug delivery across the BTB following FUSwMB: 1) what benefit is there in terms of drug delivery, if the PS to small molecules is decreasing, instead of increasing? 2) How does one explain results that demonstrated FUSwMB prior to chemotherapeutic administration improved both drug accumulation (28–30,33) and clinical outcomes such as reduction in tumor volume and survival (28,30,33–35); and 3) In brain tumors, where the PS may be significantly elevated relative to F, can PS be used to approximate FE which governs drug delivery across the BTB?

Before addressing these questions, it is important to understand the two underlying mechanisms by which drugs can cross the BTB: 1) diffusion, which is passive and dependent on concentration gradient across the barrier, and 2) convection, or bulk fluid flow carrying dissolved solute, across the barrier which is dependent on the hydrostatic pressure difference. A small molecule such as Isovue (760 Da) or Gd-DTPA (938 Da) has a relatively high diffusion coefficient; therefore its net flux is critically dependent on the diffusion coefficient before and after FUSwMB. Larger molecules, such as eXia (65 kDa) and other targeted drugs such as trastuzumab (34) or liposomal doxorubicin (33,35,36), with much lower diffusion coefficients are less able to passively diffuse across the BTB and their net flux is dependent more on the pressure gradient across the fenestrae within the BTB. Given this consideration, it is plausible that following FUSwMB, small molecule PS (which approximates FE, the volume transfer constant) is decreased relative to before treatment, whereas the PS of larger molecules that are unable to diffuse across the BTB could behave differently- increase because of the reduction in IFP. For these larger molecules, it is the difference in hydrostatic pressure that governs convective solute exchange before and after sonication.

It is also important to consider the growth stage of the tumor, since the microenvironment is different between early and late stage tumors, influencing the degree of diffusion and convection before and following FUSwMB. In early stage brain tumors, small but not large molecule PS is elevated as new highly permeable angiogenic blood vessels are being formed, meaning only small molecules that are able to diffuse across the BBB/BBB are delivered, whereas the delivery of larger molecules that rely on convection is limited due to the small fenestrae in the endothelium. In later stage tumors, with markedly increased PS from pore sizes as high as 12nm (55), bulk fluid flow allows for hydrostatic pressure dependent convective solute exchange, delivering both small and large molecules into the tumor.

Previous studies that demonstrated FUSwMB prior to chemotherapeutic administration improved both drug accumulation, and clinical outcomes, involved early stage tumors with small drugs such as Temozolomide - 194 Da (28,29) or BCNU - 214 Da (30), or larger molecules such as Trastuzumab – 145.5 kDa (34) or liposomal Doxorubicin - 80-90nm (33,35,36). Aryal et al found that liposomal doxorubicin delivery was significantly enhanced following FUSwMB, compared to an untreated control, regardless of the stage of tumor growth, whereas  $K_{trans}$  measured with Gd-DTPA (938 Da), was significantly elevated compared to controls treated at day 9, but not 14 and 17 (33). Our findings are in agreement with this result, demonstrating that for late stage tumors, FUSwMB may not increase small molecule PS, but instead allows for the increased delivery of larger molecules. In another study, Park et al found FUSwMB in combination with Trastuzumab, for six weekly treatments starting at 14 days following implant, resulted in better survival, with 4 out of 10 animals in which the tumor appeared to completely resolved (34). This study again highlights the potential for improved delivery, and therefore efficacy, for larger molecules following FUSwMB.

When eXia and Isovue permeability surface products are plotted against each other for all time-points, there is no correlation between them ( $R^2 = 0.03$ ). Because of its large size, baseline eXia PS ( $0.1 \pm 3.1$  ml/min/100g) is almost 100 times smaller than baseline Isovue PS ( $9.6 \pm 3.1$  ml/min/100g), decreasing its measurement accuracy. Interestingly, when the animals with the 5 lowest Isovue permeability at baseline were removed from

the analysis, a weak negative correlation appeared ( $R^2 = 0.15$ ), suggesting that eXia permeability measurements for early stage tumors are not reliable because of the lack of convection, or bulk fluid flow, across the BBB/BTB. For late stage and highly permeable tumors with larger fenestrae within the BTB to allow for convection, eXia permeability can be measured more reliably. The negative correlation confirms our hypothesis that as the Isovue PS decreases over three days following FUSwMB, eXia PS, and therefore the delivery of large molecules such as bevacizumab, should increase.

Although Isovue and eXia CBF were moderately correlated ( $R^2 = 0.63$ , slope = 0.51), they were not in agreement with each other, with Isovue CBF being higher than eXia CBF. Isovue and eXia CBV were also moderately correlated ( $R^2 = 0.48$ , slope = 0.71), but appeared to show better agreement than with CBF, with only 1 point outside of the 95% limits of agreement. Because of its much larger size than Isovue, it is plausible that the higher viscous drag increases the mean transit time (MTT) to cross the vasculature, resulting in an underestimation of eXia CBF.

A final point to address is whether PS, in practice, can be used to estimate FE which governs drug delivery across the BTB, especially for the current study. As discussed in Chapter 1, the volume transfer constant of solutes from blood to interstitial space is FE instead of PS. The relationship between FE and PS is given by the following equation:

$$FE = F \left( 1 - e^{-\frac{PS}{F}} \right) \quad \dots \text{Equation 3-3}$$

For the three regimes of exchange of solute between blood and interstitial space: 1) when  $PS \ll F$ , the exchange is diffusion-limited and PS approximates FE accurately; 2) when PS is of the same magnitude as F, the exchange is neither diffusion nor flow limited and to determine the volume transfer constant both F and PS have to be estimated; and 3) when  $PS \gg F$ , the exchange is flow-limited so that FE approaches F. Figure 3-8 plots the % error in using PS to approximate FE :

$$\frac{FE-PS}{FE} \times 100 = \left[ \frac{\ln(1-E)}{E} - 1 \right] \times 100 \quad \dots \text{Equation 3-4}$$

as PS is decreased relative to F.

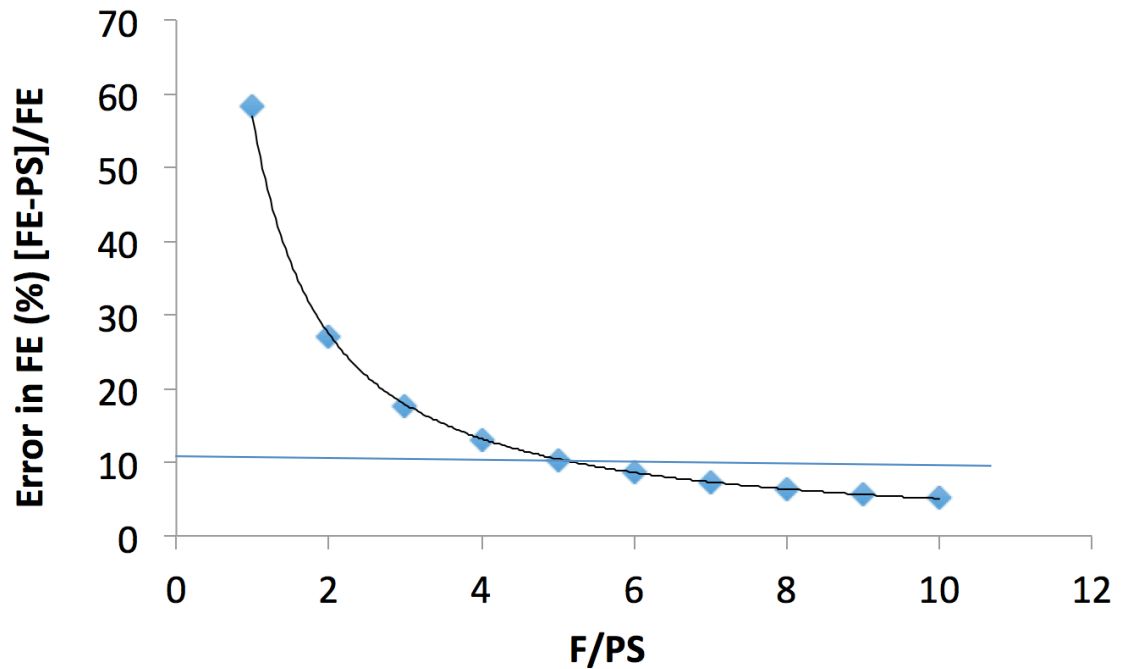


**Figure 3-8: The percent error in using permeability surface area product (PS) to approximate the flow extraction product (FE), as shown in Equation 3-4, plotted for different ratios of F/PS.**

When PS is at least 5 times smaller than F ( $F/PS > 5.0$ ), PS approximates FE to within 10%; if this condition is not true, the error in approximating FE by PS rapidly increases. However, in brain tumors, where the BTB PS is significantly elevated (42), this condition may not be met. In this study, we found that whereas Isovue PS was significantly lower at 24 h post, before returning to baseline at 72 h post; in contrast, the decrease in FE at 24 h post was not significant once the Bonferroni correction was applied, while FE at 72 h post remained significantly decreased compared to baseline. The BTB Isovue PS for 2 of the animals included in this study were on the threshold, suggesting that for such cases,

FE, which measures the volume transfer constant, would be the correct functional parameter to predict drug delivery across the BTB.

There are limitations of this study that need to be discussed. The first was that tumors at different stages of growth were used in comparing vascular response to FUSwMB. Previous studies in the literature standardized FUS treatment at a set number of days following implantation. From our experience, C6 glioma cells grew (developed) at different rates following implantation, therefore even with this standardization it was difficult to control the growth stage at which tumors were sonicated. We attempted to circumvent this problem by standardizing on tumor size (diameter) but PS remained difficult to control. The second limitation was the difficulty is using a large molecular weight CT contrast, eXia to evaluate BTB PS. Since large molecular weight agents have limited transport across the BTB, the signal-to-noise of the brain time density curve was poorer, leading to decreased reliability of their PS measurement when compared to smaller molecular weight agents. Our reasoning that there should be increased PS and accumulation of large molecular weight drugs, such as bevacizumab (149 kDa), is dependent on the decrease in edema and IFP following the decrease in small molecules (including water) PS from FUSwMB treatment. However, this study did not directly investigate edema. In chapter 4 of this thesis, we evaluate vasogenic edema by determining the extravascular contrast distribution volume ( $V_e$ ) following sonication, as well as using MRI to investigate the water content in and around the tumor.

Finally, there is evidence that the maximum delivery of NK cells across the BBB into tumors is achieved when the cells are injected just before the sonication (56,57), indicating the role of sonication in the delivery. Similarly, in study of Treat et al. (36), liposomal doxorubicin was injected prior to the sonications, and showed survival benefit with just one treatment of implanted tumors, In our current study, only the delivery of agents after the sonications was considered.

### 3.5 Conclusion

In this study, we used CT Perfusion derived tumor PS response to both small and large molecular weight CT contrast agents acutely over 4 hours and sub-acutely over 3 days to

investigate the delivery of molecules of different sizes across the BTB following FUSwMB. Instead of an immediate transient increase that was seen with the normal BBB, the tumor PS measured with standard small Isovue (760 Da) contrast agent, which was abnormally elevated at baseline because of the breakdown of the BBB in tumor vasculature, demonstrated a gradual decrease up to 4 h following sonication, and remained decreased at 24 h post, before returning to baseline levels at 72 h. This unexpected result could be explained by the physical destruction of newly formed and highly permeable angiogenic vessels which lack pericyte coverage and/or by the stimulation of microglia in and around the tumor vasculature, highlighting the potential for FUSwMB to manipulate the tumor vasculature and its microenvironment, beyond simply opening the BTB. Furthermore, the decrease in Isovue PS for up to 24-72 hrs following sonication may be accompanied by a decrease in edema, and IFP, thereby increasing large molecular PS and accumulation of larger chemotherapeutic agents, such as bevacizumab (149 kDa), that are unable to passively diffuse across the BTB and must rely on convective bulk solute flow. Future studies investigating enhanced delivery of small molecule drug to brain tumor using FUSwMB have to consider the tumor microenvironment, fenestra size in the BTB and mechanism of transport across the BTB for each drug.

### 3.6 References

1. Kreisl TN, Kim L, Moore K, Duic P, Royce C, Stroud I, et al. Phase II trial of single-agent bevacizumab followed by bevacizumab plus irinotecan at tumor progression in recurrent glioblastoma. *J Clin Oncol* [Internet]. 2009;27(5):740–5.
2. Friedman HS, Prados MD, Wen PY, Mikkelsen T, Schiff D, Abrey LE, et al. Bevacizumab alone and in combination with irinotecan in recurrent glioblastoma. *J Clin Oncol*. 2009;27(28):4733–40.
3. Gilbert MR, Dignam JJ, Armstrong TS, Wefel JS, Blumenthal DT, Vogelbaum M a, et al. A randomized trial of bevacizumab for newly diagnosed glioblastoma. *N Engl J Med* [Internet]. 2014;370(8):699–708.

4. Chinot OL, Wick W, Mason W, Henriksson R, Saran F, Nishikawa R, et al. Bevacizumab plus radiotherapy-temozolomide for newly diagnosed glioblastoma. *N Engl J Med* [Internet]. 2014;370(8):709–22.
5. Grossman S, Wharam M, Sheidler V, Kleinberg L, Zeltzman M, Yue N, et al. Phase II study of continuous infusion carmustine and cisplatin followed by cranial irradiation in adults with newly diagnosed high-grade astrocytoma. *J Clin Oncol*. 1997;15(7).
6. Liu HL, Fan CH, Ting CY, Yeh CK. Combining microbubbles and ultrasound for drug delivery to brain tumors: Current progress and overview. *Theranostics*. 2014;4(4):432–44.
7. Jain RK, di Tomaso E, Duda DG, Loeffler JS, Sorensen a G, Batchelor TT. Angiogenesis in brain tumours. *Nat Rev Neurosci*. 2007;8(8):610–22.
8. Reardon D a, Rich JN, Friedman HS, Bigner DD. Recent advances in the treatment of malignant astrocytoma. *J Clin Oncol* [Internet]. 2006;24(8):1253–65.
9. Burger PC, Vogel FS, Green SB, Strike TA. Glioblastoma Multiforme and Anaplastic Astrocytoma. *Cancer* [Internet]. 1985;56:1106–11.
10. Neuwelt EA, Frenkel EP, D'Agostino A. Growth of Human Lung Tumor in the Brain of the Nude Rat as a Model to Evaluate Antitumor Agent Delivery across the Blood-Brain Barrier. *Cancer Res* [Internet]. 1985;2827–33.
11. Neuwelt EA, Barnett P a, Bigner DD, Frenkel EP. Effects of adrenal cortical steroids and osmotic blood-brain barrier opening on methotrexate delivery to gliomas in the rodent: the factor of the blood-brain barrier. *Proc Natl Acad Sci* [Internet]. 1982;79(14):4420–3.
12. Claes A, Idema AJ, Wesseling P. Diffuse glioma growth: A guerilla war. *Acta Neuropathologica*. 2007. p. 443–58.

13. Keime-Guibert F, Chinot O, Taillandier L, Cartalat-Carel S, Frenay M, Kantor G, et al. Radiotherapy for glioblastoma in the elderly. *N Engl J Med* [Internet]. 2007;356(15):1527–35.
14. Lang FF, Gilbert MR. Diffusely infiltrative low-grade gliomas in adults. *Journal of Clinical Oncology*. 2006. p. 1236–45.
15. Palmer AM. The role of the blood-CNS barrier in CNS disorders and their treatment. *Neurobiol Dis* [Internet]. Elsevier Inc.; 2010;37(1):3–12.
16. Papadopoulos MC, Saadoun S, Binder DK, Manley GT, Krishna S, Verkman a. S. Molecular mechanisms of brain tumor edema. *Neuroscience*. 2004;129(4):1011–20.
17. Strugar J, Rothbart D, Harrington W, Criscuolo GR. Vascular permeability factor in brain metastases: correlation with vasogenic brain edema and tumor angiogenesis. *J Neurosurg* [Internet]. 1994;81(4):560–6.
18. Baxter LT, Jain RK. Transport of fluid and macromolecules in tumors. I. Role of interstitial pressure and convection. *Microvasc Res*. 1989;37(1):77–104.
19. Netti PA, Baxter LT, Boucher Y, Skalak R, Jain RK. Time-dependent behavior of interstitial fluid pressure in solid tumors: Implications for drug delivery. *Cancer Res*. 1995;55(22):5451–8.
20. Chauhan VP, Stylianopoulos T, Boucher Y, Jain RK. Delivery of Molecular and Nanoscale Medicine to Tumors: Transport Barriers and Strategies. *Annu Rev Chem Biomol Eng*. 2011;2(1):281–98.
21. Jain RK. Vascular and interstitial barriers to delivery of therapeutic agents in tumors. *Cancer Metastasis Rev*. 1990;9(3):253–66.
22. Liu Z, Zhao X, Mao H, Baxter P a., Huang Y, Yu L, et al. Intravenous injection of oncolytic picornavirus SVV-001 prolongs animal survival in a panel of primary

- tumor-based orthotopic xenograft mouse models of pediatric glioma. *Neuro Oncol.* 2013;15(9):1173–85.
23. Bhujbal S V., de Vos P, Niclou SP. Drug and cell encapsulation: Alternative delivery options for the treatment of malignant brain tumors. *Adv Drug Deliv Rev* [Internet]. 2014;67-68:142–53.
  24. Barua NU, Gill SS, Love S. Convection-enhanced drug delivery to the brain: Therapeutic potential and neuropathological considerations. *Brain Pathol.* 2014;24:117–27.
  25. Van Woensel M, Wauthoz N, Rosière R, Amighi K, Mathieu V, Lefranc F, et al. Formulations for Intranasal Delivery of Pharmacological Agents to Combat Brain Disease: A New Opportunity to Tackle GBM? *Cancers (Basel)* [Internet]. 2013;5(3):1020–48.
  26. Deeken JF, Löscher W. The blood-brain barrier and cancer: transporters, treatment, and Trojan horses. *Clin Cancer Res* [Internet]. 2007;13(6):1663–74.
  27. Madsen SJ, Hirschberg H. Site-specific opening of the blood-brain barrier. *J Biophotonics.* 2010;3(5-6):356–67.
  28. Wei KC, Chu PC, Wang HYJ, Huang CY, Chen PY, Tsai HC, et al. Focused Ultrasound-Induced Blood-Brain Barrier Opening to Enhance Temozolomide Delivery for Glioblastoma Treatment: A Preclinical Study. *PLoS One.* 2013;8(3):1–10.
  29. Liu H-L, Huang C-Y, Chen J-Y, Wang H-YJ, Chen P-Y, Wei K-C. Pharmacodynamic and Therapeutic Investigation of Focused Ultrasound-Induced Blood-Brain Barrier Opening for Enhanced Temozolomide Delivery in Glioma Treatment. *PLoS One* [Internet]. 2014;9(12):e114311.
  30. Liu H-L, Hua M-Y, Chen P-Y, Chu P-C, Pan C-H, Yang H-W, et al. Blood-brain barrier disruption with focused ultrasound enhances delivery of chemotherapeutic drugs for glioblastoma treatment. *Radiology.* 2010;255(2):415–25.

31. Chu PC, Chai WY, Hsieh HY, Wang JJ, Wey SP, Huang CY, et al. Pharmacodynamic analysis of magnetic resonance imaging-monitored focused ultrasound-induced blood-brain barrier opening for drug delivery to brain tumors. *Biomed Res Int*. 2013;2013.
32. Yang FY, Ko CE, Huang SY, Chung IF, Chen GS. Pharmacokinetic changes induced by focused ultrasound in glioma-bearing rats as measured by dynamic contrast-enhanced MRI. *PLoS One*. 2014;9(3).
33. Aryal M, Park J, Vykhodtseva N, Zhang Y-Z, McDannold N. Enhancement in blood-tumor barrier permeability and delivery of liposomal doxorubicin using focused ultrasound and microbubbles: evaluation during tumor progression in a rat glioma model. *Phys Med Biol* [Internet]. IOP Publishing; 2015;60(6):2511–27.
34. Park EJ, Zhang YZ, Vykhodtseva N, McDannold N. Ultrasound-mediated blood-brain/blood-tumor barrier disruption improves outcomes with trastuzumab in a breast cancer brain metastasis model. *J Control Release*. 2012;163(3):277–84.
35. Aryal M, Vykhodtseva N, Zhang YZ, Park J, McDannold N. Multiple treatments with liposomal doxorubicin and ultrasound-induced disruption of blood-tumor and blood-brain barriers improve outcomes in a rat glioma model. *J Control Release* [Internet]. Elsevier B.V.; 2013;169(1-2):103–11.
36. Treat LH, McDannold N, Zhang Y, Vykhodtseva N, Hynynen K. Improved Anti-Tumor Effect of Liposomal Doxorubicin After Targeted Blood-Brain Barrier Disruption by MRI-Guided Focused Ultrasound in Rat Glioma. *Ultrasound Med Biol*. 2012;38(10):1716–25.
37. Goertz DE, Wright C, Hynynen K. Contrast agent kinetics in the rabbit brain during exposure to therapeutic ultrasound. *Ultrasound Med Biol*. 2010;36(6):916–24.
38. Lee T-Y, Purdie TG, Stewart E. CT imaging of angiogenesis. *Q J Nucl Med*. 2003;47(3):171–87.

39. St Lawrence KS, Lee TY. An adiabatic approximation to the tissue homogeneity model for water exchange in the brain: II. Experimental validation. *J Cereb Blood Flow Metab.* 1998;18(12):1378–85.
40. Crone C. The Permeability of Capillaries in Various Organs as Determined by Use of the Indicator Diffusion Method. *Acta Physiol Scand.* 1963;58(4):292–305.
41. Tofts PS, Brix G, Buckley DL, Evelhoch JL, Henderson E, Knopp M V., et al. Estimating kinetic parameters from dynamic contrast-enhanced T1- weighted MRI of a diffusable tracer: Standardized quantities and symbols. *Journal of Magnetic Resonance Imaging.* 1999. p. 223–32.
42. Jain R, Narang J, Griffith B, Bagher-Ebadian H, Scarpace L, Mikkelsen T, et al. Prognostic Vascular Imaging Biomarkers in High-Grade Gliomas. Tumor Permeability as an Adjunct to Blood Volume Estimates. *Acad Radiol.* 2013;20(4):478–85.
43. Jain R. Perfusion CT imaging of brain tumors: an overview. *AJNR Am J Neuroradiol [Internet].* 2011;32(9):1570–7.
44. Bland JM, Altman DG. Statistical methods for assessing agreement between two methods of clinical measurement. *Lancet [Internet].* 1986;327(8476):307–10.
45. Monsky WL, Carreira CM, Tsuzuki Y, Gohongi T, Fukumura D, Jain RK. Role of host microenvironment in angiogenesis and microvascular functions in human breast cancer xenografts: Mammary fat pad versus cranial tumors. *Clin Cancer Res.* 2002;8(4):1008–13.
46. Jain RK. Barriers to drug delivery in solid tumor. Jain, R. K. (1994). Barriers to drug delivery in solid tumors. *Scientific American*, 271(1), 58-65. Retrieved from <http://www.ncbi.nlm.nih.gov/pubmed/8066425>tumors. *Sci Am [Internet].* 1994;271(1):58–65.

47. Yuan F, Salehi HA, Boucher Y, Vasthare US, Tuma RF, Jain RK. Vascular permeability and microcirculation of gliomas and mammary carcinomas transplanted in rat and mouse cranial windows. *Cancer Res.* 1994;54(17):4564–8.
48. Tong RT, Boucher Y, Kozin S V., Winkler F, Hicklin DJ, Jain RK. Vascular normalization by vascular endothelial growth factor receptor 2 blockade induces a pressure gradient across the vasculature and improves drug penetration in tumors. *Cancer Res.* 2004;64(11):3731–6.
49. Jain RK. Normalizing tumor microenvironment to treat cancer: bench to bedside to biomarkers. *J Clin Oncol.* 2013;31(17):2205–18.
50. Jain RK, Tong RT, Munn LL. Effect of vascular normalization by antiangiogenic therapy on interstitial hypertension, peritumor edema, and lymphatic metastasis: Insights from a mathematical model. *Cancer Res.* 2007;67(6):2729–35.
51. Bergers G, Song S. The role of pericytes in blood-vessel formation and maintenance. *Neuro Oncol.* 2005;7(4):452–64.
52. O’Brien ER, Howarth C, Sibson NR. The role of astrocytes in CNS tumors: pre-clinical models and novel imaging approaches. *Front Cell Neurosci* [Internet]. 2013;7(April):40.
53. Pekny M, Nilsson M. Astrocyte activation and reactive gliosis. *Glia.* 2005;50(4):427–34.
54. Pekny M, Wilhelmsson U, Pekna M. The dual role of astrocyte activation and reactive gliosis. *Neuroscience Letters.* 2014. p. 30–8.
55. Sarin H, Kanevsky AS, Wu H, Sousa AA, Wilson CM, Aronova MA, et al. Physiologic upper limit of pore size in the blood-tumor barrier of malignant solid tumors. *J Transl Med.* 2009;7:51.

56. Alkins R, Burgess A, Ganguly M, Francia G, Kerbel R, Wels WS, et al. Focused ultrasound delivers targeted immune cells to metastatic brain tumors. *Cancer Res.* 2013;73(6):1892–9.
57. Alkins R, Burgess A, Kerbel R, Wels WS, Hynynen K. Early treatment of HER2-amplified brain tumors with targeted NK-92 cells and focused ultrasound improves survival. *Neuro Oncol.* 2016;18(7):974–81.

## Chapter 4

### 4 Investigating the Decrease in Edema following Focused Ultrasound Sonication with Microbubble Administration using Magnetic Resonance Imaging and CT Perfusion Derived Extravascular Distribution Volume in a C6 Rat Glioma Model

#### 4.1 Introduction

One of the hallmarks of Glioblastoma (GBM) progression is the loss of blood-brain-barrier (BBB) integrity, leading to a permeable blood-tumor-barrier (BTB), accompanied by other pathological features - including marked angiogenesis with endothelial proliferation, severe hypoxia, and tumor necrosis (1–3). As a result, GBM vessels are tortuous, disorganized, and highly permeable, with abnormalities in the endothelial wall, pericyte coverage, and the basement membrane (4–7).

The loss of BBB function results in the increased accumulation of fluid and plasma proteins peri-tumorally, and in the surrounding brain (8), leading to vasogenic edema, which by itself is a major cause of morbidity in brain tumors (9). Due to the lack of a lymphatic drainage system in the solid tumor mass, vasogenic edema results in an abnormal increase in interstitial fluid pressure (IFP), which creates a barrier for drug delivery, by diminishing the transvascular pressure gradient required for convective transport across the BTB barrier (10).

At present, steroid is the only treatment for controlling vasogenic brain edema, but with moderate efficacy and many side-effects (11). Recent pre-clinical and clinical studies have demonstrated that anti-angiogenic or anti-permeabilizing agents, such as bevacizumab or cediranib, may alleviate vasogenic brain edema by ‘normalizing’ the vasculature, creating a window of decreased permeability, and therefore decreased IFP, improving perfusion and drug delivery, particularly for large molecules that rely on pressure-dependent convective solute exchange across the BTB (8,12,13). Clinical studies also demonstrated that when anti-angiogenic agents are combined with

chemotherapy, they confer a synergistic beneficial effect for brain tumor treatment (14,15).

In Chapter 3 of this thesis, we uncovered a decrease in endothelial permeability surface product (PS) response, as measured with a standard small molecule CT contrast agent, Isovue, out to 24 h following FUS sonication with MB administration (FUSwMB) in a C6 rat glioma model. We hypothesized that the observed decrease in endothelial permeability surface response should also be accompanied by a decrease in vasogenic edema, thereby decreasing the elevated IFP, restoring the transvascular pressure gradient required for convective fluid flux driven drug delivery across the BTB. In addition to improving drug delivery for larger drugs that are reliant on convective solute flux across the BTB, the potential to ‘normalize’ IFP using FUSwMB can be seen as a novel approach to alleviate the symptoms associated with vasogenic edema in brain tumors.

The decrease in endothelial PS to small molecules of the tumor vasculature following FUSwMB was an unexpected and previously unreported result except for our publication. The exact mechanism for the transient restoration in BBB function is unclear, and could be explained by one of two following hypothesis: 1) Physical destruction of the newly formed and highly permeable angiogenic vessels, specifically those that lack pericyte coverage, leaving the more pericyte covered blood vessels intact, or 2) FUSwMB activates microglia in and around the tumor vasculature, temporarily restoring BBB function. Regardless of its mechanism, the decrease in edema is an important favorable response in the treatment of brain tumors.

Although directly quantifying edema is difficult, the combination of dynamic imaging and tracer kinetic modeling have previously been used to calculate surrogate measures of edema, often with radioactive water-based tracers or with perfusion MRI (16,17). In a standard two-compartment model, the extravascular distribution volume ( $V_e$ ) is defined as the ratio of the forward volume transfer of contrast from plasma to tissue,  $K_{trans}$ , to the back flux rate constant from tissue to plasma,  $K_{ep}$ . In a distributed parameter model, such as the Johnson-Wilson and Lee model (18),  $V_e$  can be derived from the flow scaled impulse residue function,  $R(t)$ , as the ratio of the flow-extraction product (FE) to the

backflux rate constant of extravasated contrast into the vascular space,  $k_2$ . The use of a diffusible tracer that mimics water exchange across the BTB gives greater confidence that the measured tracer parameters can be used as a surrogate of edematous fluid distribution (19).

Isovue is a diffusible CT contrast agent that is commonly used to quantify various perfusion parameters, such as PS, cerebral blood flow and cerebral blood volume, but can also be used to calculate the extravascular contrast distribution volume,  $V_e$ . Therefore, the purpose of this study is to use CT Perfusion or dynamic contrast-enhanced computed tomography (DCE-CT), corroborated by MRI T1 mapping and T2 fluid attenuation inverse recovery (FLAIR) imaging, to quantitatively evaluate the decrease in vasogenic edema following FUSwMB, and to use histology and immunohistochemical staining to investigate the mechanisms responsible for this decrease in a C6 rat glioma model.

## 4.2 Methods and Materials

### 4.2.1 Animal Groups

All experiments were approved by the Animal Use Subcommittee of the Canadian Council on Animal Care at our institution. Seventeen male Wistar rats (300-450g) were used in this study. For each rat,  $1 \times 10^6$  C6 glioma cells were surgically implanted into the right striatum of the brain, using a stereotactic frame, with coordinates 3 mm to the right, and 1 mm posterior to the center of the bregma, along the coronal suture. Follow-up CT Perfusion scanning was performed at day 7 post implant, and every 2 days after that, until the following criteria were met: 1) the tumor was greater than 3 mm in diameter, measured using the average CT map (derived by averaging all images of the same slice in the CT Perfusion study), and 2) the tumor PS was greater than 1 ml/min/100g, typically at 8-15 days after implantation at which time the tumors underwent FUSwMB. Prior to sonication, anesthesia was induced by breathing 2.5% isoflurane from a nose cone, before the head was shaved and depilated, and a tail vein catheter was inserted. Ketamine-xylazine (10:1) was then administered at a rate of 5-10 ml/hr via the tail vein catheter as isoflurane was turned off. A baseline CT Perfusion scan was performed 20 minutes after switching the isoflurane off, after which the rat was placed on the FUS system inside the

CT gantry and the tumor was FUS sonicated under CT image guidance. The animals were divided into 2 groups: 1) An imaging group to evaluate changes in extravascular distribution volume ( $V_e$ ), for which CT Perfusion was performed at baseline, 24, and 72 h post (n=10), and included a subgroup that underwent MRI at each time point (n=4), and 2) a histopathology group to investigate histological changes in the vasculature before and after FUSwMB (n=7) which consisted of a subgroup that was sacrificed following baseline imaging without FUSwMB (n=3) and a subgroup that underwent FUSwMB and was sacrificed after follow-up imaging at 24 hours (n=4).

#### 4.2.2 Focused Ultrasound Sonication and Microbubble Administration

The rat was placed supine on the FUS system (FUS Instruments Inc., Toronto, Canada) and was carefully positioned for optimal trans-cranial sonication, with the ultrasound (US) transducer placed orthogonally to the surface of the rat's head. Before the placement of the transducer, a layer of ultrasound gel was placed on the surface of the skull to allow for smooth US transmission from water in the FUS system to the scalp. A schematic of the experimental setup is shown in Figure 3-1. With the rat on the FUS system, an axial CT scan (140 kVp, 200 mA, 1s rotation time, 2.5 mm slice thickness) was performed to locate the brain followed by a baseline CT Perfusion study (see below for details) to locate the center of the tumor. These coordinates were then input into the FUS system to target the tumor center. All sonications were pulsed at 1 Hz, 0.5 W and a 10 ms burst length (1 % duty cycle) for 120 s. A single bolus of Definity (Lantheus Medical Imaging, USA) microbubbles in 1:10 saline dilution at a dose of 20  $\mu$ l/kg was manually injected via the vein catheter simultaneous with the start of sonication.

#### 4.2.3 CT Perfusion Study Protocol

To quantitatively evaluate the BBB PS and other CT Perfusion derived parameters including the extravascular contrast distribution volume ( $V_e$ ), a two-phase scanning protocol was used (First phase: two images per second acquired continuously for 30s using 80 kV, 250 mA, 0.5s rotation time, 2.5 mm slice thickness; Second phase: one image acquired every 15s for another 180 seconds using the same scanning parameters).

A 2.5 ml/kg bolus of 300 mg Iodine/ml (Isovue-300, 760 Da molecular weight) was intravenously infused via the tail vein catheter over 5 seconds at the start of the first phase.

#### 4.2.4 Tracer Kinetic Modeling

The Johnson-Wilson-Lee (JWL) distributed parameter model (20,21), was used to model the distribution of injected contrast in the brain (tumor) using PS, cerebral blood flow (CBF) and cerebral blood volume (CBV) as the model parameters. The technique is explained in detail in Chapter 1 (section 1.9.4) of this thesis. One internal carotid artery was identified in the CT Perfusion images and a 2 x 2 pixel region was placed in the artery to generate the arterial time-density curve which was background subtracted to generate the arterial time-enhancement curve or the arterial input function,  $C_a(t)$  to JWL model. A typical arterial and the tumor time density curve from a rat study are shown in Figure 3-2.

Under the assumption that brain blood flow (F or CBF) is constant and CT measured signal in artery and brain is linear with respect to the concentration of contrast, the brain time-enhancement curve,  $Q(t)$  is the product of F and the convolution of the arterial input function and the impulse residue function  $R(t)$ , as shown in Equations 4-1 and 4-2.

$$Q(t) = F \cdot [C_a(t) * R(t - T_0)] \quad \dots \text{Equation 4-1}$$

$$R(t) = \begin{cases} 1, & 0 < t \leq \frac{V_b}{F} \\ E e^{-\frac{FE}{V_e}(t - \frac{V_b}{F})} H(t - \frac{V_b}{F}), & t > \frac{V_b}{F} \end{cases} \quad \dots \text{Equation 4-2}$$

where  $T_0$  is the appearance time of contrast agent in the brain relative to that in the input artery,  $V_b$  (or CBV) is the volume of ‘flowing’ blood that is in large vessels, arterioles, capillaries, venules, and veins,  $V_e$  is the contrast distribution volume in the extravascular space,  $E = 1 - e^{-\frac{PS}{F}}$  is the extraction fraction, or the fraction of contrast (mass) that is

transferred from the vascular to extravascular space during a single passage of blood from the arteriole end to the venous end of the capillaries in tissue (40), and  $H$  is the unit step function. As shown in Equation 4-2,  $R(t)$  of the JWL model is parameterized by  $F$  (or CBF),  $PS$ ,  $V_b$  (or CBV), and  $V_e$ . CT Perfusion 5 (a prototype of CT Perfusion 4D, GE Healthcare, Waukesha, Wis) was used to estimate and generate parametric maps of  $PS$ , CBF, CBV and  $V_e$ , by iteratively changing their values until an optimal fit to  $Q(t)$  is reached according to Equations 4-1 and 4-2 for each voxel.

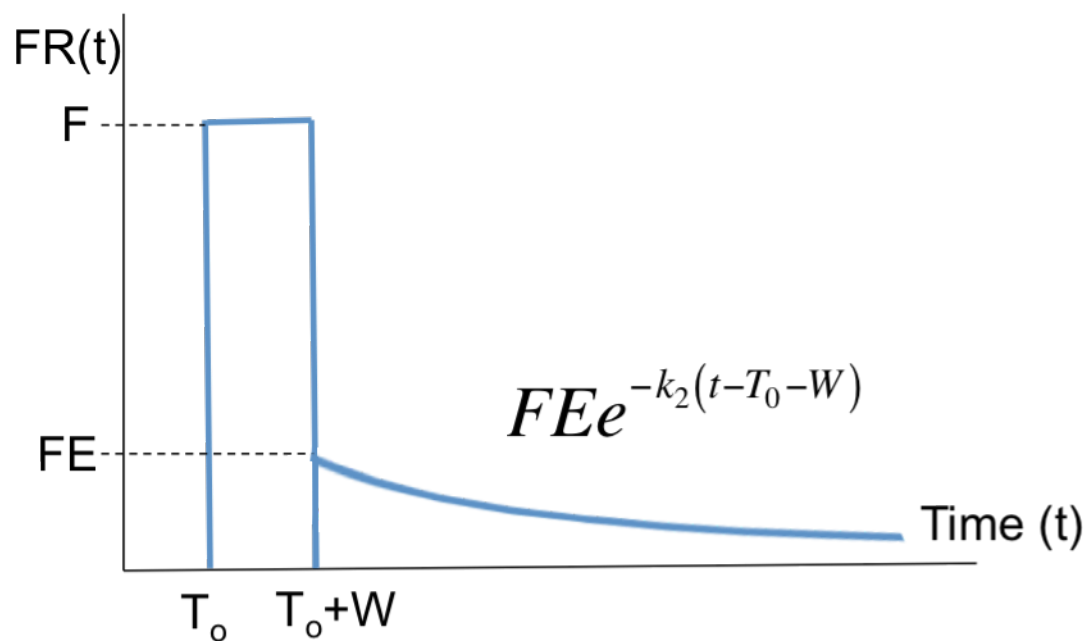


**Figure 4-1: A schematic diagram for the blood flow ( $F$ ) scaled impulse residue function,  $R(t)$ , where  $E$  is extraction efficiency,  $T_0$  is the time for the contrast to appear,  $W$  is the mean transit time, and  $k_2$  is the rate constant that defines transfer from the interstitial space back into the vasculature.**

#### 4.2.5 Magnetic Resonance Imaging

A subgroup of the imaging group underwent MRI (3T Biograph mMR, Siemens Healthcare) immediately prior to CT Perfusion at baseline, 24-h, and 72-h post sonication, to image fluid accumulation surrounding the tumor. An axial T2-FLAIR

sequence (TI = 2500 ms, TE/TR = 94ms/9000ms, slice thickness = 3 mm, NEX = 4, 256 x 256, FOV = 70mm) and a dual flip angle quantitative longitudinal relaxation time (T1) sequence (TR/TE = 15ms/3.31ms, flip angle 1 = 5°, flip angle 2 = 26°, slice thickness = 3.00mm, NEX = 6, 256 x 256, FOX = 70 mm) were used to evaluate edema. T1 was calculated using the MAPIT software package (Siemens, Erlangen Germany).

#### 4.2.6 Imaging Analysis of CT Perfusion and MRI Study

PS, CBF, and CBV map from the CT Perfusion study were used to delineate the tumor. A PS of over 1 ml/min/100g was used as the threshold for the tumor margin, as this value has previously been measured in high-grade brain tumors (22). Increased tumor CBF and CBV threshold of 1.5x relative to the contralateral hemisphere were also used to guide delineation of the tumor rim (23). The tumor ROI for each time point was delineated manually using the above thresholds on the corresponding PS, CBF and CBV map and used to calculate the mean tumor values. For MR image analysis, the T2- FLAIR image and T1 map were used to manually delineate the edematous ROI, which included tumor and peri-tumor space, at each time point.

#### 4.2.7 Calculation of Extravascular Distribution Volume

The time-density curve from the tumor ROI after background subtraction,  $Q(t)$ , was deconvolved with the corresponding arterial input function,  $C_a(t)$ , to estimate PS, CBF, CBV and  $V_e$ , by iteratively changing their values until an optimal fit to  $Q(t)$  is reached according to Equations 4-1 and 4-2. Once the model fit is found, the parameters can be used to calculate the extravascular distribution volume,  $V_e$ :

$$V_e = \frac{FE}{k_2} \quad \dots \text{Equation 4-3}$$

where  $k_2$  is the backflux constant from interstitial space to intravascular space. A schematic diagram of the flow scaled  $R(t)$  for the JW model is shown in Figure 4-1.

#### 4.2.8 Immunohistochemistry

For the histopathology analysis group, the animals were euthanized either prior to FUSwMB (n=3), or at 24-h post (n=4). Once euthanized, the animals were immediately perfusion-fixed with a phosphate buffered saline solution, followed by 4% paraformaldehyde. The brains were removed and fixed in 10% formalin for 24 hours, before they were cut into 3 mm thick blocks, paraffin-embedded, then sectioned at 5  $\mu$ m. The sections were stained with monoclonal anti-CD31 antibodies (1:50, Acris Antibodies) for endothelial cells, as a marker for endothelial proliferation and angiogenesis, and anti- vimentin antibodies (1:100, Abcam), as a marker for pericyte expression (24), or glial activation (25). Light microscopy was used to evaluate CD31 and vimentin expression. For CD31 analysis, the total number of intact and collapsed CD31 positive blood vessels, in 5 separate fields (20x) of the most vascular region of the tumor was recorded. Intact vessels were defined as having a CD31 stained rim around a blood vessel, whereas collapsed vessels were defined as circular regions with condensed CD31 expression in the center (26). For vimentin analysis, the average tumor staining density was scored as 1 (light – limited to single pericytes or glial cells), 2 (moderate – the appearance of light streaks/filament structures), and 3 (heavy – appearance of multiple heavy streak/filament structures) (27).

#### 4.2.9 Statistical Analysis

The differences in CT Perfusion and MRI parameters between time points were assessed using Mann-Whitney U Tests, with Bonferroni correction applied to account for 3 repeated measures (m=3), comparing baseline with 24 h and 72 h and 24 h with 72 h. Regression analysis was used to investigate the correlation between T2-FLAIR image signal intensity and quantitative T1 derived measures of edema with  $V_e$ , as measured by CT Perfusion at all time points. For immunohistochemical analysis, differences in the number of intact and collapsed CD31 vessels and vimentin scores between the sonicated and control groups were assessed using non-parametric t-tests. Statistical significance was determined as  $P < 0.05$ . All statistical analysis was performed with IBM SPSS v23.

### 4.3 Results

Tumor CBF, CBV,  $V_e$  and Isovuc PS over time (n=10) out to 72 hours following FUSwMB is shown in Figure 4-2. Tumor Isovuc PS was significantly lower at 24 h post ( $6.3 \pm 4.3$  ml/min/100g;  $P < 0.01$ , significant after Bonferroni correction) compared to baseline ( $9.6 \pm 6.6$  ml/min/100g), but not compared to 72 h post sonication ( $8.1 \pm 5.2$  ml/min/100g;  $P = 0.08$ ). Similarly,  $V_e$  was significantly lower at 24 h post sonication ( $31 \pm 22$  ml/100g;  $P < 0.005$ , significant after Bonferroni correction), when compared to baseline ( $39 \pm 26$  ml/100g), but not compared to 72 h post sonication ( $35 \pm 24$  ml/100g,  $P = 0.2$ ). Both CBF and CBV were higher at 24 h post ( $75 \pm 30$  mL/min/100g and  $4.4 \pm 1.3$  mL/100g; both  $P < 0.03$  not significant after Bonferroni correction) compared to baseline ( $62 \pm 19$  mL/min/1000g and  $3.8 \pm 0.8$  mL/100g), but not compared to 72 h post sonication ( $69 \pm 26$  mL/min/100g,  $P = 0.07$  and  $3.9 \pm 1.0$  mL/100g;  $P = 0.2$ , respectively).

Tumor T1 and T2-FLAIR SI over time for the subgroup that underwent MRI (n=4) in addition to CT Perfusion imaging is shown in Figure 4-3. The tumor T1 was lower at 24 h post ( $1753 \pm 153$  ms;  $P < 0.05$  but not significant after Bonferroni correction) compared to baseline ( $1807 \pm 184$  ms) but not compared to 72 h post sonication ( $1847 \pm 253$  ms;  $P = 0.2$ ). There were no significant changes in T2-FLAIR SI at 24 h post ( $662 \pm 61$ ;  $P = 0.2$ ) or 72 h post ( $704 \pm 192$ ;  $P = 0.4$ ), compared to baseline ( $688 \pm 95$ ).

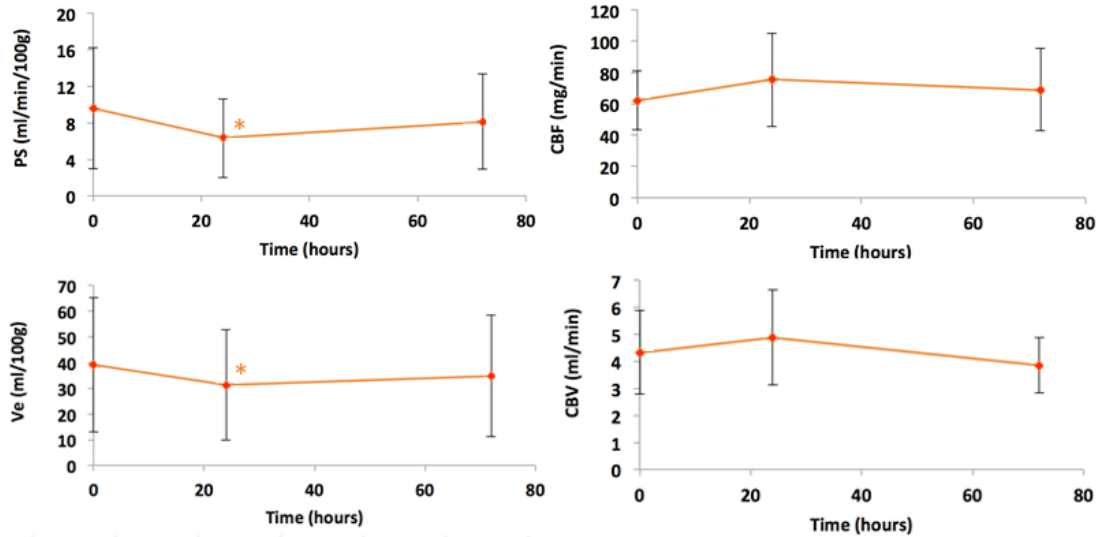


**Figure 4-2: Serial tumor PS, extravascular contrast distribution volume (Ve), cerebral blood flow (CBF), and cerebral blood volume (CBV), measured using Isovue (760 Da) contrast agent, out to 72 hours following FUSwMB (n=10). \*Significantly different from baseline value as determined by Bonferroni corrected non-parametric t-tests.**

CT Perfusion derived PS maps, MRI T1 maps and T2-FLAIR images for a rat before and after FUSwMB are shown in Figure 4-4. When compared with  $V_e$ , both the T1 ( $R^2 = 0.52$ ,  $m = 5.4$ ;  $P < 0.02$ ) and the FLAIR SI ( $R^2 = 0.85$ ,  $m = 4.9$ ;  $P < 0.005$ ) showed moderate to strong correlations as shown in Figure 4-5.

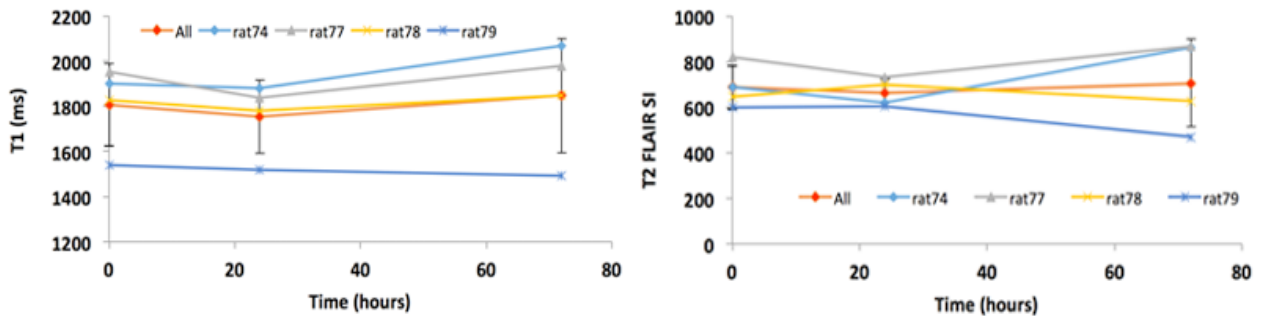


**Figure 4-3: Serial tumor longitudinal relaxation time (T1) and fluid attenuated inversion recovery (FLAIR) signal intensity (SI) out to 72 hours following FUSwMB (n=4).**

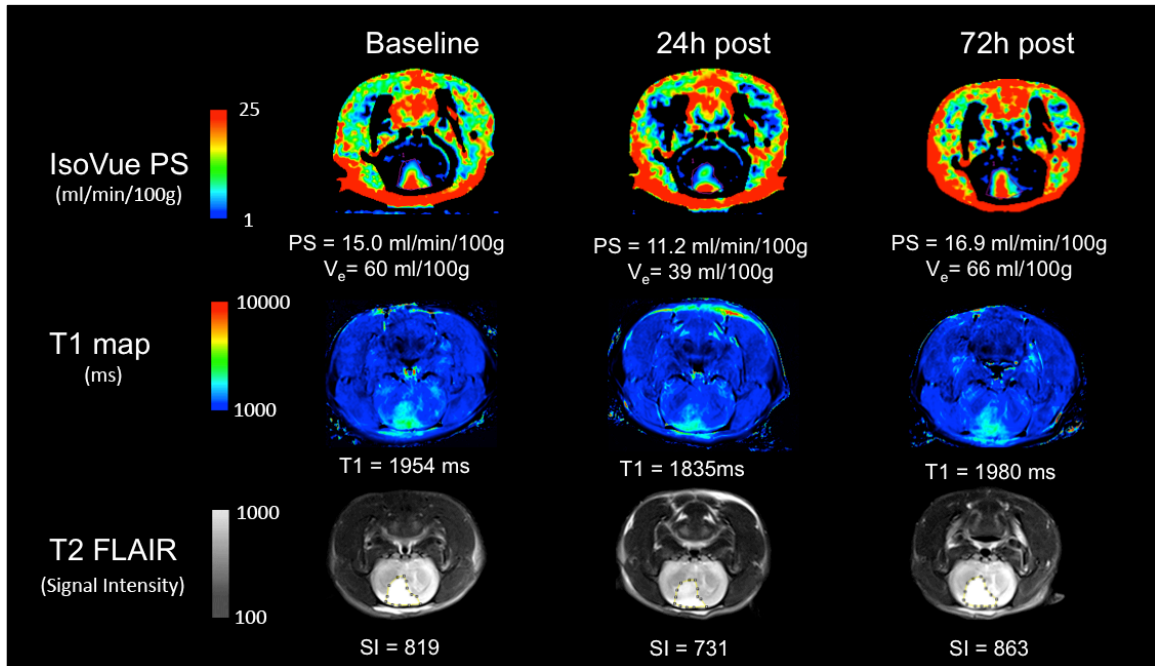


**Figure 4-4: CT Perfusion derived Isovue PS maps, and MRI longitudinal relaxation time (T1), and fluid attenuated inverted recovery (FLAIR) maps for a rat following FUSwMB.**

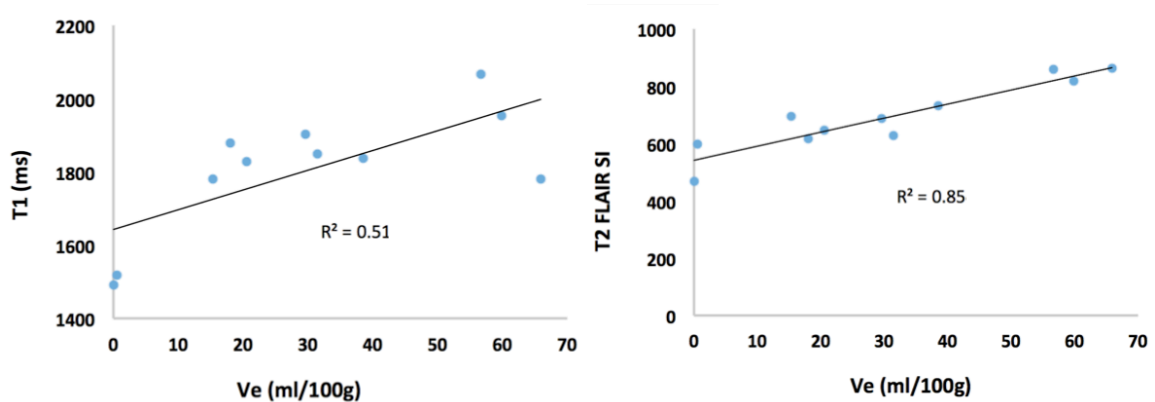


**Figure 4-5: Correlation of CT Perfusion derived extravascular distribution volume ( $V_e$ ) with MRI longitudinal relaxation time (T1), and fluid attenuated inverted recovery (FLAIR) signal intensity (SI) in 4 rats at baseline, 24 hr, and 72 hr post sonication.**

A box plot quantifying the number of collapsed and intact CD31 expressing vessels in the sonicated and control group is shown in Figure 4-6. Comparing the tumor vasculature before (control group) and at 24 h following FUSwMB revealed that the total number of CD31 expressing collapsed vessels in the sonicated group ( $9 \pm 2$ ;  $p < 0.01$ ) was significantly greater than control ( $2 \pm 1$ ). For the control group, the total number of CD31 expressing intact vessels ( $7 \pm 1$ ;  $p < 0.02$ ) was also significantly greater than the number of collapsed vessels ( $2 \pm 1$ ), whereas there was no difference between intact ( $5 \pm 2$ ;  $p = 0.1$ ) and collapsed vessels ( $9 \pm 2$ ) in the sonicated group. The average vimentin expression score was significantly higher in the sonicated group ( $2.5 \pm 0.6$ ;  $p < 0.05$ ) compared to the control group ( $1.3 \pm 0.6$ ). Representative regions from the CD31 and vimentin stained sections are presented for the sonicated and control groups in Figure 4-7.

#### 4.4 Discussion

The purpose of this study was two-fold: 1) Use CT Perfusion and MRI to investigate the change in vasogenic edema resulting from the decrease in BTB PS to small molecules up to 72 hours following FUSwMB, and 2) use immunohistochemistry to investigate the histopathology that contributes to the observed tumor response.

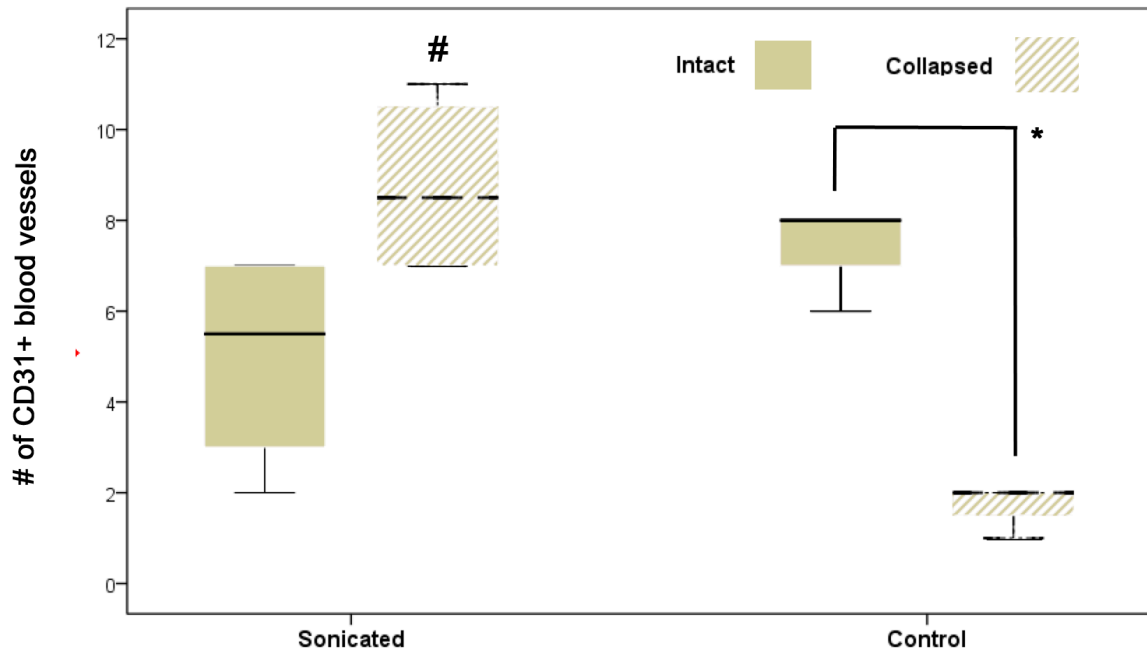


**Figure 4-6: Boxplots of the total number of intact and collapsed CD31 expressing vessels for all 5 fields in the sonicated (r=4) and control (r=3) groups. #Significantly different than the control group,  $P < 0.05$ . \*Significant difference between the number of intact and collapsed CD31 expressing vessels,  $P < 0.05$ .**

In Chapter 3 of this thesis, we reported on the decrease in BTB PS up to 72 hours following FUSwMB, using a small (760 Da) diffusible CT contrast agent. As discussed in Chapter 1,  $V_e$  is the extravascular contrast distribution volume in tissue or it is the surrogate marker of vasogenic edema. In this study, we found that the CT Perfusion derived  $V_e$  was significantly lower at 24 h post sonication, the time-point at which the measured BTB PS was also the lowest. It has been previously reported that both T1 and T2 values from proton MRI can be used as surrogates of vasogenic brain edema, in pre-clinical and clinical cases (28,29). Our MRI subgroup demonstrated that quantitative T1 measured with dual flip angles at 24 h post was lower than baseline although this difference was not significant. However, T2-FLAIR signal did not show any significant decrease from baseline at any of the time-points. CT Perfusion derived  $V_e$  showed

moderate to strong correlation with both the quantitative T1 ( $R^2 = 0.52$ ) and T2-FLAIR SI ( $R^2 = 0.85$ ), implying that it can be used as a surrogate of vasogenic brain edema.

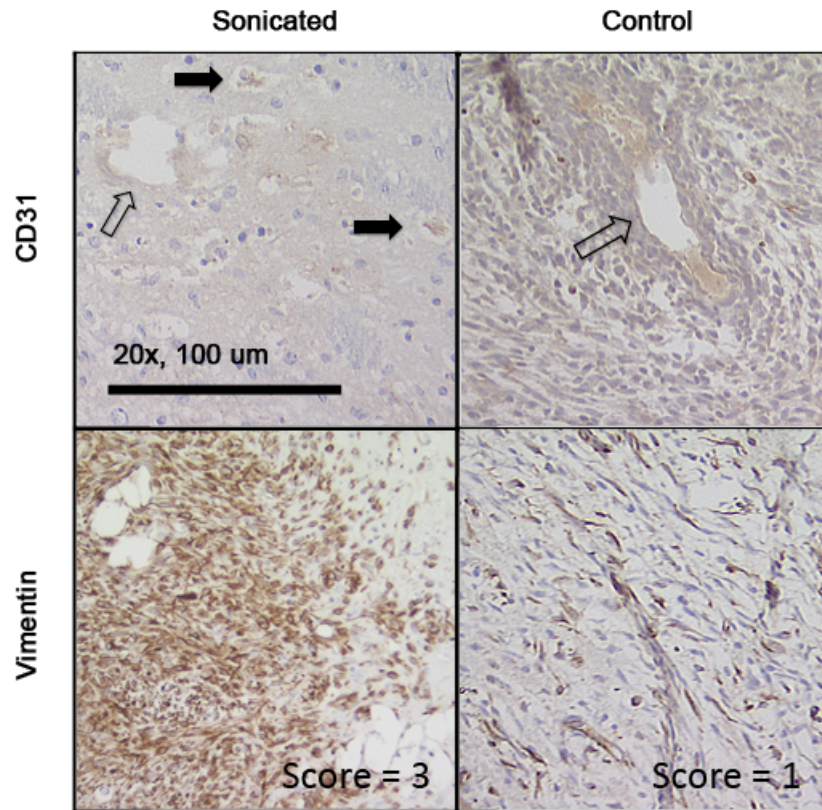


**Figure 4-7: Representative immunohistochemical stained tumor regions showing intact (hollow arrow) and collapsed (filled arrow) CD31 expressing vessels, as well as vimentin expression score, in the sonicated (n=4) and control groups (n=3). The representative vimentin expression shown was scored as 3 in the sonicated group, and as 1 in the control group.**

Another interesting finding from this study is that both CT Perfusion derived CBF and CBV show an increasing trend at 24 h post, at the time-point when both the tumor PS and vasogenic edema were at their lowest. This effect is similar to the ‘normalization’ anti-tumor effect that has been associated with anti-angiogenic therapies such as bevacizumab (30). These findings highlight the potential of combining anti-angiogenic therapies and FUSwMB, conferring a synergistic effect that decreases edema from reduced tumor PS

while normalizing the vasculature to increase blood flow and hence drug delivery. Not only would this lessen the neurological symptoms resulting from vasogenic edema in the brain, but may also increase the delivery of larger molecules that are unable to passively diffuse across the BTB, and must rely on the transvascular pressure gradient driven convective transport to get into the tumor, as discussed in chapter 3 of this thesis.

The goal in the second part of this study was to use immunohistochemical staining to investigate the histopathology behind the decreased PS and vasogenic edema within the tumor. An anti-CD31 stain was used to evaluate the number of intact and collapsed microvessels within the most vascular region of the tumor, to quantify the vascular density and damage before and at 24 h following FUSwMB. In the untreated control tumors, there was significantly greater number of intact vessels than collapsed vessels, of the latter there were almost none. At 24 h following FUSwMB, there was a significant increase in the number of collapsed vessels when compared to the untreated control. These results suggest that FUSwMB using the exposure parameters optimized to induce transient BBB opening with minimal vascular injury (have to reference your first paper here), may be used to selectively target and destroy newly formed angiogenic vessels, which lack functional pericyte coverage and are more susceptible to damage. In GBM, the newly formed angiogenic vessels contribute to the increased PS, the destruction of which would lead to the decrease in PS measured with CT Perfusion.

An anti-vimentin stain was also used to assess pericyte coverage and/or glial expression before and at 24 h following sonication. Vimentin is an intermediate filament protein that plays a key cytoskeletal role, and has been previously shown to correspond with glial fibrillary acidic protein (GFAP) expression in the central nervous system (CNS) (31). One of the important functions of glial cells is to regulate BBB function through its vascular-encircling end feet (32). In response to many CNS pathologies, such as stroke, trauma, or tumor growth, a structural and functional astrocytic response called ‘reactive gliosis’ is able to partially restore BBB function (33). Studies using a genetic mouse model determined that in the absence of intermediate filament proteins, such as vimentin or GFAP, reactive gliosis is attenuated with distinct pathophysiological and clinical consequences (34), indicating that the BBB regulatory function of glial cells is dependent

on the expression of these proteins. Our immunohistochemical results found that tumors at 24 h following sonication displayed moderate to heavy vimentin expression, whereas untreated control tumors displayed only light to moderate vimentin expression, suggesting the possibility of some form of reactive gliosis that developed following FUSwMB, decreasing BTB permeability, and the associated vasogenic edema. It is important to consider that the procedure used to score vimentin did not discriminate between the two features of vimentin expression – pericyte coverage or activated glial cells. As such, the increased vimentin expression at 24 h following sonication may be attributed to the increased pericyte expression or activation of glial cells. Further co-expression studies are required to evaluate the changes in pericyte and/or activated glial following sonication, along with vimentin staining.

There are limitations of this study to be considered. First, CT Perfusion derived  $V_e$ , measured with a small (760 Da) diffusible iodinated contrast agent and a relatively short acquisition time of 3.5 min, may not reflect the true water  $V_e$  as a surrogate of vasogenic edema. However, we did find  $V_e$  correlated well with MRI T1 and T2, which have previously been shown to measure water content and vasogenic edema (35). The second limitation was using immunohistochemical staining to investigate the histopathologic basis behind the observed decrease in BTB permeability and vasogenic edema, particularly with the correlation of immunohistochemical findings with imaging results. Brain tumors, particularly GBM, can be highly heterogeneous due to the presence of multiple cell types in the microscopic scale, whereas CT Perfusion derived measures of permeability and vasogenic edema were performed at a much larger spatial scale, making it difficult to compare immunohistochemical staining and imaging results.

## 4.5 Conclusion

In this study, we used CT Perfusion to derive the extravascular distribution volume ( $V_e$ ) as a surrogate of vasogenic edema in a pre-clinical C6 rat glioma model. We found that  $V_e$  was significantly lower at 24 h post sonication, the time at which BTB PS was also at its lowest. CT Perfusion derived  $V_e$  showed moderate to strong correlations with MRI T1 and T2 measurements, which have previously been shown to correlate with the extent of vasogenic edema in brain tumors, indicating it may be used as a reliable surrogate of

vasogenic edema in brain tumors. In addition, immunohistochemical staining of vascular and glial markers suggests the destruction of newly formed and angiogenic blood vessel and/or the increased glial expression resulting from intermediate filament driven reactive gliosis, may be responsible for the decrease in PS and vasogenic edema following FUSwMB.

## 4.6 References

1. Valk PE, Mathis CA, Prados MD, Gilbert JC, Budinger TF. Hypoxia in human gliomas: demonstration by PET with fluorine-18-fluoromisonidazole. *J Nucl Med.* 1992;33(12):2133–7.
2. Plate KH, Mennel HD. Vascular morphology and angiogenesis in glial tumors. *Exp Toxicol Pathol [Internet].* 1995;47(2-3):89–94.
3. Rampling R, Cruickshank G, Lewis AD, Fitzsimmons SA, Workman P. Direct measurement of pO<sub>2</sub> distribution and bioreductive enzymes in human malignant brain tumors. *Int J Radiat Oncol Biol Phys.* 1994;29(3):427–31.
4. Winkler F, Kozin S V., Tong RT, Chae SS, Booth MF, Garkavtsev I, et al. Kinetics of vascular normalization by VEGFR2 blockade governs brain tumor response to radiation: Role of oxygenation, angiopoietin-1, and matrix metalloproteinases. *Cancer Cell [Internet].* 2004;6(6):553–63.
5. Yuan F, Salehi HA, Boucher Y, Vasthare US, Tuma RF, Jain RK. Vascular permeability and microcirculation of gliomas and mammary carcinomas transplanted in rat and mouse cranial windows. *Cancer Res.* 1994;54(17):4564–8.
6. Hobbs SK, Monsky WL, Yuan F, Roberts WG, Griffith L, Torchilin VP, et al. Regulation of transport pathways in tumor vessels: role of tumor type and microenvironment. *Proc Natl Acad Sci U S A.* 1998;95(8):4607–12.
7. Monsky WL, Fukumura D, Gohongi T, Ancukiewicz M, Weich HA, Torchilin VP, et al. Augmentation of transvascular transport of macromolecules and

- nanoparticles in tumors using vascular endothelial growth factor. *Cancer Res.* 1999;59(16):4129–35.
8. Jain RK, Tong RT, Munn LL. Effect of vascular normalization by antiangiogenic therapy on interstitial hypertension, peritumor edema, and lymphatic metastasis: Insights from a mathematical model. *Cancer Res.* 2007;67(6):2729–35.
  9. Strugar J, Rothbart D, Harrington W, Criscuolo GR. Vascular permeability factor in brain metastases: correlation with vasogenic brain edema and tumor angiogenesis. *J Neurosurg [Internet]*. 1994;81(4):560–6.
  10. Jain RK, di Tomaso E, Duda DG, Loeffler JS, Sorensen a G, Batchelor TT. Angiogenesis in brain tumours. *Nat Rev Neurosci.* 2007;8(8):610–22.
  11. Bebawy JF. Perioperative Steroids for Peritumoral Intracranial Edema. *Journal of Neurosurgical Anesthesiology.* 2012. p. 173–7.
  12. Jain RK. Normalization of tumor vasculature: an emerging concept in antiangiogenic therapy. *Science.* 2005;307(5706):58–62.
  13. Tong RT, Boucher Y, Kozin S V., Winkler F, Hicklin DJ, Jain RK. Vascular normalization by vascular endothelial growth factor receptor 2 blockade induces a pressure gradient across the vasculature and improves drug penetration in tumors. *Cancer Res.* 2004;64(11):3731–6.
  14. Pope WB, Lai a., Nghiemphu P, Mischel P, Cloughesy TF. MRI in patients with high-grade gliomas treated with bevacizumab and chemotherapy. *Neurology.* 2006;66:1258–60.
  15. Vredenburgh JJ, Desjardins A, Herndon JE, Dowell JM, Reardon D a, Quinn J a, et al. Phase II trial of bevacizumab and irinotecan in recurrent malignant glioma. *Clin Cancer Res.* 2007;13(4):1253–9.

16. Heiss WD, Dohmen C, Sobesky J, Kracht L, Bosche B, Staub F, et al. Identification of malignant brain edema after hemispheric stroke by PET-imaging and microdialysis. *Acta Neurochir Suppl* [Internet]. 2003;86:237–40.
17. St. Lawrence KS, Owen D, Wang DJJ. A two-stage approach for measuring vascular water exchange and arterial transit time by diffusion-weighted perfusion MRI. *Magn Reson Med*. 2012;67(5):1275–84.
18. Johnson JA, Wilson TA. A model for capillary exchange. *Am J Physiol -- Leg Content* [Internet]. 1966 Jun 1;210(6):1299–303.
19. St Lawrence KS, Lee TY. An adiabatic approximation to the tissue homogeneity model for water exchange in the brain: II. Experimental validation. *J Cereb Blood Flow Metab*. 1998;18(12):1378–85.
20. Lee T-Y, Purdie TG, Stewart E. CT imaging of angiogenesis. *Q J Nucl Med*. 2003;47(3):171–87.
21. Crone C. The Permeability of Capillaries in Various Organs as Determined by Use of the Indicator Diffusion Method. *Acta Physiol Scand*. 1963;58(4):292–305.
22. Jain R, Narang J, Griffith B, Bagher-Ebadian H, Scarpace L, Mikkelsen T, et al. Prognostic Vascular Imaging Biomarkers in High-Grade Gliomas. Tumor Permeability as an Adjunct to Blood Volume Estimates. *Acad Radiol*. 2013;20(4):478–85.
23. Jain R. Perfusion CT imaging of brain tumors: an overview. *AJNR Am J Neuroradiol* [Internet]. 2011;32(9):1570–7.
24. Bandopadhyay R, Orte C, Lawrenson JG, Reid AR, De Silva S, Allt G. Contractile proteins in pericytes at the blood-brain and blood-retinal barriers. *J Neurocytol*. 2001;30(1):35–44.

25. Schnitzer J, Franke WW, Schachner M. Immunocytochemical demonstration of vimentin in astrocytes and ependymal cells of developing and adult mouse nervous system. *J Cell Biol.* 1981;90(2):435–47.
26. Chauhan VP, Martin JD, Liu H, Lacorre DA, Jain SR, Kozin S V, et al. Angiotensin inhibition enhances drug delivery and potentiates chemotherapy by decompressing tumour blood vessels. *Nat Commun [Internet].* 2013;4:2516.
27. Maruno M, Yoshimine T, Ushio Y, Hayakawa T, Jamshidi J, Arita N, et al. Immunohistochemical study of human brain tumors with vimentin and astroprotein (GFAP). *J Neurooncol [Internet].* 1987;5(4):377–85.
28. Fu Y, Tanaka K, Nishimura S. Evaluation of brain edema using magnetic resonance proton relaxation times. *Adv Neurol.* 1990;52:165–76.
29. Kamman RL, Go KG, Brouwer W, Berendsen HJ. Nuclear magnetic resonance relaxation in experimental brain edema: Effects of water concentration, protein concentration, and temperature. *Magn Reson Med.* 1988;6(3):265–74.
30. Beal K, Abrey LE, Gutin PH. Antiangiogenic agents in the treatment of recurrent or newly diagnosed glioblastoma: analysis of single-agent and combined modality approaches. *Radiat Oncol [Internet].* BioMed Central Ltd; 2011;6(1):2.
31. Oudega M, Marani E. Expression of vimentin and glial fibrillary acidic protein in the developing rat spinal cord: an immunocytochemical study of the spinal cord glial system. *J Anat [Internet].* 1991;179:97–114.
32. Alvarez JI, Katayama T, Prat A. Glial influence on the blood brain barrier. *Glia.* 2013;61(12):1939–58.
33. Pekny M, Nilsson M. Astrocyte activation and reactive gliosis. *Glia.* 2005;50(4):427–34.

34. Lu Y-B, Iandiev I, Hollborn M, Körber N, Ulbricht E, Hirrlinger PG, et al. Reactive glial cells: increased stiffness correlates with increased intermediate filament expression. *FASEB J* [Internet]. 2011;25(2):624–31.
35. Barber PA, Hoyte L, Kirk D, Foniok T, Buchan A, Tuor U. Early T1- and T2-weighted MRI signatures of transient and permanent middle cerebral artery occlusion in a murine stroke model studied at 9.4 T. *Neurosci Lett*. 2005;388(1):54–9.

## Chapter 5

### 5 Conclusion and Future Work

#### 5.1 Summary of Findings

This thesis demonstrated: 1) the feasibility of using CT Perfusion to monitor blood-brain barrier and brain tumor barrier (BBB/BTB) permeability surface product (PS) in normal intact brain and brain tumor respectively following FUS sonication with MB administration (FUSwMB); 2) in a C6-glioma brain tumor model in rats, instead of a transient increase in PS as seen in normal brain, a decrease in PS acutely and at 24 hours following FUSwMB; 3) correlation of the observations in 2) with decrease in vasogenic edema corroborated by tissue water imaging with MR and with pruning of immature leaky blood vessels and reactive gliosis as shown by histopathology.

##### 5.1.1 CT Perfusion to quantify PS changes following FUSwMB

Prior to the work presented in this thesis, there were only a handful of pre-clinical studies that attempted to use tracer kinetic analysis to quantify endothelial PS following FUSwMB, using either Gd-enhanced T1 MRI (1,2), or SPECT (3).

For dynamic contrast enhanced studies, CT has the following advantages over MRI: 1) Greater temporal resolution with sub-millimeter spatial resolution, 2) better quantitative accuracy as x-ray attenuation is less affected by the tumor microenvironment (4), and 3) less susceptibility to contrast signal saturation from repeated scans (5).

In Chapter 2 of this thesis, we presented a range of FUSwMB parameters that can induce transient BBB opening in a normal rabbit brain, with minimal damage to neurons and vasculature, monitored with CT Perfusion derived BBB PS. Furthermore, measured PS time profiles post FUSwMB allow for visualization of the distinct window for increased therapeutic drug delivery, and provide a method for quantifying and monitoring the extent of drug delivery in a clinical setting.

### 5.1.2 BTB PS response following FUSwMB

Previous pre-clinical brain tumor studies have attempted to quantify the tumor permeability to various molecules following FUSwMB (6–11). The few studies that have attempted to characterize BTB PS found an increase in the parameter and/or drug delivery following sonication, although the results varied because of the stage (early or late) at which the tumor is sonicated, and the time delay following sonication at which PS or delivery was evaluated (6,10).

In Chapter 3 of this thesis, we demonstrated that although there was a transient increase in BTB small molecule PS immediately following FUSwMB, this is followed by a decrease in PS at 24 hours post, particularly in underdeveloped and less permeable tumors. However, when a larger contrast molecule was used, there was a trend of increasing PS following FUSwMB, although this was not significant after correction for multiple comparison. This surprising result was rationalized by the physical destruction of newly formed and highly permeable angiogenic vessels which lack pericyte coverage and/or the stimulation of microglia in and around the tumor vasculature, highlighting the potential for FUSwMB to manipulate the tumor vasculature and its microenvironment, beyond simply opening the BTB. Furthermore, the decrease in Isovue PS between 24-72 hrs following FUSwMB may be accompanied by a decrease in edema as corroborated by tissue water imaging with MR, and interstitial fluid pressure (IFP), thereby increasing PS and accumulation of larger chemotherapeutic agents, such as bevacizumab, that are unable to passively diffuse across the BTB and must rely on convective bulk solute flow.

In the context of drug delivery, the volume transfer constant  $K_{trans}$  (FE), which is estimated by the Johnson and Wilson (JW) model and encapsulate the influence of blood flow relative to PS, is more appropriate for drug delivery than PS alone. Unlike the normal brain, where drug delivery across the disrupted BBB is diffusion limited and FE can be approximated by PS, this condition is not necessarily true in brain tumors, where the PS may be significantly elevated relative to blood flow, in which case FE would be a more appropriate functional parameter to quantify transvascular drug delivery, particularly for larger drugs that rely on convective solute flux, instead of diffusion. Further investigation is required to determine whether PS or FE is the correct functional

parameter to use and under which conditions, when measuring drug delivery across the BTB.

In Chapter 4 of this thesis, we showed that this decrease in BTB PS, as measured with a small molecule CT contrast agent Isovue, was accompanied by a decrease in the extravascular distribution volume,  $V_e$ , a surrogate of vasogenic edema. The implication of this finding is that FUSwMB may be used to temporarily alleviate the IFP that results from vasogenic edema in brain tumors, as well as increase the delivery of molecules across the BTB, particularly larger antibody-like molecules such as bevacizumab, that rely on convective transport to accumulate in the tumor. In addition, immunohistochemical staining of vascular and glial markers suggest the destruction of immature leaky blood vessel, and/or the increased glial expression, as a form of intermediate filament driven reactive gliosis, may be responsible for the decrease in PS and vasogenic edema following FUSwMB in brain tumors.

## 5.2 Future Work

The work presented in this thesis used CT Perfusion measured PS to address questions regarding the use of FUSwMB to increase drug delivery of blood borne solutes across intact BBB in normal brain and across the BTB in a rat C6 tumor model. Our findings in brain tumor led us to conclude that although the BTB may increase hours following sonication, it is preceded by a decrease in PS, and therefore vasogenic edema. This seemingly contradictory result has generated a number of new and important questions that future investigation can address.

### 5.2.1 Evaluating the increase in PET-labeled Bevacizumab delivery following FUSwMB in a C6 Rat Tumor Model

One of the significant findings of this thesis was the decrease in BTB PS, measured using a standard small molecule CT contrast agent, at 24 hours following FUSwMB. To our knowledge, this is a previously unreported result, and generates a number of questions. In the context of blood borne solute drug delivery, a decrease in measured BTB PS is not beneficial. However, the decrease in BTB PS was also accompanied by a decrease in vasogenic edema, which we hypothesize would restore the transvascular pressure

gradient required for the delivery of larger molecules, such as bevacizumab, that are reliant on convective transport across the BTB. Radiolabeled PET tracers are commonly used to evaluate drug delivery and accumulation in tumors. Recently, bevacizumab has been tagged with  $^{89}\text{Zr}$  in a number of studies looking at its delivery and distribution in tumors (12–16). A future study using  $^{89}\text{Zr}$  labeled bevacizumab would allow us to evaluate the improved delivery that results from a decrease in BTB PS, as measured by a diffusible small molecule CT tracer post FUSwMB in a C6 brain tumor model.

### 5.2.2 Improvement in clinical outcomes following FUSwMB in combination with Bevacizumab administration in a C6 Rat Glioma Model

In a healthy brain, pro- and anti- angiogenic signaling molecules are balanced and able to maintain an organized and efficient vascular supply. In brain tumors, the overexpression of pro-angiogenic factors, such as vascular endothelial growth factor (VEGF) results in a permeable BTB, increased IFP, and therefore vasogenic edema. Gliomas, which account for approximately 70% of all malignant brain tumors, demonstrate particularly poor prognosis due in part to the vasogenic edema that results from the breakdown in the BTB (17). Furthermore, this breakdown in BTB is also accompanied by an increase in IFP (18), which creates a barrier for transvascular drug delivery, increases hypoxia induced treatment resistance within and surrounding the tumor, and promotes micrometastasis surrounding the primary tumor that serve as sites of recurrence (19).

In Chapter 4 of this thesis, we showed that the decrease in BTB PS following FUSwMB, as measured with a standard small molecule CT contrast agent, was also accompanied by a decrease in extravascular distribution volume,  $V_e$ , which is a surrogate of vasogenic edema. It can be hypothesized that this decrease in vasogenic edema following FUSwMB is also accompanied by a decrease in IFP in and around the tumor mass – leading to a ‘vascular normalization’ effect that has been associated with anti-angiogenic therapies such as bevacizumab (20–22). The destruction of newly formed pro-angiogenic vessels or the stimulation of reactive glial cells following FUSwMB would normalize the BTB permeability, lowering the surrounding IFP and improving perfusion throughout the tumor. Not only would this benefit the neurological symptoms that result from vasogenic

edema in the brain, but should also increase the delivery of larger molecules that rely on the transvascular pressure gradient driven convective transport across the BTB, as discussed in chapter 3 of this thesis. A future study looking at the improvement in clinical outcomes, particularly survival, from increased bevacizumab delivery following FUSwMB, in a C6 Rat Glioma Model would allow for the investigation of this synergistic benefit.

### 5.3 References

1. Park J, Zhang Y, Vykhodtseva N, Jolesz F a., McDannold NJ. The kinetics of blood brain barrier permeability and targeted doxorubicin delivery into brain induced by focused ultrasound. *J Control Release* [Internet]. Elsevier B.V.; 2012;162(1):134–42.
2. Vlachos F, Tung Y-S, Konofagou EE. Permeability assessment of the focused ultrasound-induced blood-brain barrier opening using dynamic contrast-enhanced MRI. *Phys Med Biol*. 2010;55(18):5451–66.
3. Yang F-Y, Wang H-E, Lin G-L, Teng M-C, Lin H-H, Wong T-T, et al. Micro-SPECT/CT-based pharmacokinetic analysis of <sup>99m</sup>Tc-diethylenetriaminepentaacetic acid in rats with blood-brain barrier disruption induced by focused ultrasound. *J Nucl Med*. 2011;52(3):478–84.
4. Eastwood JD, Lev MH, Wintermark M, Fitzek C, Barboriak DP, DeLong DM, et al. Correlation of Early Dynamic CT Perfusion Imaging with Whole-Brain MR Diffusion and Perfusion Imaging in Acute Hemispheric Stroke. *Am J Neuroradiol*. 2003;24(9):1869–75.
5. Wintermark M, Maeder P, Thiran JP, Schnyder P, Meuli R. Quantitative assessment of regional cerebral blood flows by perfusion CT studies at low injection rates: A critical review of the underlying theoretical models. *Eur Radiol*. 2001;11(7):1220–30.

6. Aryal M, Park J, Vykhodtseva N, Zhang Y-Z, McDannold N. Enhancement in blood-tumor barrier permeability and delivery of liposomal doxorubicin using focused ultrasound and microbubbles: evaluation during tumor progression in a rat glioma model. *Phys Med Biol* [Internet]. IOP Publishing; 2015;60(6):2511–27.
7. Liu H-L, Huang C-Y, Chen J-Y, Wang H-YJ, Chen P-Y, Wei K-C. Pharmacodynamic and Therapeutic Investigation of Focused Ultrasound-Induced Blood-Brain Barrier Opening for Enhanced Temozolomide Delivery in Glioma Treatment. *PLoS One* [Internet]. 2014;9(12):e114311.
8. Liu H-L, Hua M-Y, Chen P-Y, Chu P-C, Pan C-H, Yang H-W, et al. Blood-brain barrier disruption with focused ultrasound enhances delivery of chemotherapeutic drugs for glioblastoma treatment. *Radiology*. 2010;255(2):415–25.
9. Chu PC, Chai WY, Hsieh HY, Wang JJ, Wey SP, Huang CY, et al. Pharmacodynamic analysis of magnetic resonance imaging-monitored focused ultrasound-induced blood-brain barrier opening for drug delivery to brain tumors. *Biomed Res Int*. 2013;2013.
10. Yang FY, Ko CE, Huang SY, Chung IF, Chen GS. Pharmacokinetic changes induced by focused ultrasound in glioma-bearing rats as measured by dynamic contrast-enhanced MRI. *PLoS One*. 2014;9(3).
11. Park E-J, Zhang Y-Z, Vykhodtseva N, McDannold N. Enhanced permeability of tumor blood vessels in brain using focused ultrasound with microbubbles. 2010 *IEEE Int Ultrason Symp*. 2010;2123–6.
12. Van Der Bilt ARM, Terwisscha Van Scheltinga AGT, Timmer-Bosscha H, Schröder CP, Pot L, Kosterink JGW, et al. Measurement of tumor VEGF-A levels with <sup>89</sup>Zr-bevacizumab PET as an early biomarker for the antiangiogenic effect of everolimus treatment in an ovarian cancer xenograft model. *Clin Cancer Res*. 2012;18(22):6306–14.

13. Nagengast WB, de Korte M a, Oude Munnink TH, Timmer-Bosscha H, den Dunnen WF, Hollema H, et al.  $^{89}\text{Zr}$ -bevacizumab PET of early antiangiogenic tumor response to treatment with HSP90 inhibitor NVP-AUY922. *J Nucl Med* [Internet]. 2010;51(5):761–7.
14. Oosting SF, Brouwers AH, van Es SC, Nagengast WB, Oude Munnink TH, Lub-de Hooge MN, et al.  $^{89}\text{Zr}$ -bevacizumab PET visualizes heterogeneous tracer accumulation in tumor lesions of renal cell carcinoma patients and differential effects of antiangiogenic treatment. *J Nucl Med* [Internet]. 2015;56(1):63–9.
15. Gaykema SB, Brouwers a H, Lub-de Hooge MN, Pleijhuis RG, Timmer-Bosscha H, Pot L, et al.  $^{89}\text{Zr}$ -bevacizumab PET imaging in primary breast cancer. *J Nucl Med* [Internet]. 2013;54(7):1014–8.
16. Gaykema SBM, Schröder CP, Vitfell-Rasmussen J, Chua S, Munnink THO, Brouwers AH, et al.  $^{89}\text{Zr}$ -trastuzumab and  $^{89}\text{Zr}$ -bevacizumab PET to evaluate the effect of the HSP90 inhibitor NVP-AUY922 in metastatic breast cancer patients. *Clin Cancer Res*. 2014;20(15):3945–54.
17. Grossman S a., Batara JF. Current management of glioblastoma multiforme. *Semin Oncol* [Internet]. 2004;31(5):635–44.
18. Jain RK. Vascular and interstitial barriers to delivery of therapeutic agents in tumors. *Cancer Metastasis Rev*. 1990;9(3):253–66.
19. Jain RK. Normalizing tumor microenvironment to treat cancer: bench to bedside to biomarkers. *J Clin Oncol*. 2013;31(17):2205–18.
20. Beal K, Abrey LE, Gutin PH. Antiangiogenic agents in the treatment of recurrent or newly diagnosed glioblastoma: analysis of single-agent and combined modality approaches. *Radiat Oncol* [Internet]. BioMed Central Ltd; 2011;6(1):2.
21. Winkler F, Kozin S V., Tong RT, Chae SS, Booth MF, Garkavtsev I, et al. Kinetics of vascular normalization by VEGFR2 blockade governs brain tumor

response to radiation: Role of oxygenation, angiopoietin-1, and matrix metalloproteinases. *Cancer Cell* [Internet]. 2004;6(6):553–63.

22. Jain RK. Normalization of tumor vasculature: an emerging concept in antiangiogenic therapy. *Science*. 2005;307(5706):58–62.

## Curriculum Vitae

### EDUCATION

---

- 11/01 – present      Ph.D in Medical Biophysics  
 Department of Medical Biophysics,  
 The University of Western Ontario, London, ON, Canada  
**Thesis:** Using Dynamic Contrast Enhanced Computed Tomography to Evaluate  
 Blood-Brain-Barrier and Blood-Tumor-Barrier Response in Pre-Clinical Models  
**Supervisor:** Dr. Ting Lee
- 09/08 – 04/10      M.Sc. in Medical Biophysics  
 Department of Medical Biophysics,  
 The University of Western Ontario, London, ON, Canada  
**Thesis:** Hyperpolarized Helium-3 Magnetic Resonance Imaging of Cystic  
 Fibrosis.  
**Supervisor:** Dr. Grace Parraga
- 09/04 – 04/08      B.Sc (Honours)  
 Biopharmaceutical Sciences, Specialization in Medicinal Chemistry  
 University of Ottawa, Ottawa, ON, Canada

### WORK EXPERIENCE (Selected)

---

- 09/08 – present      Graduate Research Assistant  
 The University of Western Ontario, London, ON, Canada  
 Department of Medical Biophysics
- 05/08 – 08/08      Summer Research Assistant  
*Analyzed data for ongoing imaging studies and helped develop protocols for future  
 studies.*  
 Imaging Research Laboratories, Robarts Research Institute, London, ON, Canada
- 10/07 – 04/08      Medical Assistant (Part-time)  
*Assisted and helped manage day to day operations at the medical clinic. Triage  
 patients and prepared them for the physician.*  
 Appletree Medical Centre, Ottawa, ON, Canada

### ACADEMIC AWARDS AND SCHOLARSHIPS

---

- 09/13 – 08/14 Canadian Institute for Health Research (CIHR) Strategic Training Program in Cancer Research and Technology Transfer (CaRTT)  
*Awarded to graduate trainees working on high impact translational cancer science and treatment projects*  
International  
**\$15,000/yr**
- 11/12 Radiological Society of North America (RSNA) Trainee Research Prize 2012 (Neuroradiology Category)  
*Awarded to best original research paper by a medical student/resident/physics trainee in each category*  
International  
**\$1000**
- 09/12 – 08/13 Canadian Institute for Health Research (CIHR) Strategic Training Program in Cancer Research and Technology Transfer (CaRTT)  
*Awarded to graduate trainees working on high impact translational cancer science and treatment projects*  
International  
**\$15,000/yr**
- 11/09 Radiological Society of North America (RSNA) Trainee Research Prize 2009 (Chest Radiology Category)  
*Awarded to best original research paper by a medical student/resident/physics trainee in each category*  
International  
**\$1000**
- 09/08 – 08/10 Western Graduate Research Scholarship (The University of Western Ontario)  
*Awarded to graduate students who enrolled with an average of 78% or above.*  
Institutional  
**\$4,100/yr**
- 09/07 – 04/08 Constance Nozzolillo Scholarship (University of Ottawa)  
*Awarded to B.Sc. students with a B+ standing and in financial need*  
Institutional  
**\$1000**
- 09/06 – 04/07 Biopharmaceutical Science Director's Scholarship (University of Ottawa)  
*Awarded to a biopharmaceutical science students based on academic standing and involvement in the program*  
Institutional  
**\$500**
- 09/04 – 04/08 Academic Entrance Scholarship (University of Ottawa)  
*Awarded upon admission who have an admission average of 85-89.9%.*  
Institutional  
**\$2,500/yr**

---

#### RELEVANT GRADUATE COURSES

Department of Medical Biophysics  
The University of Western Ontario,  
London, ON, Canada

Inferential Statistics (01/09 – 04/09) – **90%**  
Scientific Communications (09/08 – 03/09) – **83%**  
Medical Imaging (09/08 – 12/08) – **90%**  
Vascular Imaging (09/08 – 12/08) – **94%**  
Research Ethics and Biostatistics (09/08 – 12/08) – **94%**

## PUBLICATIONS AND PRESENTATIONS

### Peer Reviewed Journal Manuscripts (3)

---

**H. Ahmed**, R. Chopra, K. Hynynen, and TY. Lee. *Investigating the Decrease in Edema Following Focused Ultrasound with Microbubble Administration using Magnetic Resonance Imaging, and Dynamic Contrast Enhanced Computed Tomography Derived Vascular Distribution Volume in a C6 Rat Glioma Model*. In preparation for submission to *Academic Radiology*.

**H. Ahmed**, R. Chopra, K. Hynynen, and TY. Lee. *Comparison of Small (760 Da) and Large (65 kDa) Contrast Agent Dynamic Contrast Enhanced Computed Tomography to Measure Blood-Tumor-Barrier Permeability Surface Response Following Focused Ultrasound Sonication with Microbubble Administration in a C6 Rat Glioma Model*. In preparation for submission to *Ultrasound In Medicine and Biology*.

**H. Ahmed**, A. Waspe, R. Chopra, K. Hynynen, D. Jackson, and TY. Lee. *Focused Ultrasound Sonication with Microbubble Administration Induced Blood-Brain-Barrier Disruption: Quantifying the Increased Endothelial Permeability Surface Area Using Dynamic Contrast Enhanced Computed Tomography in Rabbits*. In preparation for submission to *Ultrasound In Medicine and Biology*.

### Non-Peer Reviewed Journal Manuscripts (1)

---

**H. Ahmed**, S. Choy, A. Wheatley, and G. Parraga. *Development of Spatial-Temporal Ventilation Heterogeneity and Probability Analysis Tools for Hyperpolarized Helium-3 Magnetic Resonance Imaging*. *The International Society for Optical Engineering (SPIE) Biomedical Applications in Molecular, Structural, and Functional Imaging Proceedings*, (10/09).

### Peer Reviewed Published Conference Proceedings (4)

---

**H. Ahmed**, R. Chopra, K. Hynynen, and TY. Lee. *Focused Ultrasound and Microbubble Induced Blood-Tumor-Barrier Disruption: Quantifying Endothelial Permeability using Dynamic Contrast Enhanced Computed Tomography in a C6 Rat Glioma Model*. *Radiological Society of North America (RSNA) Proceedings 2013*, (11/13).

**H. Ahmed**, A. Waspe, R. Chopra, K. Hynynen, D. Jackson, and TY. Lee. *Focused Ultrasound and Microbubble Induced Blood-Brain-Barrier Disruption: Quantifying Endothelial Permeability using Dynamic Contrast Enhanced Computed Tomography*. *Radiological Society of North America (RSNA) Proceedings 2012*, (11/12).

**H. Ahmed**, A. Wheatley, R. Etemad-Rezai, NAM. Paterson, and G. Parraga. *Hyperpolarized Helium-3 Magnetic Resonance Imaging of Adult Cystic Fibrosis: Diffusion-weighted and Static Ventilation Imaging Measurement Precision for Clinical Trials*. *Radiological Society of North America (RSNA) Proceedings*

2009, (11/09).

**H. Ahmed, A. Wheatley, NAM. Paterson, and G. Parraga.** Hyperpolarized Helium-3 Magnetic Resonance Imaging Precision in Cystic Fibrosis. American Thoracic Society (ATS) Proceedings 2009. *Am. J. Respir. Crit. Care Med.*, Apr 2009; 179: A1444

---

#### Peer Reviewed Oral Presentations (5)

**H. Ahmed, R. Chopra, K. Hynynen, and TY. Lee.** *Computed Tomography to Measure Blood-Tumor-Barrier Permeability Surface Response Following Focused Ultrasound Sonication with Microbubble Administration in a C6 Rat Glioma Model.* Imaging Network of Ontario Symposium, Toronto, Ontario, Canada (02/15).

**H. Ahmed, A. Waspe, R. Chopra, K. Hynynen, D. Jackson, and TY. Lee.** *Focused Ultrasound and Microbubble Induced Blood-Brain-Barrier Disruption: Quantifying Endothelial Permeability using Dynamic Contrast Enhanced Computed Tomography.* Imaging Network of Ontario Symposium, Toronto, Ontario, Canada (02/13).

**H. Ahmed, A. Waspe, R. Chopra, K. Hynynen, D. Jackson, and TY. Lee.** *Focused Ultrasound and Microbubble Induced Blood-Brain-Barrier Disruption: Quantifying Endothelial Permeability using Dynamic Contrast Enhanced Computed Tomography.* Radiological Society of North America (RSNA) Conference, Chicago, Illinois, USA (11/12).

**H. Ahmed, S. Choy, A. Wheatley, and G. Parraga.** *Development of Spatial Ventilation Heterogeneity and Temporal Probability Image Analysis Tools and application to Asthma Hyperpolarized Helium-3 Magnetic Resonance Imaging.* The International Society for Optical Engineering (SPIE) Biomedical Applications in Molecular, Structural, and Functional Imaging Conference, San Diego, California, USA (02/10).

**H. Ahmed, A. Wheatley, R. Etemad-Rezai, NAM. Paterson, and G. Parraga.** *Hyperpolarized Helium-3 Magnetic Resonance Imaging of Adult Cystic Fibrosis: Diffusion-weighted and Static Ventilation Imaging Measurement Precision for Clinical Trials.* Radiological Society of North America (RSNA) Conference, Chicago, Illinois, USA (11/09).

---

#### Peer Reviewed Poster Presentations (11)

**H. Ahmed, R. Chopra, K. Hynynen, and TY. Lee.** *Investigating the Decrease in Edema Following Focused Ultrasound with Microbubble Administration using Magnetic Resonance Imaging, and Dynamic Contrast Enhanced Computed Tomography Derived Vascular Distribution Volume in a C6 Rat Glioma Model.* Research Oncology Day, London, Ontario, Canada (06/15).

**H. Ahmed, R. Chopra, K. Hynynen, and TY. Lee.** *Comparison of Small (760 Da) and Large (65 kDa) Contrast Agent Dynamic Contrast Enhanced Computed Tomography to Measure Blood-Tumor-Barrier Permeability Surface Response Following Focused Ultrasound Sonication with Microbubble Administration in a C6 Rat Glioma Model.* Focused Ultrasound Symposium 2014, Bethesda, Maryland, USA (10/14).

**H. Ahmed, R. Chopra, K. Hynynen, and TY. Lee.** *Comparison of Small (760 Da) and Large (65 kDa) Contrast Agent Dynamic Contrast Enhanced Computed Tomography to Measure Blood-Tumor-Barrier Permeability Surface Response Following Focused Ultrasound Sonication with Microbubble*

*Administration in a C6 Rat Glioma Model*. London Imaging Discovery Day, London, Ontario, Canada (06/14).

**H. Ahmed**, R. Chopra, K. Hynynen, D. Jackson, and TY. Lee. *Focused Ultrasound and Microbubble Induced Blood-Tumor-Barrier Response Following Focused Ultrasound and Microbubble Treatment in a Rat Glioma Model*. Research Oncology Day, London, Ontario, Canada (06/13).

**H. Ahmed**, R. Chopra, K. Hynynen, D. Jackson, and TY. Lee. *Focused Ultrasound and Microbubble Induced Blood-Tumor-Barrier Response Following Focused Ultrasound and Microbubble Treatment in a Rat Glioma Model*. London Imaging Discovery Day, London, Ontario, Canada (06/13).

**H. Ahmed**, S. Choy, A. Wheatley, R. Etemad-Rezai, NAM. Paterson and G. Parraga. Evaluation of Ventilation Heterogeneity in Adult Cystic Fibrosis using Hyperpolarized Helium-3 Magnetic Resonance Imaging. Lawson Research Day, London, Ontario, Canada (03/10).

**H. Ahmed**, A. Wheatley, NAM. Paterson, and G. Parraga. *Reproducibility of Hyperpolarized Helium-3 Magnetic Resonance Imaging in Adult Cystic Fibrosis*. Western World Discoveries Showcase, London, Ontario, Canada (02/10).

**H. Ahmed**, A. Wheatley, NAM. Paterson, and G. Parraga. Hyperpolarized Helium-3 Magnetic Resonance Imaging Precision in Cystic Fibrosis. London Imaging Discovery (LID) Forum, London, Ontario, Canada (06/09).

**H. Ahmed**, A. Wheatley, NAM. Paterson, and G. Parraga. Hyperpolarized Helium-3 Magnetic Resonance Imaging Precision in Cystic Fibrosis. International Conference of American Thoracic Society (ATS), San Diego, California, USA (05/09)

**H. Ahmed**, M. Kirby, L. Mathew, S. Choy, AR Wheatley, G. Santyr, R. McFadden, NAM. Paterson, J. Lewis, R. Veldhuizen, C. Licskai, DG. McCormack and G. Parraga. Hyperpolarized Helium-3 Magnetic Resonance Imaging: Novel Imaging Endpoints for Respiratory Research. Canadian Respiratory Conference, Toronto, Ontario, Canada (04/09).

**H. Ahmed**, L. Mathew, A Wheatley, and G. Parraga. Tools for Assessing Differences in Hyperpolarized Helium-3 Magnetic Resonance Static Ventilation Images. 3<sup>rd</sup> International Workshop for Pulmonary Functional Imaging, Iowa City, Iowa, USA (010/08).

## CONFERENCES ATTENDED

---

- 06/15 Research Oncology Day (Local)  
London, ON, Canada
- 02/15 Imaging Network of Ontario Symposium (National)  
Toronto, ON, Canada
- 10/14 Focused Ultrasound Symposium (International)  
Bethesda, MD, USA
- 06/14 London Image Discovery (LID) Forum 2014 (Local)  
London, ON, Canada
- 06/14 Research Oncology Day (Local)  
London, ON, Canada
- 11/13 Radiological Society of North America (RSNA) 2013 Conference (International)  
Chicago, IL, USA
- 06/13 Research Oncology Day (Local)  
London, ON, Canada
- 06/13 London Image Discovery (LID) Forum 2013 (Local)  
London, ON, Canada
- 02/13 Imaging Network of Ontario Symposium (National)  
Toronto, ON, Canada
- 11/12 Radiological Society of North America (RSNA) 2012 Conference (International)  
Chicago, IL, USA  
London Image Discovery (LID) Forum 2012 (Local)  
London, ON, Canada
- 06/11 London Image Discovery (LID) Forum 2011 (Local)  
London, ON, Canada
- 02/10 International Society for Optical Engineering (SPIE) Biomedical Applications in  
Molecular, Structural, and Functional Imaging Conference 2010 (International)  
San Diego, CA, USA
- 02/10 Western World Discoveries Showcase (Local)  
London, ON, Canada
- 11/09 Radiological Society of North America (RSNA) 2009 Conference (International)  
Chicago, IL, USA
- 10/09 4<sup>th</sup> International Workshop for Pulmonary Functional Imaging (International)  
Boston, MA, USA
- 06/09 London Image Discovery (LID) Forum 2009 (Local)  
London, ON, Canada
- 05/09 International Conference of the American Thoracic Society (ATS) 2009  
(International)  
San Diego, CA, USA
- 04/09 Canadian Respiratory Conference 2009 (National)  
Toronto, ON, Canada
- 03/09 Margaret Moffat Research day 2009 (Local)  
London, ON, Canada
- 10/08 3<sup>rd</sup> International Summit on the Future of Quantitative and Functional Lung Imaging  
(International)  
Iowa City, IA, USA
- 06/08 London Image Discovery (LID) Forum 2008 (Local)  
London, ON, Canada

**PROFESSIONAL SOCIETIES**

---

09/11 - present	Focused Ultrasound Foundation <i>Member</i>
09/08 - present	Canadian Organization of Medical Physicists (COMP) <i>Member</i>
09/08 – 08/10	Canadian Thoracic Society <i>Member</i>